School of Civil and Mechanical Engineering

Multiscaling of Elasticity and Cohesion Strength in Heterogeneous Composite Materials for Surface Coating Applications Using Nanoindentation and Micromechanical Analysis

Wai Yeong Huen

This thesis is presented for the Degree of
Doctor of Philosophy
of
Curtin University

May 2020

Declaration

To the best of my knowledge and belief this thesis contains no material previously published by any other person except where due acknowledgement has been made.

This thesis contains no material which has been accepted for the award of any other degree or diploma in any university.

Wai Yeong Huen	Date

"If I have seen further it is by standing on the shoulders of Giants"

— Sir Isaac Newton

Acknowledgements

Firstly, I express my deepest gratitude to my supervisor, Associate Professor Vanissorn Vimonsatit, for her continuous guidance, encouragement and support during my PhD journey. Through her wisdom, patient and mentoring, I found my role in the academic world and manage to complete my PhD degree.

I am also indebted to Dr Hyuk Lee for his continuous support, guidance and mentorship since the beginning of my PhD journey. I am truly blessed to have Dr Lee as a friend, colleague and mentor. I thanked him for sharing his critical views on my research direction and provided the much-needed coaching on those unfamiliar territories.

I would like to extend my gratitude to Dr Ranjan Sarukkalige (Postgraduate Coordinator, Curtin) for taking up the supervisory role during the last term of my PhD. I also like to thank Associate Professor Andrew Whyte (Head of School, Civil and Mechanical, Curtin) for his guidance while working as a sessional academic.

My gratitude also goes to Professor Priyan Mendis, Department of Infrastructure Engineering, Melbourne University, for his guidance to showcase my PhD work to the academic community. I am grateful for his critical input as the co-author to the successful publications in high ranking journals and conferences.

I would like to thank Professor Han-Seung Lee, Department of Architectural Engineering at Hanyang Unversity, ERICA Campus at Ansan, South Korea, for providing the thermal arc sprayed coating specimens as part of my experimental nanoindentation work. I am grateful for Professor Lee's critical input as the co-author to my recent publications related to the coating. I am also thankful for the research training program (RTP) scholarship awarded by the Australian government that supported my PhD work financially.

I would like to take this opportunity to thank the civil department and laboratory staff, including Mark Whittaker, Dr Arne Bredin and others for their help with the laboratory work. I would like to express my gratitude to the civil department administrative staffs for their enthusiastic and kind support on administrative matters and nanoindentation related procurement.

And finally, I thank my loving wife, Yee Jeh, for being by my side during my pursuit of the PhD. She is the silent support of my life, the central pillar of the family. In the shadow of her virtue, I will continually strive for excellence in all my accomplishment and be the role model for my daughters, Rosamund and Rosalind, as they deserve nothing less.

Abstract

Heterogeneous composite materials, whether they exist naturally in sedimentary rocks, or in man-made products such as concrete and thermal sprayed coating, have been widely used in the building and heavy industries as construction material or functional product to protect the critical asset from corrosion and erosion. Despite the effort of extensive testing of these material performance and behaviour over the years, the complex behaviour due to the composite effect have mainly been obscured. In recent years, there is an increasing trend of looking into the heterogeneity of these materials at multiple length scales to study the origin of these engineering behaviours. The application of nanoindentation is one of the recent development that provides the scientific community to access the material individual phase microstructure properties and morphology that otherwise cannot be isolated using the conventional macro-testing method on the macroscopic bulk form. Existing multiscaling theory can relate the material properties across different length scale based on theoretical and analytical approach. The challenge is to have the ability to incorporate the experimental indentation data into the multiscaling algorithm that can be used to predict macroscopic behaviour based on microscale measured properties.

The development of a comprehensive and systematic indentation analysis coupled with a coherent multiscaling framework is the focus of this thesis. This thesis tackles the limitation of conventional indentation solution to obtain the inherent measured properties, i.e. hardness and elastic modulus, through the proposed computational simulated indentation approach. Improvement on indentation measurement is demonstrated by adopting the continuous stiffness measurement (CSM) method to obtain the experimental stiffness directly instead of using a theoretical derivation. By simulating the indentation process with finite element simulation, the relationship of the indentation response and the indentation geometry can be established using dimensional analysis. As a result, this approach enables the prediction of indentation response using machine learning for a wide range of engineering parameters and indentation geometry.

Thermal arc sprayed hybrid coating is adopted as the application to showcase the investigation of the material's heterogeneity at different length scales using the proposed scaling relationships within a multiscaling framework. This multiscaling framework is built upon an arbitrary material model consisting of cohesive-frictional porous material. In this approach, the adoption of mass array indentation with the statistical analysis provides the basis to isolate individual phase properties within the collected indentation data. A downscaling algorithm is presented to quantify the anisotropic behaviour for each phase in the hybrid coating. This algorithm can extract the solid particle properties which represent the building block of the composite material at a lower length scale. The research outcome is consistent with the microporomechanics theory, where mechanical behaviour at a larger length scale is affected by the porosity existing at the lower length scale. The investigation outcome showed that the elasticity properties from individual aluminum and zinc phase remain at isotropic at the smaller length scale although the composite coating is known to exhibit anisotropic indentation result. On the contrary, the anisotropic behaviour is found to originate from the plasticity deformation observed by the highly anisotropic yield parameters, including the cohesion and friction coefficient.

By using a similar multiscaling approach, this thesis follows through the multiscaling procedure onto the larger length scale by presenting an upscaling algorithm to predict the macroscopic coating properties based on the indentation result. The originality of this work comes from

the derivation of an alternative form of the scaling relationship functions compared to the linear comparison composite approach first suggested by Ortega et.al. (2011). The scaling relationship functions are further extended to describe the solid to rigid morphology that can be used to investigate the coating behaviour on the substrate, which the later is assumed rigid. Based on the macroscale bond strength pull test result, the research outcome confirmed that failure in the coating is unlikely to occur within the coating body among the aluminum and zinc phase, as long as the porosity is maintained within the normal porosity range of less than 20%. The research came to the conclusion that the bond failure occurs at the weak interfacial layer between the coating with the substrate. The presence of a weak layer is known to be affected by the residual stress as the coating cooled and deposited onto the substrate. The upscaling algorithm can be used to predict the volume fraction of the weak interfacial layer to the overall volume and its corresponding mechanical properties.

Contents

List of Figures

List of Tables

Chapter 1

Introduction

1.1 General

The science of measuring mechanical properties is a direct response to the need for characterising the physical condition of the material that we encountered in our daily life. For instance, the description of hardness, either hard or soft, can be described as a fundamental human instinct, that is considered intuitive but highly complex to define. It is only relatively new that we attempt to look for a scientific manner to systematically categorize hardness when early researchers conduct test starting about 100 years ago. One of the first pioneers in hardness measurement was Brinell (1901) when he began testing metal hardness by dropping a relatively hard steel ball on them and measure the size of dents. His experiment and findings give birth to the scientific journey of what termed as indentation hardness test to quantify hardness on materials. Brinell's contribution in describing the hardness scientifically, which is based on an impression made by a relatively harder material, has a significant implication on almost every aspect of engineering that relies on the material mechanical response. This very fundamental hardness measurement gives rise to a myriad of hardness test (Fischer-Cripps, 2004) including the Brinell, Rockwell, Berkovich, Knoop and Vickers test. Hardness is commonly defined by pressing a relatively harder material or known as the indenter, with an input force to create an impression onto the intended test subject material. The indentation impression can either be described by the actual pressed surface area or the projected area on indenter depends on the specification of the test being carried out. The ability to categorise material by hardness has a profound influence in every stage in materials extraction, mining, production, manufacturing, building and construction.

The introduction of the indentation test, or better known as nanoindentation, is one of the instrumented indentation techniques that was developed since the early 1970s. This technology has gained growing popularity and becomes widely available these days due to its ability to make a mechanical measurement at the microscale level. During the indentation process, a relatively rigid indenter is indented onto the material's surface, and the corresponding force and displacement are recorded. Earlier work by Loubet et.al. (1984, 1985), Doerner and Nix (1986) and Oliver and Pharr (1992, 2004) are considered indispensable in laying the theoretical groundwork in the mechanism of indentation, which helps to propel the popularity of using indentation technique in small scales mechanical properties investigation. For the past

few decades, nanoindentation has been applied to investigate the mechanical properties for a wide range of industrial manufacturing and building construction materials, ranging from metals, ceramics, polymers, concrete, timber and composite. Many fields and industries, i.e. microelectronics, optical engineering and nanotechnology, benefited from continuous innovation and development, thanks to the insight provided by nanoindentation. There is also a growing interest to extend nanoindentation technology into the food and biological industry. One particular area that has seen promising result with the inclusion of nanoindentation technology is the study of naturally formed complex and heterogeneous materials including naturally formed rocks, shale and cement. Although the latter is considered a man-made recipe, the raw material used to produce cement is, in fact, a naturally occurred materials. There has been promising work carried out in the recent year to decipher the complexity of rock mechanic due to years of geological evolution and complex chemical reaction during the rock formation. There is also a growing interest to figure out the origin of strength in cement paste that has played a critical part in the development of human civilisation dated since its application during Roman's empire in the 1st century.

Over the twentieth century, one of the most exciting trends in the next scientific frontier is to study material at a smaller length scale, from microscale to nanoscale. The ability to extract material's mechanical response at the microscale by indentation contributes to the understanding of how they behave when the measurement is made by many magnitudes smaller. At the same time, there is a growing interest in developing reliable methods to link the mechanical response observed across these lengths scales. Such knowledge has been known to be essential in the development of many fields of science such as biology, material science, paleontology and atmospheric science, where the issues involving multiple length scales become apparent. Currently, the scientific community is facing a formidable challenge to come out with predictive methodologies to analyse advanced materials with ever-increasing complexity. Mechanical behaviour prediction is often tricky due to its complex nature in both advanced human-made materials, i.e. nano-particles infused composite, and naturally existing materials, i.e. shale and rock. How would the individual compounds in the complex microstructure interact with each other that results in the overall observed mechanical behaviour? How would the individual compound's properties differ if we look at a lower length scale? These are the questions that this PhD work is trying to answer.

1.2 Research Aim and Objectives

The overall goal in this research is to derive a systematic approach that consists of both experimental and analytical framework to describe the mechanical properties in complex composite material at different length scale. The following are the key objectives to achieve this goal:

- ■ Nanoindentation Measurement and Outcome

  - To investigate the relationship of stiffness measured using the continuous stiffness measurement with the obtained mechanical response, i.e. modulus and hardness.
  - To derive a stiffness-based reverse algorithm that improves the modulus and hardness measurement using nanoindentation by addressing the geometrical indentation (impression) assumptions.

- Microporomechanical Analytical Solution

  - To incorporate a material mechanical model with the elastic-plastic response into the measured nanoindentation result using a combination of computational simulation and machine learning (artificial neural network)

  - To assess the interaction of multiphase material in a porous morphology at the microscale and relate to the mechanical response measured.

  - To evaluate the effect of porosity on the mechanical response based on the theoretical microporomechanical approach.

  - To derive a multiscale framework with scaling relationship to relate the microscale mechanical response with the macroscale experimental response.

- Application on Coating

  - To assess the mechanical properties of thermal arc sprayed aluminum and zinc coating at the microscale using the nanoindentation and statistical analysis tools.

  - To evaluate the mechanical response of the individual phase and the overall hybrid composite coating.

  - To derive the composite effect of aluminum and zinc phase using the analytical microporomechanical approach.

  - To investigate the scaling relationship of microscale mechanical response obtained using nanoindentation with the macroscale mechanical test, i.e. bond strength test (pull test).

  - To evaluate the anisotropic nature of the coating by modelling the coating as transversely isotropic material and derive the corresponding directional mechanical properties.

1.3   Scope

This work uses the nanoindentation as the primary tool to collect the mechanical response, i.e. modulus and hardness experimentally. Rather than relying on the built-in result from the nanoindentation manufacturer, this thesis explores the fundamental science in the indentation and propose improved alternative solutions to obtain the indentation's response using a combination of computational simulation and machine learning approach. The ability to relate the mechanical response across different length scale requires a multiscale framework that is built on a theoretical material model and analytical scaling relationship. This thesis presents an analytical framework based on the microporomechanics theory to derive the scaling relationships linking the material behaviour at multiple length scales. Thermal arc sprayed hybrid aluminum-zinc coating represents a heterogeneous and multiphase material in this work. The coating mechanical properties are derived using a series of the downscaling, and upscaling homogenization algorithm on several length scales.

1.4   Thesis Outline

This thesis is divided into the following parts and their respective tasks with the desired outcome:

1. Chapter 1 is the introduction of this thesis, where the general background, research aim, research significance are provided.

2. Chapter 2 is to introduce nanoindentation technology and outline how the measurement and outcome are obtained. This chapter first describes the indentation process and outline its basic measured parameters. This chapter then goes in detail to describe the characteristic of the indentation impression, which has a significant effect on how the hardness and the elastic modulus are being calculated. The discussion within this chapter mainly focuses on how accurate is the indentation measurement output preset by the manufacturer's own methodology. The conventional method, which is also the methodology adopted from the machine used in this work, is discussed in length with the assumptions and limitation tabled out. This is then followed by the introduction of a relatively recently developed indentation method, i.e. the continuous stiffness measurement (CSM). The CSM method is chosen and demonstrated extensively in this work due to its unique features, i.e. its ability to measure stiffness continuously during the indentation process. This feature is essential in the forthcoming chapters, where this thesis proposes an improved solution to address the conventional nanoindentation's limitation. It is the intention of this thesis to forego the preset nanoindentation output and adopt a new and enhanced nanoindentation measurement algorithm and a more efficient post-processing capability of mass array indentation result with a significantly large amount of indentation data.

3. Chapter 3 describes the nanoindentation experiment in details and present investigation results for the thermal arc sprayed hybrid aluminum and zinc coating. The experimental nanoindentation adopted in this thesis is based on the mass array indentation approach, where a relatively significant amount of indentation locations are carried out in a structured manner instead of the manually intensive individual selected indentation locations. This chapter further discussed how this approach, coupled with grid indentation framework and statistical analysis methodology, would allow access into the complex heterogeneous composite material properties. The introduction of multiscale material model concept is introduced here that serves as the precursor to the multiscaling homogenization technique in the later chapters. This multiscale model remains as an integral part of the thesis, which is where the scaling and homogenization algorithm is based on. The background and conditions outlined in the multiscale model presented in this chapter are essential to provide an understanding of how the scaling relationship is derived and used to relate the material's microscale mechanical properties with the macroscale behaviour. The experimental investigation of the hybrid coating is presented, followed by the description of the indentation procedure. Finally, the indentation result for the mechanical properties of the coating using the mass array approach is present.

4. Chapter 4 introduces the computational assisted indentation algorithm to address the limitation of conventional indentation highlighted in Chapter 2. Firstly, the concept of empirical scaling and proportionality, which is used to describe the relationship observed in the experimental outcome, is introduced. This concept leads to the adoption of the combination of computational simulation and dimensional analysis approach that forms the foundation framework to rationalise the indentation measurement outcome. This chapter follows by introducing a machine learning algorithm using the artificial neural network to decipher these relationship functions and determine the desired mechanical behaviour such as hardness and elastic modulus. The originality in this work is the

introduction of the stiffness-based inverse algorithm that provides a unique relationship based on the CSM measured stiffness and the indentation geometry. The novelty of this proposed algorithm lies on the fact that it is a relatively simple way to obtain the desired indentation outcome such as hardness and elastic modulus. At the same time, the issue of indentation impression profile is also addressed.

5. Chapter 5 presents the down-scaling algorithm to show how the nanoindentation experimental data can be used to derive a fundamental unit material's properties at a lower scale length. The method used in the downscaling algorithm is based on the microporomechanics theory that describes the composite material as a porous material consists of solid (fundamental unit) and pores. The aim of this chapter is to introduce a downscaling algorithm that can be used to estimate the solid fundamental building block that gives the indentation response collected. This chapter is concluded with the hybrid coating building blocks results presented as the outcome.

6. Chapter 6 presents an upscaling algorithm to predict the coating performance, which is commonly derived using pull-test, based on the experimental nanoindentation result. The upscaling algorithm is based on the microporomechanical theory using the linear comparison composite (LCC) approach. The novelty presented includes a new derivation of the scaling relationship functions compared to the original LCC functions. A macroscale experimental bond strength test has been carried out to measure the pull strength of the coating. The mechanical properties of the coating that correspond to the pull strength is then derived using the upscaling algorithm. It is revealed that an interfacial layer between the hybrid coating and the rigid substrate is the cause of the bonding failure of the coating.

1.5   Research Significance

The outcome of this research aims at contributing to the Curtin nanoindentation team by providing an improved assessment capability to the nanoindentation result and enabling the nanoindentation result for multiscaling analysis of heterogeneous composite materials. The knowledge gained through this PhD thesis is critical to the development of advanced composite materials such as the next-generation high-strength concrete and nanoparticle infused functional coating. Using the analytical approach proposed in this thesis, the process of material development can be carried out using computational simulation instead of the conventional experimental trial and error method. The systematic indentation data collection and post-processing are designed to cover a wide range of material parameters that forms the basis of a complete engineering material indentation database. This accuracy and applicable range of this indentation database will continue to improve as more material's indentation data are learned through the proposed machine learning algorithm. The cumulative benefit of compiling the indentation knowledge through computational simulation and the multiscaling analytical algorithm will push the boundary of future material science research in terms of performance and complexity. Most importantly, this PhD thesis is part of a collective effort in the academic community to gain a better understanding of the fundamental science in terms of material's behaviour and performance correlation with the material's morphology and microstructure at different length scale.

Chapter 2

Nanoindentation

2.1 Introduction

This chapter presents the essential background of the nanoindentation technology, together with its mechanical process and the expected outcome. The ability to understand the current nanoindentation capability and investigate its limitation is part of the current research aim. Detailed explanation on each of the indentation's parameters from the indentation process is put forward. The derivation of the corresponding mechanical properties determined from the indentation process is presented. Subsequently, the limitation in the derivation of the mechanical properties is tabled. The notation and parameters described in this chapter form a consistent base reference to all the subsequent methodologies proposed in this thesis. A section is devoted to the continuous stiffness measurement (CSM), which is a crucial investigation tool used in the research for this thesis.

2.2 Indentation Parameters

The indentation process involves two stages, i.e. loading and unloading stage (see Figure 2.1. The load path taken during the loading process is represented by the loading curve, where it starts when the indenter is indented onto the initial material's surface, i.e. zero displacements. The loading cycle is complete when the indenter reaches its intended maximum force (P) or maximum displacement (h_{max}), depending on the type of method used. The force will return to zero when the indenter separates from the material surface. The distance from the initial surface to the final depth recorded at the zero-force is also known as the residual depth (h_f). Since the unloading process is due to elastic deformation (Oliver and Pharr, 1992), the distance rebound from the final depth to the residual depth is, therefore, the elastic deformation (h_e). As a result, the residual depth is also a measure of plastic deformation. The unloading stiffness (S_u) is measured by the gradient of the upper portion unloading from maximum force (P_{max}). When the indenter is at the h_{max}, the depth at which the indenter remains in contact with the sample is known as the contact depth (h_c).

In general, there are two types of indentation cross-section profile, i.e. sink-in and pile up profile (see Figure 2). A sink-in profile refers to the condition when the contact edge between
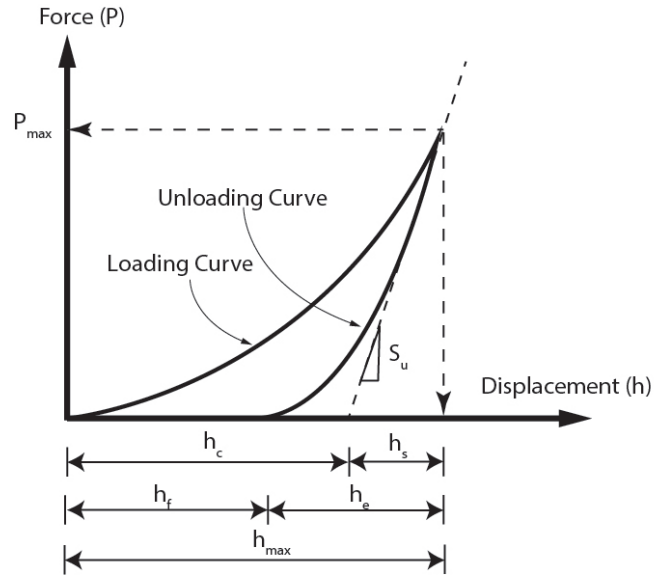
Figure 2.1: Nanoindentation loading and unloading curve

the indenter and the sample's surface is below the initial surface when the indenter is at its maximum depth. In other words, the contact area is below the initial surface ($h_c/h_{max} \leq 1$). The distance between the contact depth and the initial surface is known as the sink-in depth (h_s). On the other hand, a pile-up profile refers to the condition where the contact edge between the contact edge of the indenter and the sample's surface is above the initial surface when the indenter is at its maximum depth. The pile-up depth (h_p) is the distance in between the top of the indenter-sample contact edge and the initial surface. In this scenario, the pile-up surface is higher than the initial surface. Therefore, the contact depth is higher compared to the maximum depth ($h_c/h_{max} > 1$). The pile-up depth (h_p) refers to the distance between the top of the pile-up surface to the initial surface. Note that the contact depth has a significant role in the determination of both elastic modulus and hardness, which will be elaborated further in subsequent sections.
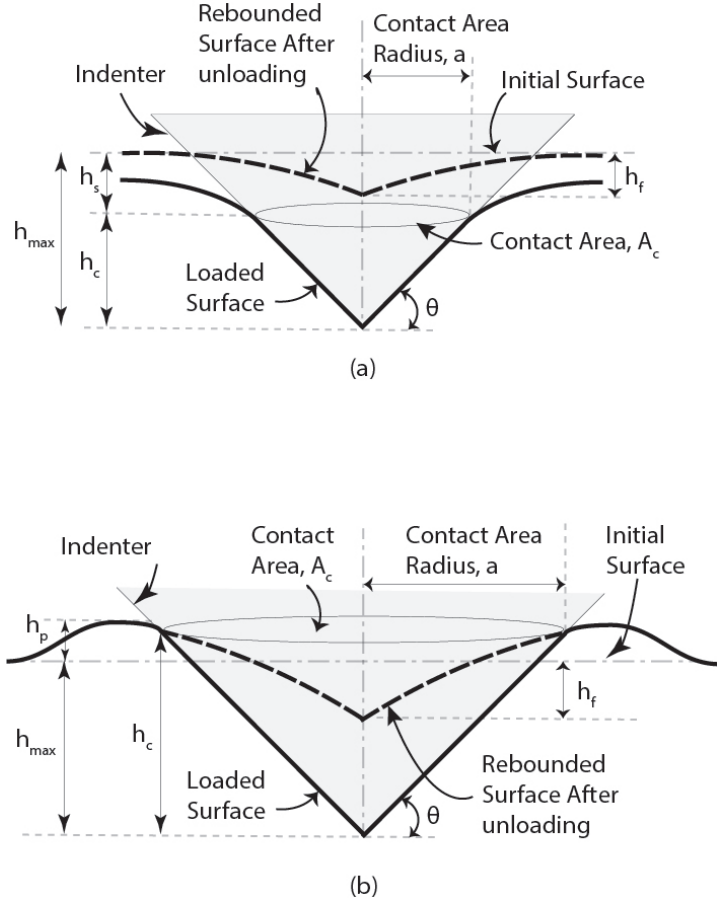
Figure 2.2: Indentation cross-section: (a) sink-in profile (b) pile-up profile

2.3 Conventional Method

Nanoindentation is commonly used to identify the material's elastic modulus and hardness. One of the popular method used to determine these two parameters is the Oliver-Pharr method (Oliver and Pharr, 1992, 2004). Conventionally, the loading curve has a linear relationship (Equation 2.3.1 with the square of the indentation depth (h) with a loading curve gradient (C) (Cheng and Cheng, 2004).

$$P = Ch^2 \tag{2.3.1}$$

The key feature in the Oliver-Pharr method is the introduction of a power-law function to describe the unloading curve, shown in Equation 2.3.2. This simple approach enables a wide range of material's indentation response to be described by only two power-law fitting constants (α and m). In this case, the unloading stiffness can be obtained by differentiating Equation 2.3.2, i.e. $S_u = dP/dh$, provided the constants α and m are known. When this is not the case, one has to resort to graph fitting to evaluate the unloading stiffness. It is noted here that the Oliver-Pharr method is found limited because graph fitting is a subjective exercise leading to inconsistency outcome. This PhD work intends to address this issue by proposing an alternative solution outlined in Chapter 3.

$$P = \alpha \left(h - h_f \right)^m \qquad (2.3.2)$$

Two pre-requisite parameters must be made known, i.e. material's stiffness and indenter to the material contact area, to determine both the elastic modulus and hardness. The term effective modulus, first introduced in the Oliver-Pharr method, is related to the effective elastic modulus of the material (E^*), the elastic modulus of the indenter (E_i) and the Poisson's ratio for the material (v) and indenter (v_i).

$$\frac{1}{E^*} = \frac{1 - v^2}{E} + \frac{1 - v_i^2}{E_i} \qquad (2.3.3)$$

The effective elastic modulus is directly related to the unloading stiffness (S_u) and contact area (A_c) (Equation 2.3.4). This equation can be traced back to work by Sneddon (Sneddon, 1965) who first introduced a solution for the shape an indentation impression made by an axisymmetric rigid indenter by using a solid revolution of non-linear function in an elastic half-space. Since Sneddon's assumption is in the elastic half-space, the indentation impression always follows a sink-in profile, where the h_c is less than the h_{max}.

$$S_u = \frac{dP}{dh} = \frac{2}{\sqrt{\pi}} E^* \sqrt{A_c} \qquad (2.3.4)$$

The contact depth can be determined by Equation (2.3.5) where ϵ=0.75 is recommended by Bolshakov and Pharr (1998). Note that in this equation, the value of h_c will always be less than the maximum depth as the Oliver-Pharr method is based on a sink-in profile. In other words, the accuracy in the Oliver-Pharr method is limited when the material exhibits a pile-up profile.

$$h_c = h_{max} - \epsilon \frac{P}{S_u} \qquad (2.3.5)$$

Based on the geometry of the conical indenter contact to the sample surface, the contact area (A_c) can be determined by

$$A_c = \pi a^2 = \pi h_c{}^2 tan^2 \theta \qquad (2.3.6)$$

Note that Equation 2.3.6 shows that the contact area can be represented by a shape constant that is dependent on the type of indenter and the contact depth (h_c). For the case of a Berkovich indenter, a shape constant can be derived from an equivalent conical indenter and impose an area function that is a function of the contact depth (h_c), as shown in Equation (2.3.7) (Oliver and Pharr, 1992). The first coefficient of this area function is the equivalent shape constant for a Berkovich indenter. The rest of the coefficients are there to represent an imperfect indenter profile, i.e. a blunt indenter. The coefficient in this area function can be obtained during the calibration of the Berkovich indenter by independent measurement to consider the blunting of the indenter tip.

$$A_c = 24.5h_c{}^2 + C_1h_c + C_2h_c^{\frac{1}{2}} + C_3h_c^{\frac{1}{4}} + \cdots + C_8h_c^{\frac{1}{128}} \tag{2.3.7}$$

Once the contact area (A_c) is defined, the hardness can be determined from

$$H = \frac{P}{A_c} \tag{2.3.8}$$

In nanoindentation, the contact area is a critical parameter required for calculating hardness but remained difficult to determine (Bolshakov and Pharr, 1998). This is because the contact depth can only be approximated by assuming a sink-in contact profile, as shown in Equation (2.3.5) but cannot be directly measured by the instrument during the indentation process. For this reason, there is a need to provide an improved method to determine the contact area in nanoindentation to cover material not only with the sink-in profile, but also the pile-up profile which has been known to occur in a wide range of metals (Bolshakov et al., 1996). For this reason, an alternative solution presented in Chapter 3 intends to address the limitation in the Oliver-Pharr method to determine the true contact area.

2.4   Continuous Stiffness Measurement

The conventional nanoindentation measured both force and displacement during the indentation process. A relatively new tool has been introduced, namely, the continuous stiffness measurement (CSM) method that can measure the stiffness as an additional response parameter (Oliver and Pharr, 1992, 2004). This is made possible by imposing a small dynamic oscillation on the indenter so that the force and displacement signal can be measured dynamically together with the corresponding amplitude and phase (Pethica and Oliver, 1987). To obtain the dynamic response from the sample, the stiffness of the mechanical system, also known as the frame stiffness, has to be isolated when measuring stiffness at the indenter tip. To understand the interaction between the frame stiffness and the measured stiffness at the indenter tip, a simplified dynamic model is presented in Figure 2.3.
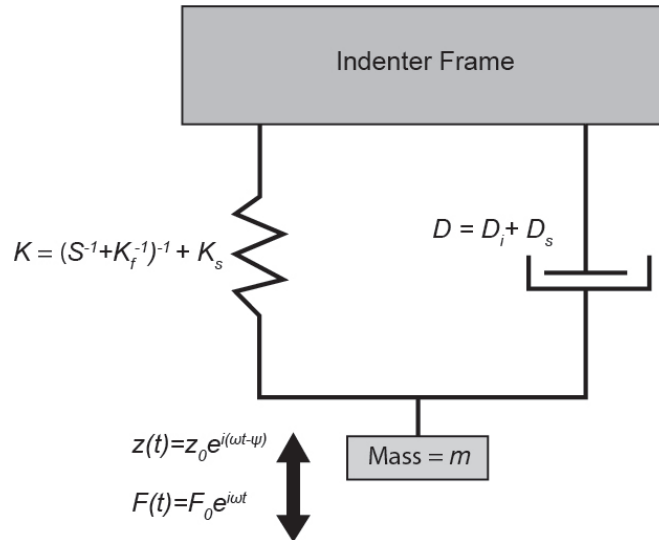
Figure 2.3: Simplified Continuous Stiffness Measurement Dynamic Model. Adapted from Oliver and Pharr (1992)

Equivalent damping (D_e) is a combination of the indentation head damping (D_i) and the contact damping (D_s). The equivalent stiffness (K) is a function of the contact stiffness (S) at the maximum indentation depth, the frame stiffness (K_f) and the supporting spring's stiffness (K_s) (Equation 2.4.1). It is worth noting that the equivalent stiffness of the system is not a constant but changes because the contact stiffness (S) changes during the indentation while the frame stiffness and the supporting spring's stiffness are constant. In other words, the natural frequency (ω) varies throughout the indentation process following the changes in contact stiffness (S) even though the input excitation frequency imposed is fixed. The supporting spring, where the indenter is hanging freely, is constant because the indenter is not restraint in any manner until it is in contact with the sample.

$$K = \left(\frac{1}{S} + \frac{1}{K_f}\right)^{-1} + K_s \tag{2.4.1}$$

The imposed dynamic force (P_d) and displacement (z) within a simplified harmonic oscillator model can be represented in a differential equation, as shown in Equation 2.4.2. On the other hand, the same force and displacement can form a function with respect of time (t) together with the natural frequency (ω) and phase angle (ϕ), see Equation 2.4.3 and 2.4.4.

$$F(t) = m\ddot{z} + D_e\dot{z} + Kz \tag{2.4.2}$$

$$P_d(t) = F_0 e^{i(\omega t - \phi)} \tag{2.4.3}$$

$$z(t) = z_0 e^{i\omega t} \tag{2.4.4}$$

Substituting Equation 2.4.3 and 2.4.4 into Equation 2.4.2 yields

$$\frac{P_d}{z_0} = \sqrt{(K - m\,\omega^2)^2 + (\omega D_e)^2} \tag{2.4.5}$$

$$tan\,\phi = \frac{\omega D_e}{K - m\,\omega^2} \tag{2.4.6}$$

The force amplitude (P_0), displacement amplitude (z_0) and phase angle can be measured during the dynamic indentation process. In other words, the dynamic displacement oscillates at the same frequency as the force that lags by a phase angle. Hence the equivalent stiffness (k) and damping (D_e) can be solved simultaneously by Equation 2.4.5 and 2.4.6. Finally, the contact stiffness (S) and contact damping (D_s) can be solved by Equation 2.4.7 and 2.4.8 (Selvadurai, 2019).

$$S = \left(\frac{1}{\dfrac{P_0}{z_0} cos\,\phi - (K - m\,\omega^2)} - \frac{1}{K_f} \right)^{-1} \qquad (2.4.7)$$

$$D_s\,\omega = \frac{P_0}{z_0} sin\,\phi - D_i\,\omega \qquad (2.4.8)$$

Unlike the conventional method where stiffness is derived from a simplified method based on elastic modulus and the elastic contact assumption, stiffness determined from CSM is a measured product based on a dynamic approach, and therefore often referred to as the dynamic stiffness. Previous literature has shown that the dynamic stiffness has a linear relationship (Equation 2.4.9) with the indentation depth with a gradient of C_h and the indentation force is linearly related to the square of the dynamics stiffness with a gradient of C_p. (Joslin and Oliver, 1990, Wang and Rokhlin, 2005, Wang et al., 2005).

$$h = C_h\,S \qquad ; \qquad P_d = C_p\,S^2 \qquad (2.4.9)$$

2.5 Summary and Conclusion

In the conventional indentation process, the unloading stiffness is a derived parameter that depends on the elastic modulus and the contact area assuming a simplified elastic contact profile. This represents the first limitation in conventional post-processing of indentation result where this conventional approach could not be used to represent the wider range of material that exhibit plasticity during the indentation process. The second limitation is the simplification adopted to determine the contact area using an area function that does not take into account the material's pile-up. The challenge around this issue is that the contact area cannot be readily monitored and measured due to the limitation in current instrumentation technology.

The dynamic stiffness determined using the CSM method address the first limitation where stiffness is no longer required to be derived. Instead, it can be readily measured. The CSM method is a critical element in this thesis with the provision of the measured dynamic stiffness as an additional parameter on top of the force and displacement. The dynamic stiffness serves as an enabler role to relate the measured experimental result with the proposed alternative methodologies proposed in the next chapter in this thesis to derive the elastic modulus, hardness and contact area.

Chapter 3

Experiment

3.1 Introduction

This chapter presents the experimental indentation procedure carried out based on the grid indentation approach. The theoretical background for the grid indentation and the statistical approach are elaborated. Thermal arc sprayed coating representing a heterogeneous and multi-phase material is the primary experimental subject. The sample preparation and the indentation procedure are outlined. The outcome with regards to the sample's constituents investigation and imaging are presented.

3.2 Grid Indentation Analysis

Heterogeneous and multi-phase composite materials commonly contain several mechanically significant phases where each individual phase property has a considerable effect on the overall material performance. While the instrumented indentation technique is useful in a homogeneous and monolithic material, using it on these composite materials poses new challenges.

Conventionally, the indentation process is carried out together with an optical microscope or imagining tool with the conjunction of characterisation tool such as EDS-SEM to locate the indentation visually to know what material is indented on. This approach is obviously difficult and not suitable to be used in a large-array indentation investigation. For the case of metal, it is common to etch the metal surface with acids to reveal the feature when viewed under the optical microscope. However, not all phases can be differentiated with the etching technique, or the indentation is simply too small to be seen under the microscope. Any surface post-processing technique such as polishing and etching can result in alteration in surface roughness that may hinder the measurement accuracy. In addition, shallow-depth indentation is often influenced by the effect of surface roughness where inconsistent contact profile between the indenter and the sample surface can result in measurement errors.

The development of grid indentation technique originally indented on cementitious materials (Constantinides et al., 2006, Ulm et al., 2007) can address the challenges mentioned above. When used together with the statistical deconvolution technique, the grid indentation technique enables the mechanical properties of individual phases to be measured without the need to have

visual verification. Provided that the indentation depth is much smaller than the size of the particular material phase, a single indentation location is expected to capture the mechanical response from the single-phase entity. By contrast, if the indentation depth is much larger than the largest size of any of the material phases, the indentation result would represent an overall composite response. Therefore the choice of indentation depth must be carefully selected to coincide with the intended size of the element where the mechanical response is desired. Provided the individual material phase's length scale is chosen correctly, this technique can derive volume fraction information for each composite material phase. The ability to do so enables information on not just the mechanical properties but the microstructure morphology to be obtained. This is the reason why the grid indentation analysis is central to this work. This technique is used extensively in the experimental nanoindentation data collection to investigate the scaling relationship of porosity with the mechanical properties.

3.3 Indentation Length Scales

The purpose of grid indentation analysis is to enable a way to investigate the properties of heterogeneous materials using nanoindentation based on the concept of homogenization techniques. The classical homogenization techniques (Reuss, 1929, Sachs, 1928, Voigt, 1889) from the early days is mainly used to find a replacement of heterogeneous complex body by a fictitious homogeneous one so that the two behaves mechanically at a similarly way at the global scale. These early work are focused in finding a numerical bound to describe the problem, which subsequently leads to the analytical solution proposed by Hill (1965) that effectively gives rise to the field of "continuum micromechanics". The goal of applying the continuum mechanics is to derive the macroscale response of a material system from its equivalent microscale one. Conventionally, the material macroscale constitutive behaviour can be determined by carrying out experiments on a macroscale sample. Alternatively, the homogenization approach can be adopted to derive the macroscale constitutive behaviour by solving a boundary value problem mathematically on a theoretical sample. This theoretical sample is referred to a representative volume element (RVE) of a porous entity that is a made-up entity of homogeneous mechanical response and fulfils the scale separability condition (Constantinides et al., 2006).

$$d \ll \mathscr{L} \ll \mathscr{D} \tag{3.3.1}$$

where $\mathscr{L}$ is the characteristic size of the RVE, which must be much larger than the characteristic size of in-homogeneity and deformation mechanism, d, contained in the RVE. In this case, d can be defined as the maximum size of the individual phase particle within the RVE. At the same time, The RVE size must be much smaller than the strain gradient variation, $\mathscr{D}$, in the microstructure.

Consider a porous RVE that consists of solid-porosity or skeleton-fluid, which is used to describe the composite material constitutive behaviour, i.e., geometrical (strain) and mechanical response (stress). The length scale representing each scale level has to be chosen carefully to satisfy the scale separability condition. In this case, the the indentation depth is selected to have the same length scale as the RVE so that $d \ll (\mathscr{L}, h) \ll \mathscr{D}$. As shown in Figure 3.1, the separate length scale is illustrated as level 2, level 1 and level 0 in descending order. It is postulated here that the material constitutive behaviour across these multiple scales are

considered equivalent, where the continuum micromechanics field stress and strain laws are met. The concept of "composite" is treated differently at every scale level. At level 2, which is macroscopic structure level, the RVE is represented as a collection of superposition of individual phases. At level 1, referred to in this work as the microscale level, the RVE is represented as a heterogeneous entity that contains all the different phases. The smallest scale level is level 0, where the material system is represented as a solid particles that serves as the building block of the material system. In the context of the hybrid aluminum and zinc coating, this building block is represented by the individual aluminum and zinc crystallised grain that was known to form the basic crystal structure for thermal sprayed metallic coating (McPherson, 1989). The indentation grid analysis relies on the concept of continuum micromechanics framework where the heterogeneous body can be represented by the RVE that has an equivalent mechanical response with the heterogeneous body (Zaoui, 2002). In other words, the mechanical response of the heterogeneous body derived at level 2 would achieve average values that is the same as the RVE's mechanical response measured at level 1, see Figure 3.2.
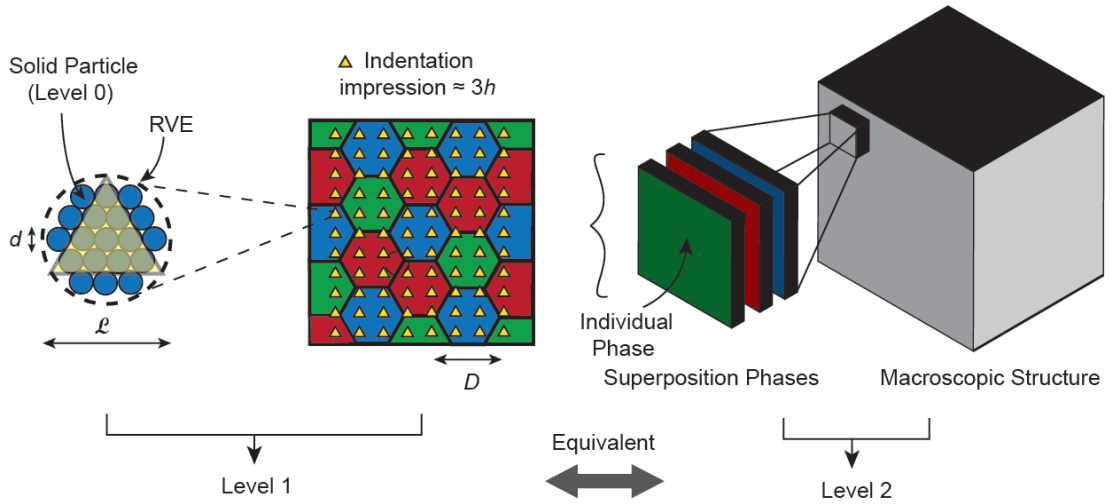
Figure 3.1: Small-scale indentation tests carried out on a heterogeneous composite at level 1. The indentation depth, h is taken such that the scale separability condition is met as shown. In this case, h is taken at the same scale length as $\mathscr{L}$ as the RVE.

In the context of nanoindentation experiment, a small scale indentation test is carried out, which is referred to the indentation on a multi-phase heterogeneous material that has an individual phase's characteristic length scale ($\mathscr{D}$), and letting the indentation depth (h) to be $h = \mathscr{L}$ in the scale separability condition. As a rule of thumb when $h \ll \mathscr{D}$, i.e. h should not be bigger than $1/10$ of $\mathscr{D}$ (Buckle, 1973), a large nanoindentation test array ($N \gg 1$) can access the individual composite phase's mechanical properties. This is achieved by selecting a grid spacing that is larger than the size of the indentation impression, generally accepted as 3h to avoid interference between each indentation location. This way, each indentation location has no statistical bias for the spatial distribution of the in-homogeneity found in the multi-phase body. Thus, the summation of surface fraction identified from each indentation's onto a specific phase is equal to the probability of indenting into the same phase. In other words, the volume fractions for each phase can be shown as:

$$f_j = \frac{N_j}{N} \qquad ; \qquad \sum_{j=1}^{n} N_j = N \qquad (3.3.2)$$

Where N_j is the total number of indentation on material phase j, N is the total number of the entire grid indentation carried out, f_j is the volume fraction of material phase j that has a distinct mechanical property.

The indentation response obtained using this approach is, in essence, the average mechanical properties of each individual phase derived using established statistical relationship. This average value is effectively the mean value of a probability distribution frequency for the specific material's phase with respect to its mechanical properties. The schematic is shown in Figure 3.2. The methodology to arrive at the individual phase mechanical property characteristic, as shown, is through the use of the statistical deconvolution technique (Constantinides et al., 2006, Ulm et al., 2007).
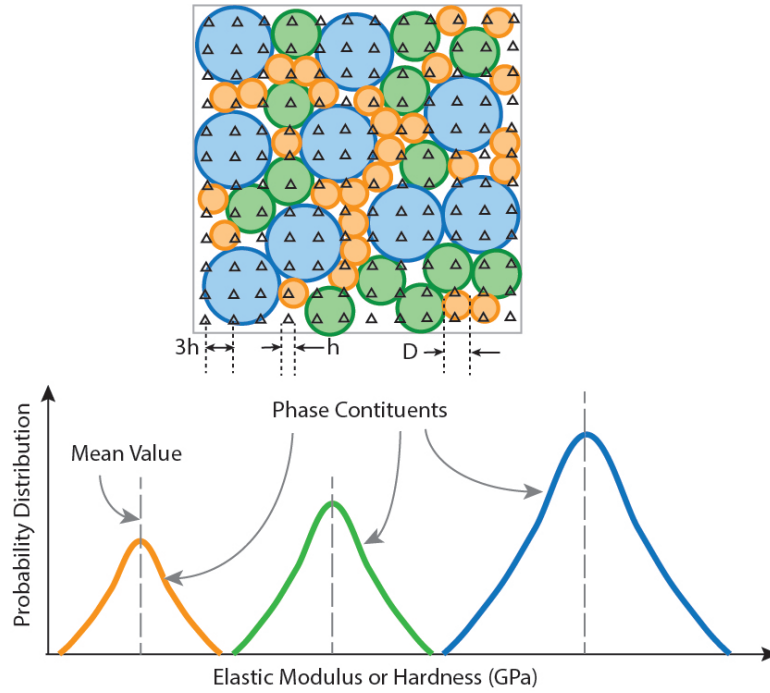
Figure 3.2: Schematic showing grid indentation technique, or mass array indentation, applied on multi-phase composite heterogeneous material. When h $\ll \mathscr{D}$, each indentation is able to access individual phase constituent properties. The outcome can be presented in a probability distribution for the frequency on each phase constituents with its mechanical properties.

3.4   Statistical Deconvolution Technique

The outcome of the grid indentation analysis, i.e. indentation modulus (M) and hardness (H) are considered randomly generated population that can be approximated by the normal or Gaussian distribution. As a result, the theoretical normal distribution $(\Phi_j^T(X))$ of indentation mechanical property $X = M, H$ for phase j has a mean value of μ_j and a standard deviation of σ_j for N number of indentation locations on a material that has n phases.

$$\Phi_j^T(X) = \frac{1}{\sigma_j\sqrt{2\pi}} \int_{\infty}^{X_i} exp\left[\frac{-(s-\mu_j)^2}{2\sigma_j^2}\right] dt \quad for \quad i \in [1, N] \text{ and } X = (M, H) \qquad (3.4.1)$$

If the individual phases within the same indented material follows the same normal distribution, the overall frequency distribution of the mechanical properties, $X = M, H$ should follow the

following relationship with the theoretical cumulative distribution function ($C^T(X)$), or CDF and volume fraction for each phase (f_j), expressed as:

$$C^T(X) = \sum_{j=1}^{n} f_j \, \Phi_j^T(X) \tag{3.4.2}$$

Similarly, an experimental cumulative distribution function can be obtained by sorting each of the measured mechanical property data point, X=M,H from:

$$C^E(X) = \frac{i}{N} - \frac{1}{2N} \qquad for \quad i \in [1, N] \text{ and } X = (M, H) \tag{3.4.3}$$

There are 5 unknowns, i.e. f_j, μ_j^M, σ_j^M, μ_j^H, σ_j^H that can be determined by utilizing a minimization function as shown, which aims to minimize the difference between the experimental CDF (C^E) with the theoretical CDF (C^T).

$$min \sum_{i=1}^{N} \sum_{X=(M,H)} \left[\sum_{j=1}^{n} C^T(X) - C^E(X) \right]^2 \qquad where \quad \sum_{j=1}^{N} f_j = 1 \tag{3.4.4}$$

An additional constraint is required within the deconvolution algorithm to maintain a clear contrast among the different mechanical properties by avoiding two consecutive normal distribution functions to overlap each other. This is achieved by applying the following condition:

$$\mu_j^X + \sigma_j^X \leq \mu_{j+1}^X + \sigma_{j+1}^X \qquad where \, X = (M, H) \tag{3.4.5}$$

3.5 Coating Sample Preparation

Thermal arc sprayed hybrid (aluminum and zinc) coating is used as experimental heterogeneous material in this work. The coating samples are prepared and supplied by Hanyang University, led by Professor Han-Seung Lee. The raw material for the coating consists of commercially pure Aluminum and Zinc (99.95 wt. %) wires with 1.6 mm diameter. The substrate is made of sandblasted mild steel plate. Arc spraying method using a twin feeding spray gun is used to create the coating. The spraying process parameters used to prepare the sample used in this work is shown in Table 3.1.

Table 3.1: Spraying parameters for the thermal arc metal spray coating

Parameters (unit)	Value
Air Pressure (bar)	4–6
Spraying Distance (cm)	15–25
Spraying Voltage (V)	30
Spraying Current (A)	200

In this method, the raw material wires are fed into the gun by a wire driving mechanism. As the material passed through an arc point powered by high current power source, the metal is melted, atomised and propelled forward by a hot jet of compressed air. As the molten metal is deposited on the substrate surface, the molten droplet solidifies into a thin layer of splats as they continue to cool down. Depending on the spraying process parameters, the individual splat has a size in the range of 1 to 20 μm and form a uniform and relatively fine-grained polycrystalline metallic structure (Davis et al., 2004). These solidified splat builds up in layers following the continuous stream of the molten droplets to form a complex intergranular microstructure with voids and cracks (Ang and Berndt, 2014). The porosity entrenched in the coating is due to the nature of the intergranular morphology and the presence of defects, i.e. un-melted or partially molten metal and oxidation from en-trained air. Scanning electron microscope (SEM) images have been taken on the cross-section and the surface, shown in Figure 3.3.
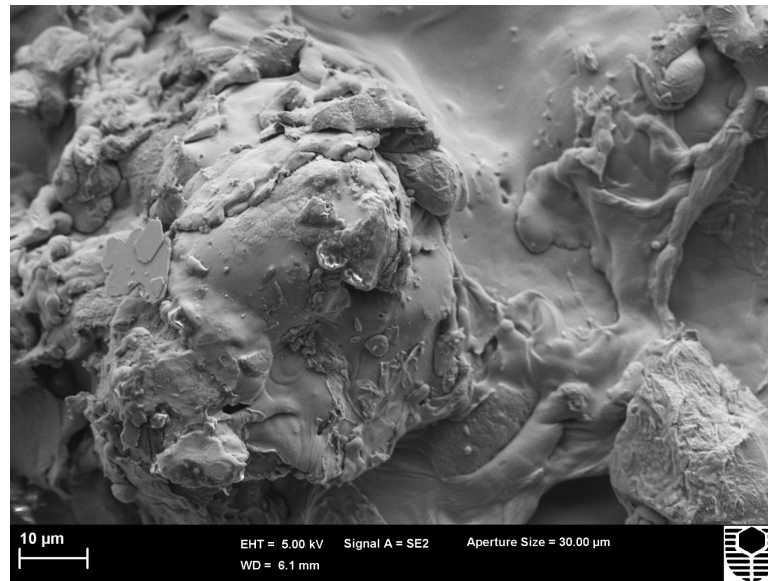
Figure 3.3: Scanning electron microscope images for the coating surface at 10 μm

3.6   Coating's Porosity Estimation

A sample of the coating cross-section has been scanned using the EDS, and the results are shown in Figure 3.4. The captured image shows two distinctly contrast materials, which have been confirmed by SEM-EDS scan as aluminum (with the darker contrast) and zinc (with the lighter contrast). The coating cross-section shows high porosity and irregular thickness, with some part being less than the desired 100 μm. This cross section image shows a deposition with uneven surface and thickness where voids are visible between and inside the splats. This is condition is common in the real world where the coating is sprayed and deposited under a turbulent spraying condition. While it is not the scope of this work to identify the factors affecting the coating's poor quality, this work intends to demonstrate how the presence of the porosity can be used to define the coating strength and other mechanical properties. The porosity ratio to the solid coating volume has can be estimated using the colour intensity segregation tool from Adobe Photoshop and determined as 18%. This result is considered high compared to the porosity reported in the thermal sprayed coating that has a range of 10% to 20% (Zhang et al., 2009).

18
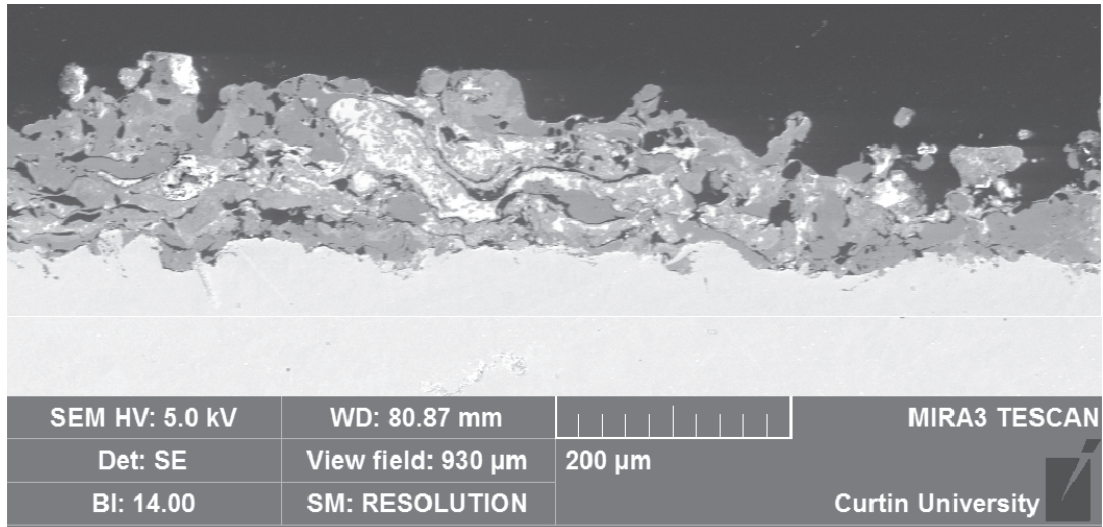
Figure 3.4: Cross-section of aluminum-zinc coating

3.7 Bond Strength Test

A bond strength test, or known as pull test for the coating has been carried out and reported previously by Lee et al. (2018). The results are shown in Table 3.2. The bond strength test was carried out in accordance to KS F4716 (KSF4716, 2001). It is noted that the coating used in this work is supplied from the same batch of the coating. Therefore, the previously reported bond strength is assumed applicable in this work. The average bond strength observed was 3.93 MPa, which is considered low for thermal arc sprayed coating that has a typical range of bond strength of 6-10 MPa (Varacelle et al., 1998). Based on the scanned image, the low bond strength captured may be due to the relatively high porosity found in this batch of the coating.

Table 3.2: Bond Strength for Aluminum-Zinc coating.
(Reproduced with permission from Lee et al. (2018))

Sample Number	Bond Strength (MPa)
1	4.00
2	3.99
3	3.80
4	3.92
Average	3.93

3.8 Nanoindentation Preparation and Execution

The microscale mechanical properties for the coatings were investigated using nanoindentation. The coating sample is first to cut into 10 mm × 10 mm pieces. This is followed by applying epoxy resin on the coating surface to fill up the porosity. To achieve an acceptable surface roughness, the samples are polished in line with the standard ASTM E3-11 with additional manual polishing steps using diamond particle suspension liquid until the acceptable surface roughness is obtained ($\leq 10 \mu$m). Approximately 500 nanoindentation locations are carried out using the Keyside G200 nanoindenter with a Berkovich indenter and the continuous stiffness method. The nanoindentation experiments are conducted in the Curtin University nanoindentation facility.

3.9 Microstructure Investigation

To verify the composition of the coating material, chemical microanalysis has been carried out using the Energy Dispersive X-Ray Spectroscopy (EDS) technique in conjunction with SEM. The outcome of the EDS-SEM, is shown in Figure 3.5. The result indicates that the coating consists of predominantly two phases, namely aluminum and zinc. Further investigation was carried out to find out the coating characteristic by using electron backscatter diffraction (EBSD). The outcome of EBSD, as shown in Figure 3.6, confirmed the aluminum and zinc composition, and the image can reveal the overall size of the grain and the variation in their orientation. Figure 3.6(a) shows the interface of the aluminum and zinc phase with the mild steel substrate. The aluminum phase is highlighted as blue while the zinc phase is highlighted as red. The back area is the voids occupied in between the deposited molten plats and the defects. Based on the colour contrast, it is observed that the intergranular structure is formed as the aluminum and zinc spats solidified on top of each other. An intergranular structure is observed when small particles of zinc are infused into the aluminum splat, as shown by the red dots exist within the blue region. For the purpose of this work, the splat that forms the zinc infused intergranular microstructure is to be treated as a coherent material. It is shown in the later chapters that the indentation carried out into the splat at the microscale reflects the mechanical feature from the dominant material phase. However, how much the coating mechanical properties are affected by the intergranular structure remained unknown, which is beyond the scope of this PhD work. On this note, this presents a future investigation opportunity to investigate the coating's intergranular structure at the nanoscale experimentally.
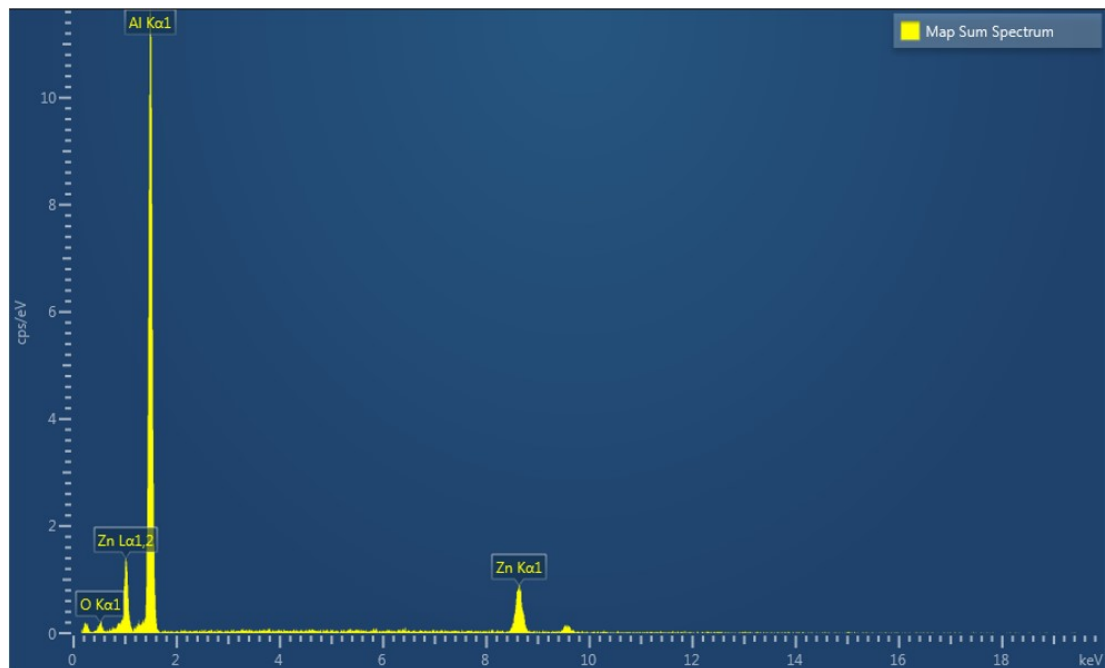
Figure 3.5: Aluminum-Zinc coating phase characterisation by SEM-EDS

The EBSD reveals a relatively fine grain composition relative to the bulk material with a wide range of grain size measured at 25 μm and smaller. This observation is expected as the molten metal particle underwent extensive plastic deformation after exposure to high heat and kinetic pressure during the spraying process (Deshpande and Sampath, 2005), similar to the annealing process. Another observation in the coating grain structure is the variation of grain orientation

which is also common in thermal sprayed coatings, bulk metals and alloys (Stoudt et al., 2011, Wang et al., 2015). Grain orientation is known to contribute to the variation in mechanical properties at the nanoscale level. This may be the reason that the indentation result has broad properties range. However, it is beyond to scope of this PhD work to investigate the effect of grain orientation on the indentation result. The challenge in investigating thermal sprayed coating is the complex and heterogeneous nature of the microstructure, as evidence in Figure 3.6(c). From the practicality point of view, there is a significant challenge to identify individual grain location and its mechanical properties using nanoindentation in this circumstances. For this reason, the grid indentation approach is adopted so that the grain's properties can be determined using a statistical representation.
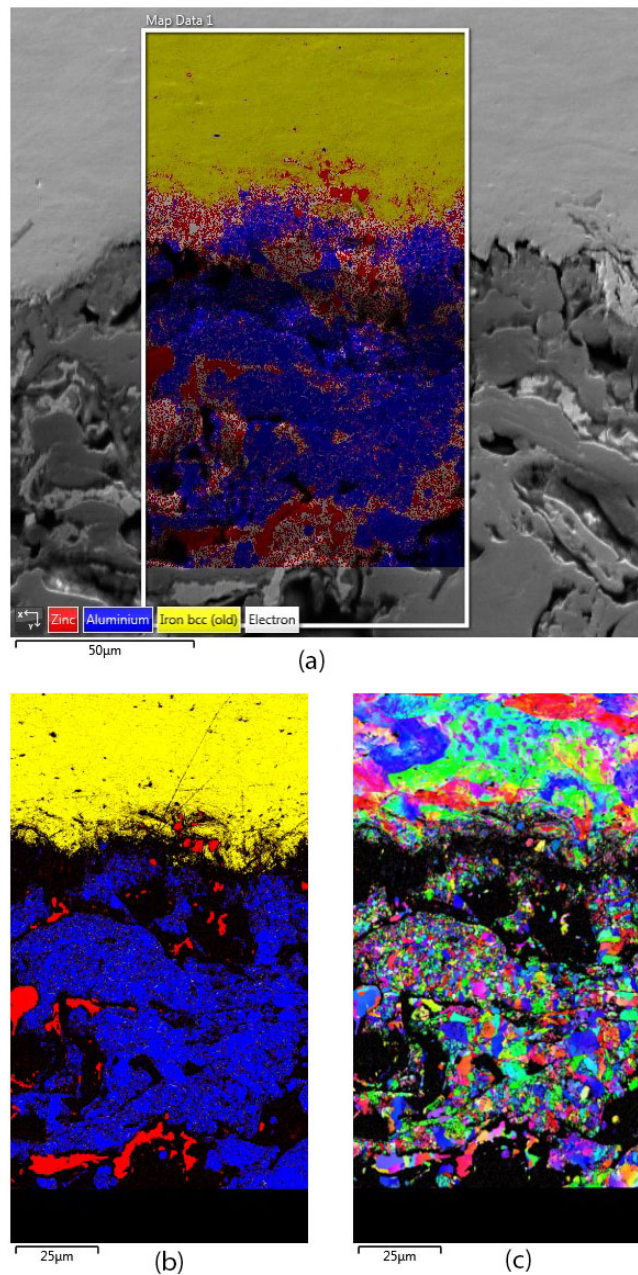
Figure 3.6: EBSD carried out on thermal sprayed Al-Zn coating cross-section: (a) snapshot taken on the coating with iron steel substrate (b) phase contrast showing aluminum (blue), zinc (red) and iron (yellow) (c) grain size and orientation

3.10 Statistical Deconvolution Outcome

Based on the statistical deconvolution methodology presented in the previous section, the outcome is given in Table 3.3. The deconvolution result is plotted in terms of the cumulative distribution function, as shown in Figure 3.7 and the cumulative distribution functions plots, as shown in Figure 3.8. The histogram showing the number of counts and their respective value is shown in the background as a vertical bar chart. The coating sample is represented by a transversely isotropic model that consists of a transversely isotropic plane ($x_1=x_2$) and a rotational symmetric axis (x_3). The rotational symmetric axis coincides with the spraying and indentation direction. The x_3 direction mechanical properties are directly obtained from the experimental indentation values. The x_1 direction mechanical properties are derived from the computational simulation. The details of how the x_1 mechanical properties are obtained are outlined in Chapter 5. For this particular batch of indentation locations, the outcome shows that the majority of the indentation location hit the zinc phase. The values from the indentation direction (x_3) are relatively larger compared to the transverse direction (x_1 or x_2). This observation is in line with the outcome shown from Chapter 5, where dominant mechanical properties are obtained from the indentation or spraying direction. Another observation made from these result is that the coating elastic modulus for both the phases is lower compared to the bulk material. In the case of aluminum in the (x_3) direction, the elastic modulus, E and hardness, H determined to have a mean value and standard deviation of 26 ± 16 GPa and 0.8 ± 0.5 GPa respectively. These values are found to be reasonable within the range $E = 47 – 90$ GPa and $H = 0.7 – 1.0$ GPa based on existing literature (Kang et al., 2014, Lim et al., 1999, Van Steenkiste et al., 2002). For zinc, the reported elastic modulus is 62 - 75 GPa (Guzman et al., 2000, Sundararajan et al., 2013) and the hardness has a range of 0.45 - 1.86 GPa Jiang et al. (2008). However, the reason why the mechanical properties of the coating are lower than the bulk material remains unknown. These cases have high standard deviation, which could be due to the high variation in the state of individual metal grains, which can be observed from the EBSD grain orientation result in Figure 3.6(c). Other materials also found to exhibit relatively high indentation data scatter as observed in existing literature (Constantinides et al., 2006, Ulm et al., 2007). In this PhD work, it is shown that the material porosity has a direct effect on the mechanical properties found. This hypothesis is further explained in the subsequent chapters.

Table 3.3: Statistical deconvolution outcome for aluminium-zinc coating

Direction	Phase	Elastic Modulus, E (GPa)		Hardness, H (GPa)		Volume Fraction
		Mean	StD	Mean	StD	%
x1	Aluminum	26.96	13.83	1.31	0.25	19
	Zinc	78.26	28.49	1.67	0.84	81
x3	Aluminum	29.51	15.90	0.84	0.52	28
	Zinc	83.25	17.28	1.06	0.33	72
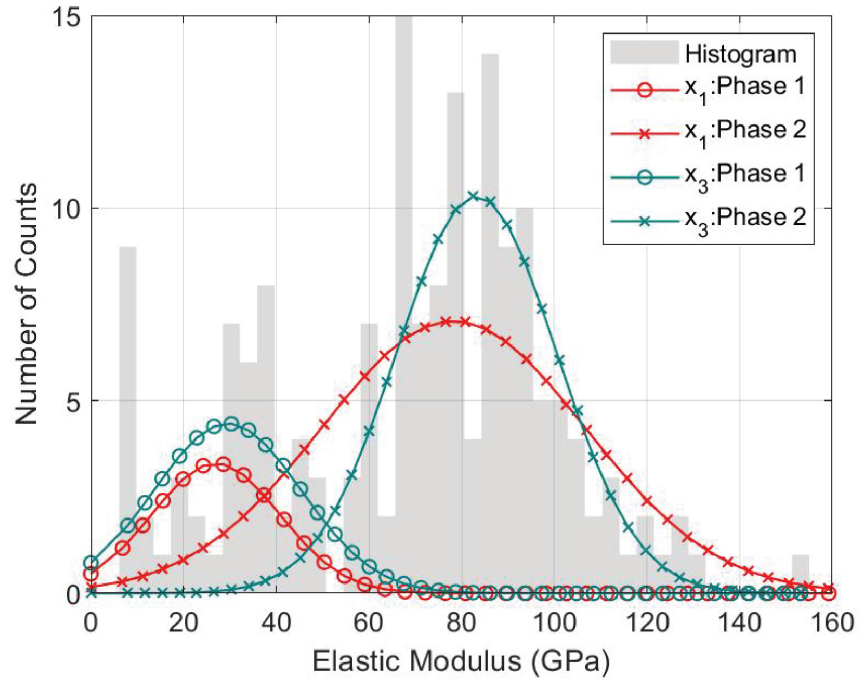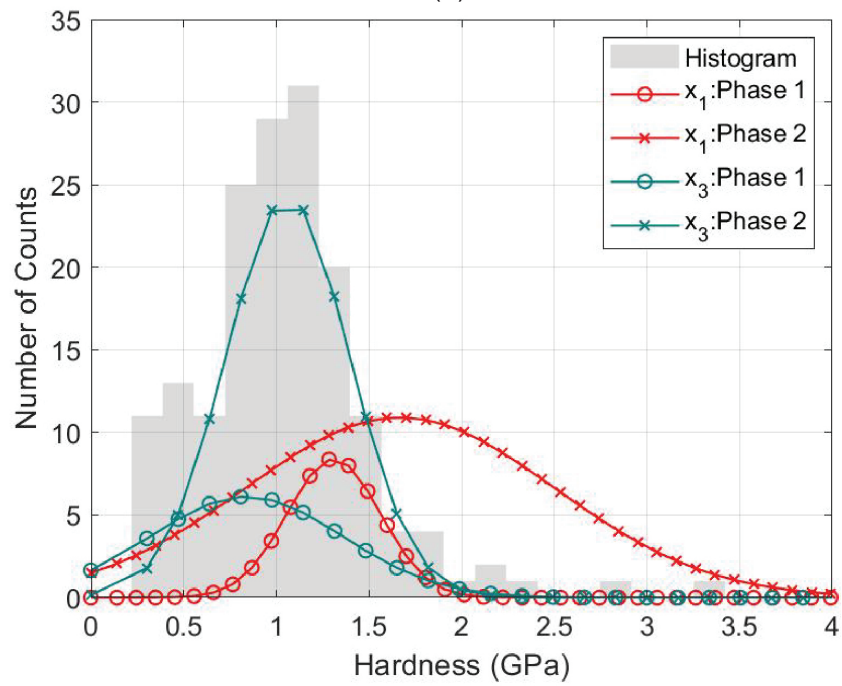
Figure 3.7: Probability distribution function for the Aluminum-Zinc coating (a) Elastic Modulus (b) Hardness
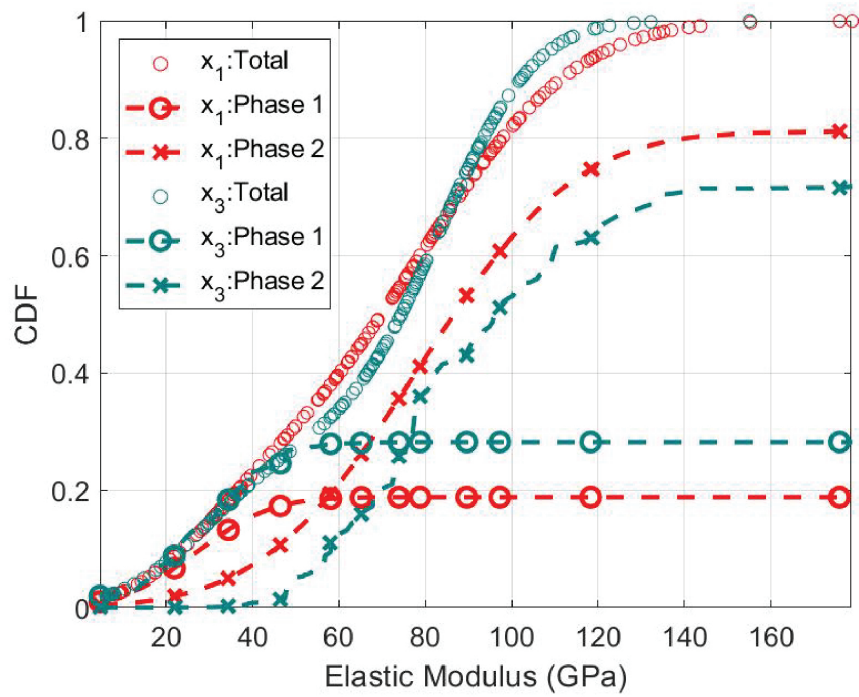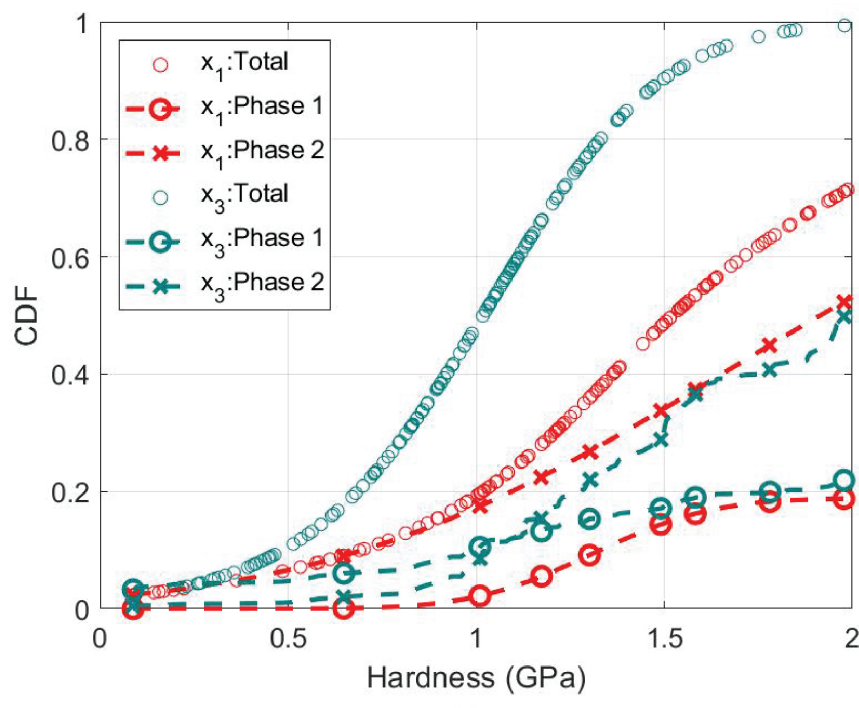
Figure 3.8: Cumulative distribution function for the Aluminum-Zinc coating (a) Elastic Modulus (b) Hardness

3.11　Summary and Conclusion

The grid indentation analysis offers a practical approach to obtain mechanical properties of the individual phases within the thermal sprayed coating. The statistical deconvolution technique is useful in separating the indentation data and allows access into the known phases mechanical properties. As shown in the advanced imaging and microstructure investigation, the thermal sprayed hybrid coating's microstructure is found to be highly complex and heterogeneous. The results obtained using the statistical deconvolution technique shows that the coating's mechanical properties for both the aluminum and zinc content are consistent with the reported literatures, but different compared to the bulk material. What this implies is that the thermal coating's microstructure is fundamentally different compared to the bulk material. Another reason for the difference is due to the fact that nanoindentation measurement is carried out at the microscale, while the bulk material properties is measured at the macroscale. Therefore, it is prudent to identify a link to relate the microscale measurement to the macroscale material properties. The way to achieve this is through the use of multiscaling analysis with experimental data provided at the different length scales. In the subsequent chapter, a computational assisted indentation approach is introduced to enable experimental indentation data to be used in the multiscaling analysis.

Chapter 4

Computational Assisted Indentation Approach

4.1 Introduction

In this chapter, an alternative solution is presented to obtain indentation result by incorporating dimensional analysis, finite element simulation and artificial neural network prediction. The proposed computational assisted indentation approach is not intended to replace the conventional method as described in Chapter 2, but to improve the accuracy by addressing the limitation highlighted previously. The concept of scaling and proportionality is first introduced, followed by the presentation of indentation parameters and their relationship using dimensional analysis. An indentation result database is built to allow for sensitivity study based on a range of mechanical properties specified in the design of engineering (DOE) approach. Finite element simulation is adopted to simulate the indentation process. The final step of the solution is to enable result prediction based on the database by using a custom-built artificial neural network algorithm. In this PhD thesis, a novelty is achieved by incorporating the continuous stiffness method into the indentation proportionality solution. This work has been published in Huen et al. (2020). Graphs and results have been adopted from this publication with the permissions from the authors.

4.2 Dimensional Analysis - Conventional Dimensionless Functions

The central feature of dimensional analysis lies on the fact that physical law does not depend on the arbitrary choice of the units of measurement, but rather dictated by a specific combination of ratios or proportionality in the physical quantities (Cheng and Cheng, 2004). The scaling and proportionality (or similarity) concepts is an essential tool to describe the mechanical behaviour of solid material. Dimensional analysis can be used to describe the relationship of the parameters measured or determined by the nanoindentation mechanism. For example, the indenter shape and size can be related to the indented material's load-carrying capacity. In turn, the load-carrying capacity can be represented by mechanical properties such as hardness

and elastic modulus as a response measured by nanoindentation. The objective here is to use dimensional analysis to describe the strength capacity in terms of nanoindentation response and the mechanical properties, including elastic, plastic, creep and fracture.

The nanoindentation response is conventionally represented by two parameters, i.e. force on the indenter (P) and the displacement of the indenter (h). The CSM method allows dynamic stiffness (S) to be measured throughout the indentation depth. All these measured experimental responses can be replicated in the computational simulation, as explained in the previous section using finite element modelling. Therefore, the simulated response parameters are referred to as the force (F), indentation displacement (h), stiffness (S), work done during loading (W_{tot}) and contact depth (h_c). The material mechanical and geometry properties are chosen as yield strength (Y), elastic modulus (E), Poisson's ration (ν) and the geometrical representation of the indenter (θ).

The dimensional analysis used in this work is made popular by Cheng and Cheng (2004). The approach is represented by dimensionless functions formed based on the relationship in the simulated response with the corresponding mechanical properties and indenter geometry information. The derivation of the dimensionless function starts with the indentation loading process. By combining the material model parameters with the nanoindentation response, the loading curve expression (P_L) can be written as a function of the six established parameters:

$$P_L = f(E, \nu, Y, n, h, \theta) \tag{4.2.1}$$

Among the six established parameters, The parameters E and h are independent dimension. By applying the Π-theorem (Cheng and Cheng, 2004), the loading curve dimensionless function, Π_1 can be obtained. This expression is in line with the relationship found by Tabor (1948) where the load is proportional to the square of the indentation depth. The loading curve coefficient, C is a fitting parameter that is specific to the shape of the loading curve as $F = C_h{}^2$.

$$P_L = Eh^2 \left(\frac{Y}{E}, \nu, n, \theta \right) \qquad or \qquad \frac{P_L}{Eh^2} = \frac{C}{E} = \Pi_1 \left(\frac{Y}{E}, \nu, n, \theta \right) \tag{4.2.2}$$

The unloading process is followed when the loading reaches the maximum indentation depth. Therefore, an additional independent parameter, h_{max}, is added to form the unloading curve expression (P_u).

$$P_u = Eh^2 \left(\frac{Y}{E}, \frac{h}{h_{max}}, \nu, n, \theta \right) \tag{4.2.3}$$

Equation 2.3.2 shows that a power-law function can be used to describe the unloading curve. Similar to the derivation of unloading slope presented in Equation 2.3.3, the unloading stiffness can be derived here by differentiating Equation 4.2.3 with indentation depth (h) and evaluating the indenter displacement at maximum indentation depth (h_{max}). The second dimensionless function representing the slope of the unloading curve can then be obtained.

$$\frac{1}{Eh_{max}} \frac{dP_u}{dh}\bigg|_{h=h_{max}} = \frac{S_u}{Eh_{max}} = \Pi_2 \left(\frac{Y}{E}, \nu, n, \theta\right) \tag{4.2.4}$$

The third dimensionless function involves the contact height (h_c) as an unknown parameter. It has been shown that the contact height (h_c) is dependent on the indentation height (h) with the same four parameters in the loading curve expression, as shown in Equation 4.2.5. By taking $h = h_{max}$ as a specific case, dimensionless function Π_3 shows a converging trend as Y/E increases. This trend is consistent with the conventional Oliver-Pharr method, where the indentation impression has a sink-in profile. However, the data started to scatter when the Y/E ratio is smaller than 0.05 and when the work hardening exponent is relatively large, i.e. $n = 0.5$, indicating a soft material such as metal that exhibits pile-up contact profile.

$$h_c = h\Pi_3 \left(\frac{Y}{E}, \nu, n, \theta\right) \qquad or \qquad \frac{h_c}{h_{max}} = \Pi_3 \left(\frac{Y}{E}, \nu, n, \theta\right) \tag{4.2.5}$$

The fourth dimensionless function representing the indentation work done by finding the area under the loading and unloading curve. By integrating the loading curve from zero to maximum indentation depth (h_{max}), the total work done (W_{tot}) can be derived with the substitution from Equation 4.2.2:

$$W_{tot} = \int_0^{h_{max}} P_L \, dh = \frac{Eh_{max}^3}{3} \Pi_4 \left(\frac{Y}{E}, \nu, n, \theta\right) \tag{4.2.6}$$

Based on a similar approach, the fifth dimensionless function can be derived for the work done during unloading (W_u). By integrating the area under the unloading curve and substituting it with Equation 4.2.3, the unloading work done (W_u) can be derived as

$$W_u = \int_{h_f}^{h_{max}} P_u \, dh = Eh_{max}^3 \Pi_5 \left(\frac{Y}{E}, \nu, n, \theta\right) \tag{4.2.7}$$

As the unloading process consists of elastic rebound, so the work done is reversible (Cheng and Cheng, 2004). Therefore, the irreversible work, i.e. plastic deformation and other energy losses, can be known by subtracting the unloading work done from the total work done. The ratio of irreversible work done to the total work can be shown to form another dimensionless function that is independent of the maximum indentation depth (h_{max}) (Cheng et al., 2002).

$$\frac{W_{tot} - W_u}{W_{tot}} = 1 - 3\,\Pi_6 \left(\frac{Y}{E}, \nu, n, \theta\right) \tag{4.2.8}$$

The hardness (H) can be shown to relate to the same standard dimensionless functions by using the same approach. Note that hardness is related to the force and the contact area. Therefore, the seventh dimensionless function can be derived by adopting the ratio of hardness to the elastic modulus (H/E) and substituting with Equation 4.2.2 and 4.2.5

$$\frac{H}{E} = \frac{P_L}{A_c E} = \frac{P_L}{\pi h_c^2 tan^2\theta E} = \frac{cot^2\theta}{\pi} \Pi_7 \left(\frac{Y}{E}, \nu, n, \theta\right) \tag{4.2.9}$$

4.3 CSM Based Dimensionless Functions

Continuous stiffness measurement (CSM) method allows the stiffness (S) to be determined dynamically along with the indentation force (P) and indentation displacement (h). Recall from Chapter 2 that the indentation force (F) has a linear relationship with the square of the indentation displacement (h^2), the indentation displacement is linearly dependant on the dynamic stiffness (S), and the indentation force is linearly dependant on the square of the dynamic stiffness (S^2). The coefficients for these three relationships are given by the loading gradient (C), displacement-stiffness gradient (C_h) and force-stiffness gradient (C_p) (Wang and Rokhlin, 2005), as shown in Equation 4.3.1. These linear relationships that relate the stiffness with the force and displacements can be observed on a homogeneous and isotropic material. The indentation result using continuous indentation method carried out on fused silica is shown in Figure 4.1.

$$P = C\,h^2 \qquad or \qquad h = C_h\,S \qquad or \qquad P = C_p\,S^2 \qquad (4.3.1)$$

(a)

(b)

(c)
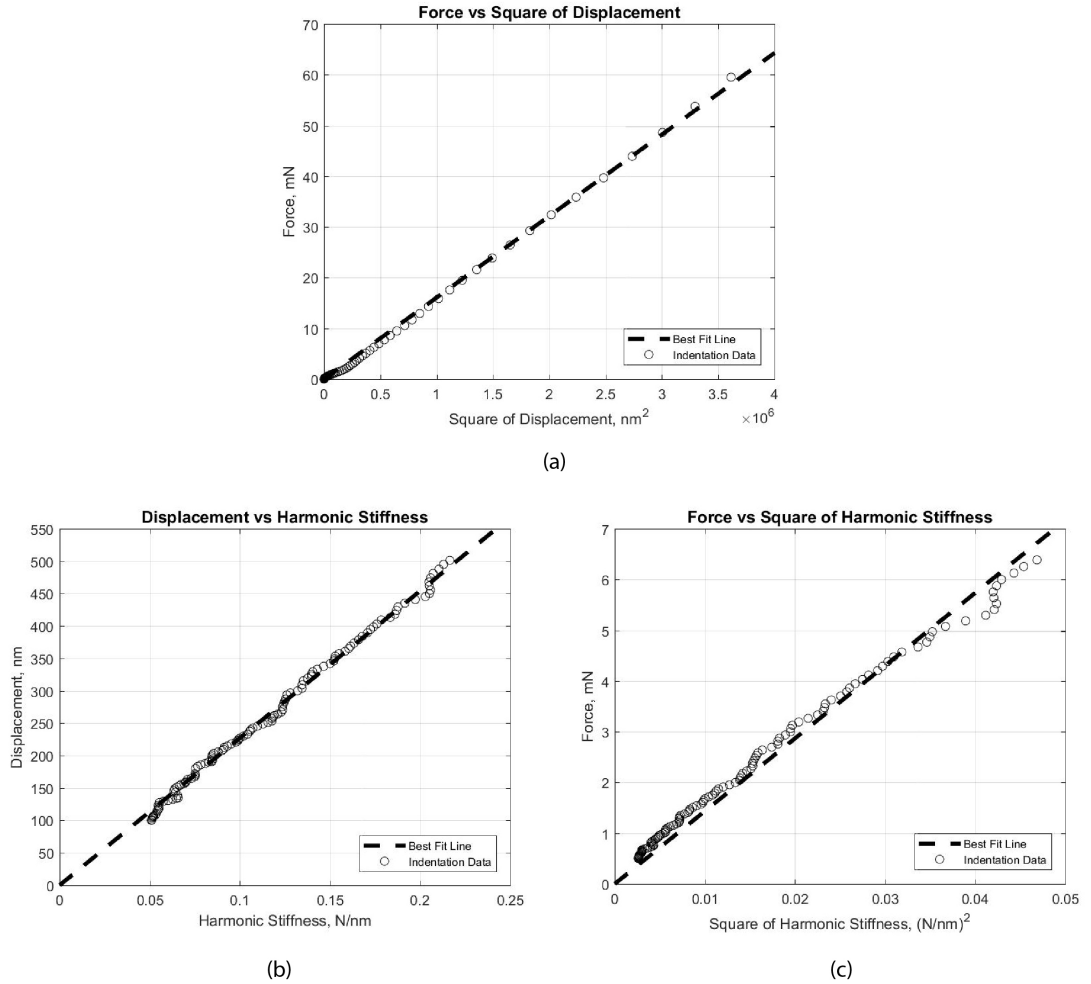
Figure 4.1: Indentation on fused silica a) $F = C\,h^2$, b) $h = C_h\,S$, c) $F = C_f\,S^2$

Experimental indentations were carried out on a hybrid thermal arc sprayed coating with aluminum and zinc, and the outcome is presented in Figure 4.2. For material such as the hybrid coating that does not have homogeneous composition along with the indentation depth, con-

tinuous stiffness measurement can show the presence of multiple phases and the location where the composition change. In this example, the coating shows a change in composition at a depth of 600 nm. The measured stiffness is observed to increase linearly within the same material phase. This observation leads to a constant displacement-stiffness and force stiffness coefficient that can be drawn from the indentation data set.
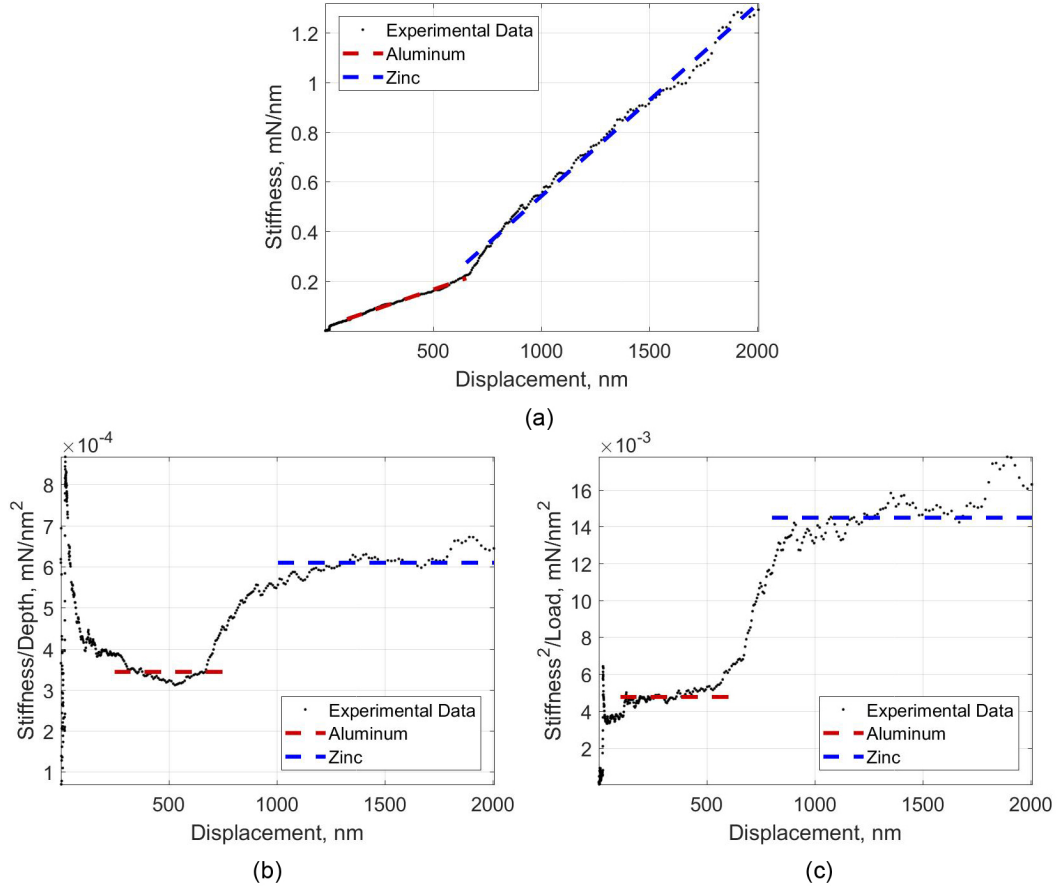
Figure 4.2: Indentation stiffness measurement showing the presence of the aluminum and zinc phases. (a) Stiffness increases linearly with depth (b) Constant displacement-stiffness gradient (c) Constant force-stiffness gradient

Similar to the approach deriving the conventional dimensionless function, these dynamic based stiffness relationship with the indentation force and indentation displacement can be written as the dimensionless function for yield strength (Y), elastic modulus (E), work hardening coefficient (n) and equivalent conical indenter slope (θ). Note that by taking $h = h_{max}$, which is a specific case in the indentation displacement dimension, the dimensionless functions can be written as (Huen et al., 2019):

$$\frac{S}{Eh_{max}} = \frac{1}{EC_h} = \Pi_8\left(\frac{Y}{E}, \nu, n, \theta\right) \tag{4.3.2}$$

$$Y = \frac{S^2}{P} = \frac{1}{C_p} \qquad or \qquad YC_p = \Pi_9\left(\frac{Y}{E}, \nu, n, \theta\right) \tag{4.3.3}$$

4.4   Finite Element Simulation

It is now possible to derive the relationship in nanoindentation response with the material mechanical properties using the dimensionless functions. The presented dimensionless functions contains all the relevant mechanical parameters that can be used to describe the material stress strain relationship. In a typical stress-strain material model, the elastic behaviour that is characterised by Young's modulus (E) and Poisson's ratio (v). The plasticity behaviour is captured after the point of initial yield (Y) by a post yielding stress-strain relationship (ϵ_p is the plastic strain after yield) that follows a power function of work hardening (n).

The purpose of forming the dimensionless functions is to identify the relationship that can be described by a mathematical formulation. Such relationship can only be derived when the indentation response, i.e. P, h and S are known given a specific range of the parameters, i.e. Y/E, ν, n and θ through computational simulation. Computational simulation is carried out with parameter input using the design of engineering (DOE) approach (Sinha et al., 2001) where each parameter is treated as a design level. Each possible combination of individual parameter is systematically inputted into the computational simulation to investigate the simulated indentation outcome. A total of 26 levels with 2496 combinations has been adopted for the simulation as outlined in Appendix A.

A finite model of the indentation process is created using ANSYS Release 18.1 (2019). A two-dimensional axis-symmetric finite element model is used to model the material sample as a homogeneous elastic-plastic solid with a rigid conical indenter of inclined angle (θ) from the vertical centre axis-symmetric axis, see Figure 4.3. A conical indenter is chosen for the fact that it can produce geometrically similar indentation, where the ratio of the indenter's radius to indentation depth is constant. It can be shown that comparable hardness measurement can be obtained for any geometrical similar indenter shape that has an equivalent contact area to the conical indenter (Fischer-Cripps, 2011). When θ is equal to 70.3°, the conical indenter becomes a representation of a Berkovich indenter. The finite element model is built with two dimensional 8 or 6 nodes element (PLANE 83). The sample has a radius and thickness of 50 μm with an element size of 0.1 μm. The choice of selecting 50 μm as the boundary is considered adequate as extent of the stress envelope is expected to be within ten times the indentation depth. During the loading phase, the indenter is driven vertically downward at a displacement of 2 μm, followed by full unloading phase where the indenter retracts back to the initial start position. Friction is considered between the indenter and the sample, which is mainly material-dependent (Yurkov et al., 1997). In this case, the friction is assigned to be 0.15.

The solid has an elastic and plastic stress-strain relationship, as shown in Equation 4.4.1. In the elastic range, the stress and strain are related to the elastic modulus (E). In the plasticity range, after the yield point (Y), the solid material is assumed to yield further with hardening following a multi-linear isotropic hardening model. A non-symmetric solver is adopted on the Newton-Raphson option for the non-linear analysis. True plastic stress and strain are used as input in terms of engineering stress to the finite element model.
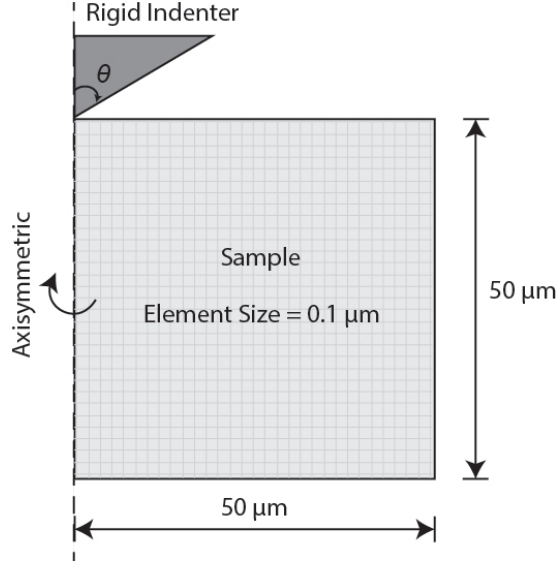
Figure 4.3: Finite element model

$$\sigma = \begin{cases} E\,\epsilon & \text{for } \sigma < Y \\ Y\left(1 + \frac{E}{Y}\,\epsilon_p\right)^n & \text{for } \sigma \geq Y \end{cases} \tag{4.4.1}$$

The computational simulation used in this work has been tailored to replicate the continuous dynamic continuous stiffness measured found in the CSM method in a simplified manner. The stiffness measurement is a result of the registered force at a corresponding depth, i.e. $S = P/h$. A simulated loading process is divided into multiple intervals to replicate the continuity of the stiffness measurement. Along with each interval during the loading process, a relatively small static displacement of 1 nm is incorporated while the corresponding forces are retrieved in the simulation. This simplification method of using static stiffness in place of the dynamic stiffness measured by CSM has been proven to be identical when the dynamic oscillation is at 45 Hz (Wang and Rokhlin, 2005). Based on this simplification, the stiffness can then be measured in the simulation by dividing the force changes during each interval with the small static displacement, i.e. $S = dF/dh$ where dF is the force difference at each interval and dh is 1 nm. This simplified static stiffness can be treated as the onset of an elastic rebound due to the relatively small displacement imposed during the interval. For this reason, the unloading stiffness relationship with the elastic modulus derived by the Oliver-Pharr method can be used with the simulated static stiffness.

4.5 Macrotesting Verification

Macro tensile tests and actual nanoindentation are carried out to compare the actual physical result with the simulated result to verify the accuracy of this finite element model. Two reference materials, i.e. bulk aluminum and steel, are tested in the form of a 12 mm cylindrical bar, according to ASTM et al. (2001). The result of this verification is shown in Figure 4.4. The actual stress-strain result from the tensile tests are inputted into the indentation simulation, and the outcome is compared to actual nanoindentation experimental result. The simulation response is observed to be very close to the actual nanoindentation test response. The discrep-

ancy noted may be due to surface roughness resulted in non-ideal contact interface (Jiang et al., 2008).
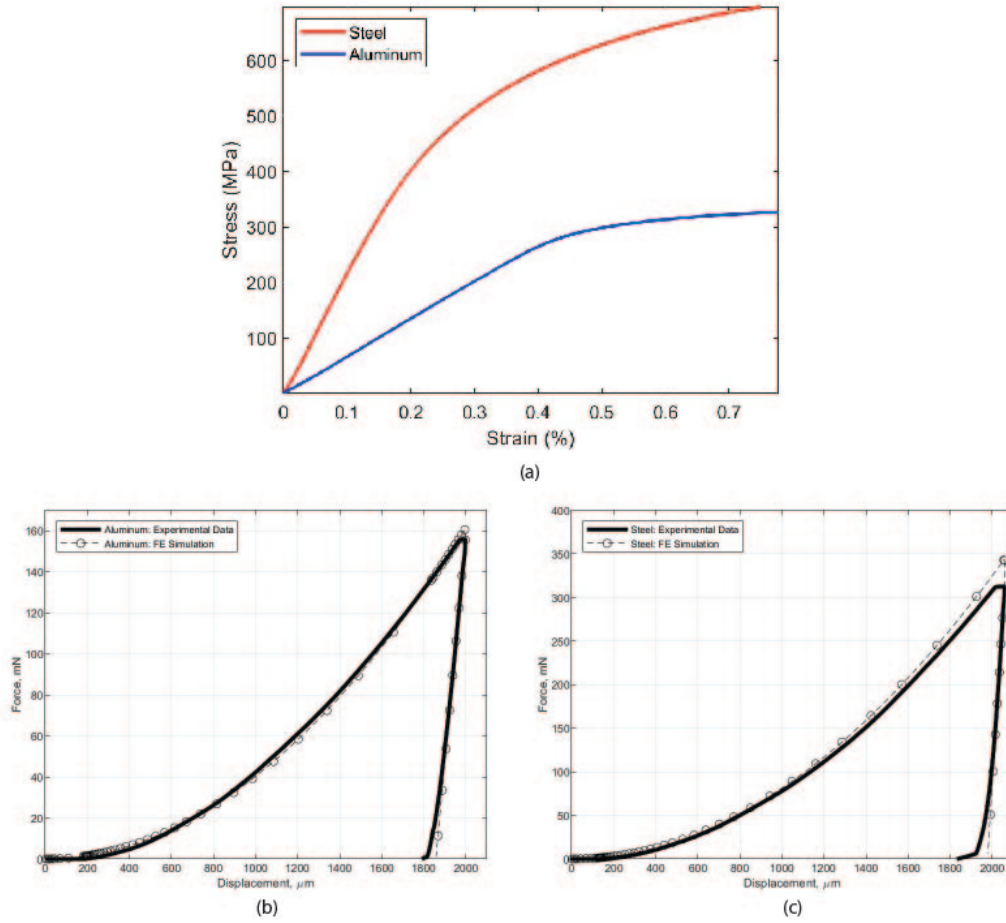
Figure 4.4: Macro tensile test and nanoindentation experiment result (a) tensile test (engineering) stress-strain result (b) nanoindentation response on aluminum (c) nanoindentation response on steel

4.6   Artificial Neural Network

Artificial neural network (ANN) tool by Matlab (Release 2019a) is used to derive the relationship for all the proposed dimensionless functions used in this work. The neural network is a form of machine learning to learn the relationship from data by utilising multiple layered inputs, hidden and output structures. The application of artificial neural network has been accepted with a high level of accuracy to predict a sizable number of outcomes from nanoindentation based on a large volume of data (Haj-Ali et al., 2008). ANN uses a series of computational cells (neurons) that are interconnected with different adjusted weights. The forward-pass network consists of multiple layers with several cells where the first layer is the input, and the last layer is the output. All the layers and their cells in between are referred to as a hidden layer. The ANN learning algorithm can adjust the optimisation variables, i.e. weights, between each cell connection to minimise the cumulative error in the objective function. The quality of the learning outcome is therefore measured by the amount of error between the input and the predicted value. The process of using ANN to predict the unknown parameters is described in the following steps:

1. Data identification: Five unknowns have been shown in the dimensional analysis, i.e. Y, E, ν, n and θ. Five dimensionless functions have been chosen as input data to solve these unknowns. Additional dimensional functions can be added to improve the accuracy of the ANN result. However, it has been demonstrated the ANN prediction accuracy is sufficiently high that with only five dimensionless functions. These dimensionless functions are selected because they can represent the overall indentation response and provide an essential relationship between measured parameters, which are force, displacement and stiffness, to the unknown mechanical and contact parameters. Pre-processing is required to derive the simulated response parameters in each dimensionless function using the outcome from the simulation.

2. Data training: After all the data in the whole DOE combination cases are ready, training can then be initiated. Only 70% of the chosen data point will be used for the training. This work employs the Bayesian regularisation training algorithm for the training as it is known to improve the performance of the ANN target identification. Thirty hidden layers chosen to be tangent sigmoid has been used in the optimal network configuration. This choice of hidden layers is justified by the outcome from a mean square error convergence, as shown in Figure 4.5. The number of hidden layers used is considered adequate for the size of the input data with the entire 2496 parameters combination. The outcome of the ANN result is expressed in a matrix form, as shown.

3. Data validation: Another 15% of the data points are used to evaluate network performance. The acceptance limit is given on each training procedure to achieve an acceptable diagnostic performance from ANN, with 1000 iterations for a change in gradient of 1.00e-7 and a standard deviation of 0.005. Based on these diagnostic parameters, the quality of prediction is presented in terms of an R2 coefficient that is similar to the root mean square (RMSE) by comparing the predicted values with the input value. The outcome shows that the expected result achieves high accuracy in line with accuracy imposed by the target acceptance limit, see Figure 4.6.

4. Data prediction: The remaining 15% of the data are used to provide the simulation and projection as the ANN outcome.
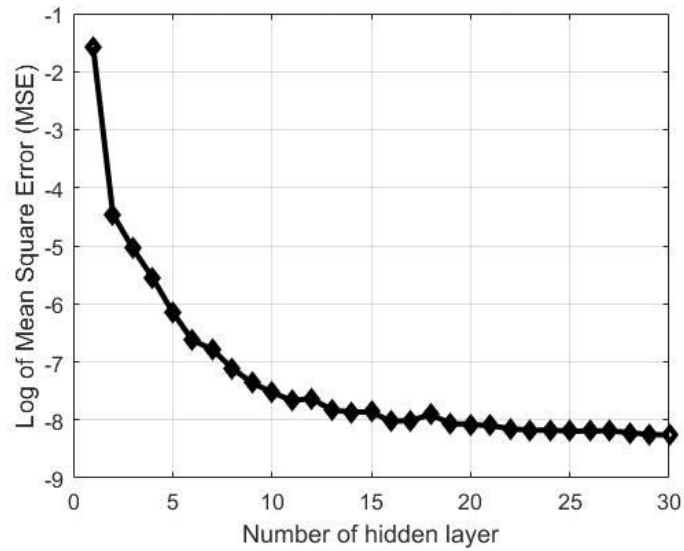
Figure 4.5: Mean square error result showing convergence with the increasing hidden layer used
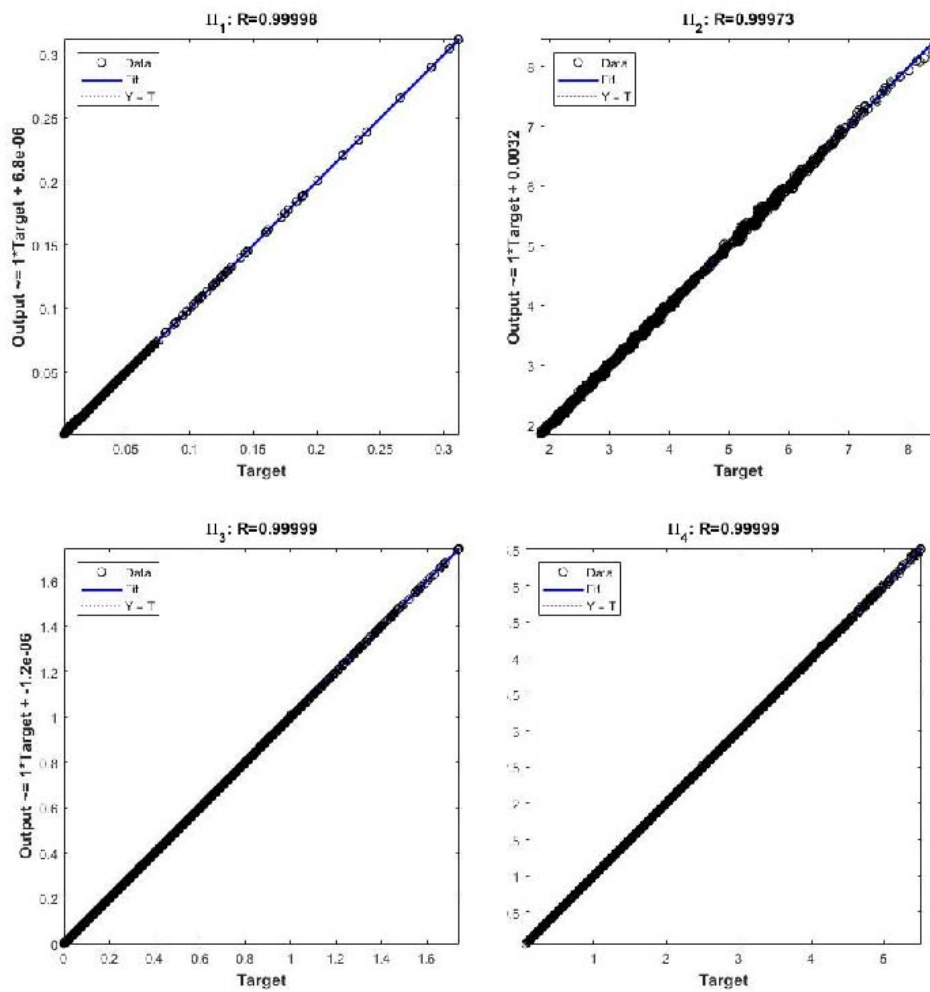
Figure 4.6: Quality of prediction by performed by ANN for the dimensionless functions

4.7   Stiffness Based Inverse Algorithm

It is learned from Chapter 2 that the indentation contact area (A_c) remains difficult to derive because the indentation impression cannot be measured during the indentation process. Furthermore, the current conventional approach using the Oliver-Pharr method is limited to only the sink-in profile. It is also apparent that the mechanical properties calculated by Oliver-Pharr method rely on the indentation force, displacement and unloading stiffness. While the first two parameters can be measured, the unloading stiffness can only be in-directly derived based on the experimental power-law relationship (Equation 2.3.2). Hence, a more accurate indentation stiffness derivation is required to improve on this matter. For this reason, this PhD work adopts the continuous stiffness measurement (CSM) method that allows indentation stiffness to be measured dynamically during the indentation process. Understanding the relationship and proportionality of stiffness with the indentation measured mechanical properties is the essence of this part of PhD thesis. While the relationship of indentation stiffness with the force and displacement has been previously established (Wang and Rokhlin, 2005, Wang et al., 2005), this research further expands this concept with an aim to rigorously study the relationship and proportionality of indentation stiffness with other indentation parameters. The outcome of this work enables predicting indentation results with a relatively better accuracy based on indentation stiffness. This work has been published in Huen et al. (2020).

A reverse algorithm has been introduced to enable the indentation result prediction based on the measured stiffness. The purpose of this algorithm is to enable a relatively quick assessment of the indented material elastic modulus and hardness based on the indentation stiffness measurement. Recall from Equation 4.3.1, the indentation stiffness is related to the indentation force and displacement. The respective displacement-stiffness coefficient (C_h) (Equation 4.3.1) from the indentation experiment is required by plotting the indentation depth (h) against the measured stiffness (S).

This algorithm has two new dimensionless functions based on the stiffness measured by the CSM method that is proportionate to the material mechanical properties, similar to those presented in Equation 4.3.2 and 4.3.3. The first new dimensional function is introduced by combining the dimensionless functions in Equations 4.2.1 and 4.3.2 as:

$$C\,C_h = \Pi_{10}\left(\frac{Y}{E}, \nu, n, \theta\right) \tag{4.7.1}$$

Since both the dimensionless functions Π_1 and Π_{10} have the same dependable parameters, these two functions can be related to each other directly and form a new dimensionless function as shown in Equation 4.7.2. For the case of $\theta = 70.3°$, which is the equivalent conical indenter for a Berkovich indenter, this relationship is plotted in Figure 4.7 by varying the Poisson's ratio (ν). Choosing this pair of dimensionless function is the first step in the algorithm where the elastic modulus (E) can be determined from two known responses obtained during the indentation process, which are the loading gradient (C) and the displacement-stiffness gradient (C_h), as:

$$\frac{C}{E} = f\left(C_h\,C\right) = \left(7.65\nu^2 - 2.266\nu + 3.747\right)\left(C_h\,C\right)^{0.7314} \tag{4.7.2}$$

36
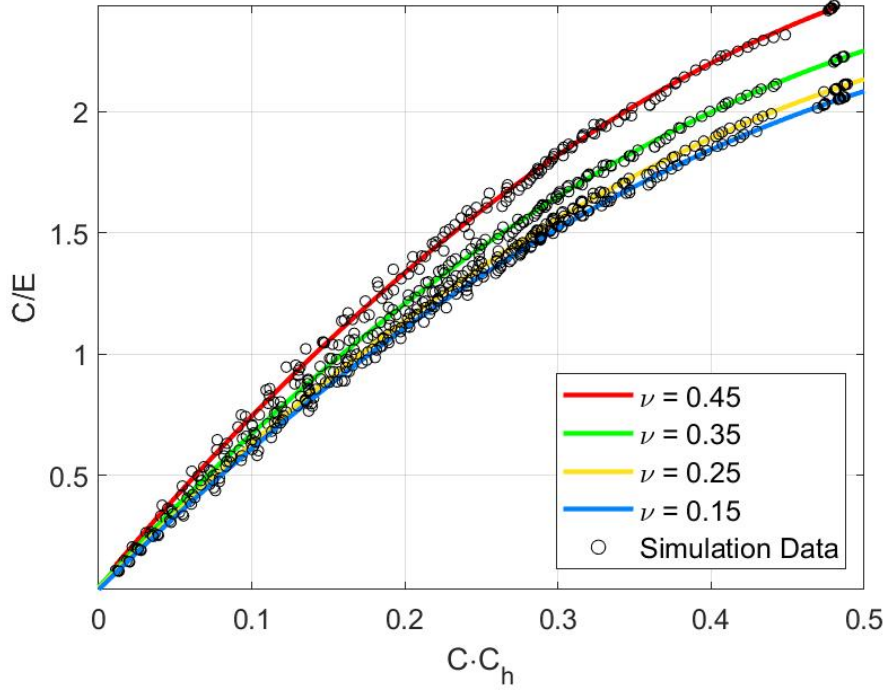
Figure 4.7: Dimensionless Relationship between C/E and $C\,C_h$ for $\theta = 70.3°$

After the elastic modulus is made known based on the relationship in Equation 4.7.2, the next parameter to be determined is the contact depth (h_c). Conventionally, the contact depth can be derived based on an area function (Equation 2.3.7). However, this area function is not suitable to represent a pile-up profile. The dimensionless function for contact depth (Π_3) is adopted to address this issue. The second new dimensionless function is then introduced by combining Equation 4.4 and 4.3.2 to form Equation 4.7.3 that relate relating the elastic modulus (E) to the contact depth (h_c) and maximum indentation depth (h_{max}). For the case of $\theta = 70.3°$, this relationship is plotted in Figure 4.8 by varying the Poisson's ratio (ν).

$$\frac{h_c}{h_{max}} = f\left(E\,C_h\right) = \left(-0.24\nu^2 - 0.064\nu + 0.172\right)\left(E\,C_h\right)^{-0.9323} \tag{4.7.3}$$

Once the contact depth (h_c) is determined from Equation 4.7.3, the contact area can be determined with Equation 4.7.4, and the hardness can be subsequently derived by using the Equation 4.7.5.

$$A_c = \pi a^2 = \pi h_c{}^2 tan^2\theta \tag{4.7.4}$$

$$H = \frac{P_{max}}{A_c} \tag{4.7.5}$$
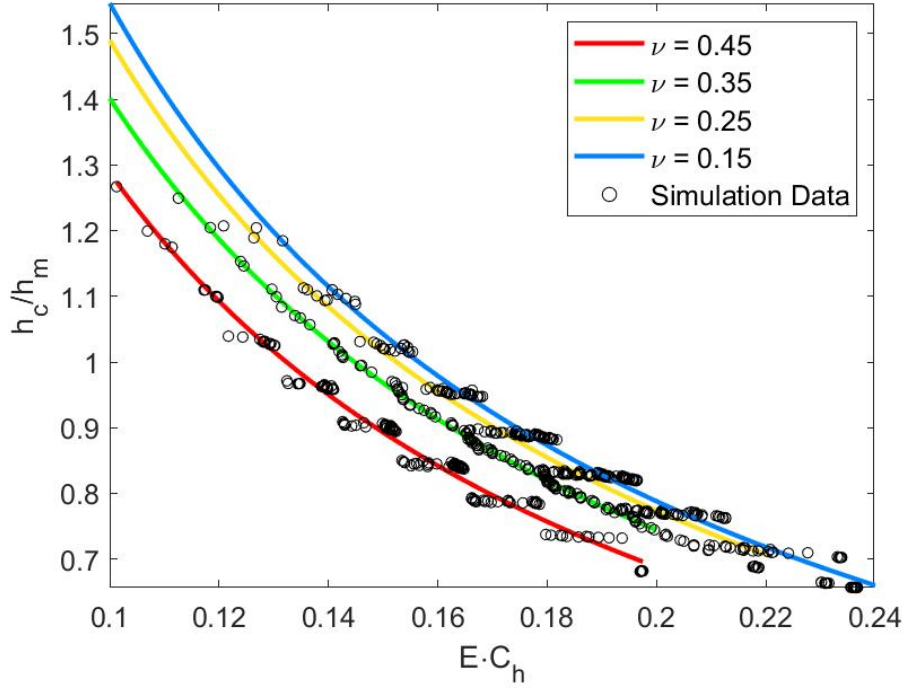
Figure 4.8: Dimensionless Relationship between h_c/h_{max} and ECh for $\theta = 70.3°$

4.7.1 Verification

The contact area determined by the proposed stiffness based algorithm is verified against two conventional methods, i.e. Cheng and Cheng method (Cheng and Cheng, 1998) and Oliver-Pharr Method (Oliver and Pharr, 1992). The Cheng and Cheng method proposed a proportional relationship for the contact depth with the maximum indentation depth using the Equation 4.7.6, where the elastic modulus (E) is a pre-requisite parameter.

$$\frac{1 - \nu^2}{E\, h_c\, tan\theta}\, S|_{h=h_m} = 2 \tag{4.7.6}$$

The Oliver-Pharr method suggested that the contact area can be determined using Equation 4.7.7, which is derived based on the unloading stiffness relationship with the elastic modulus (see Chapter 2 Equation 2.3.4). The geometry correction factor ϵ is taken as 0.75 (Oliver and Pharr, 1992) based on a sink-in profile.

$$h_c = h_{max} - \epsilon\, \frac{P_{max}}{S|_{h=h_m}} \tag{4.7.7}$$

The outcome of the comparison between the proposed stiffness based reverse algorithm with the Cheng and Cheng method and the Oliver-Pharr method is presented in Table 4.1. Three materials have been used for this comparison, namely bulk aluminum, bulk steel and fused silica. It is known that both the aluminum and zinc exhibits a pile-up profile while fused silica exhibits a sink-in profile (Oliver and Pharr, 2004). The result from this comparison is consistent with the observation made by Cheng and Cheng 2004 for both the pile-up profile ($h_c/h_{max} > 1$)

and sink-in profile ($h_c/h_{max} < 1$). In other words, the proposed reverse algorithm from this work is capable of differentiating the correct indentation profile for any indentation process within the investigated material range.

Table 4.1: Contact depth h_c/h_{max} comparison

Materials	This Work (Eq. 4.2)	Cheng and Cheng Method (Eq. 4.7.6)	Oliver-Pharr Method (Eq. 4.7.7)
Bulk Aluminum	1.002	1.127	0.944
Bulk Steel	1.083	1.438	0.974
Fused Silica	0.732	0.772	0.690

From Table 4.1, it is observed that the Cheng and Cheng method consistently return with higher value when compared to the reverse algorithm from this work. Figure 4.9 is plotted with the left-hand side of Equation 4.7.6 against σ_y/E using the simulation data points to explain the reason behind this observation. It is observed that the plots with varying θ of 65° to 80° have a relatively large variation in the range of $0 < \sigma_y/E \leq 0.04$ and converging to a constant in the range of $0.04 < \sigma_y/E \leq 0.5$. The mean value of each case (plotted as dotted line in Figure 4.9) is 2.099, 2.161, 2.240, 2.390 when θ is 65°, 70.3°, 75° and 80° respectively. In this figure, the σ_y/E values in the horizontal axis are for the data between $0 - 0.1$ to highlight the significant discrepancy of S/Eh when the σ_y/E ratio is up to 0.06. Since the contact depth (h_c) is inversely proportional to this mean value, this explains why the Cheng and Cheng method has a higher estimation of the contact depth by assuming the mean value as 2. The situation is amplified when the material has a low σ_y/E such as the metal, i.e. bulk aluminum and steel. The over-estimation of the contact depth by the Cheng and Cheng method can be higher because the true value of $S(1 - \nu^2)/(Eh_c tan\theta)$ tends to go higher than the determined mean value. For the case of an equivalent cone angle $\theta = 70.3$°, the estimated true value is 12% higher than the values derived using the Cheng and Cheng method. On this account, the proposed reverse algorithm in this work is considered consistent with the value derived from the Cheng and Cheng method.

4.7.2 Outcome

The proposed algorithm is summarised in a flowchart presented in Figure 4.10. A comparison is made to compare the outcome using the proposed inverse algorithm with the conventional methods including the power-law method proposed by Oliver and Pharr (Oliver and Pharr, 1992, 2004) and the Dao's method (Dao et al., 2001) that based on dimensional analysis. Indentations are carried out on bulk aluminum and the outcome is presented in Table 4.2. Since the elastic modulus and hardness result are closely related to the contact depth, the predicted outcome for these properties is similar to the previous result, where the proposed inverse algorithm predicted value lies in between the Oliver and Pharr method and the Dao's method. This outcome agrees well with previous literature (Bolshakov and Pharr, 1998, Bolshakov et al., 1996) where the Oliver-Pharr method is found to underestimate the contact depth while overestimating both the elastic modulus and hardness.

Table 4.2: Contact height h_C/h_m ratio comparison with the conventional methods

Indentation Solution	Elastic Modulus, E (GPa)	Hardness, H (GPa)
Stiffness based explicit solution (this work)	87.4 ± 5.9	0.19 ± 0.019
Oliver and Pharr Method	110.3 ± 6.1	0.21 ± 0.017
Dao's reverse analysis algorithm	62.1 ± 10.7	0.07 ± 0.021
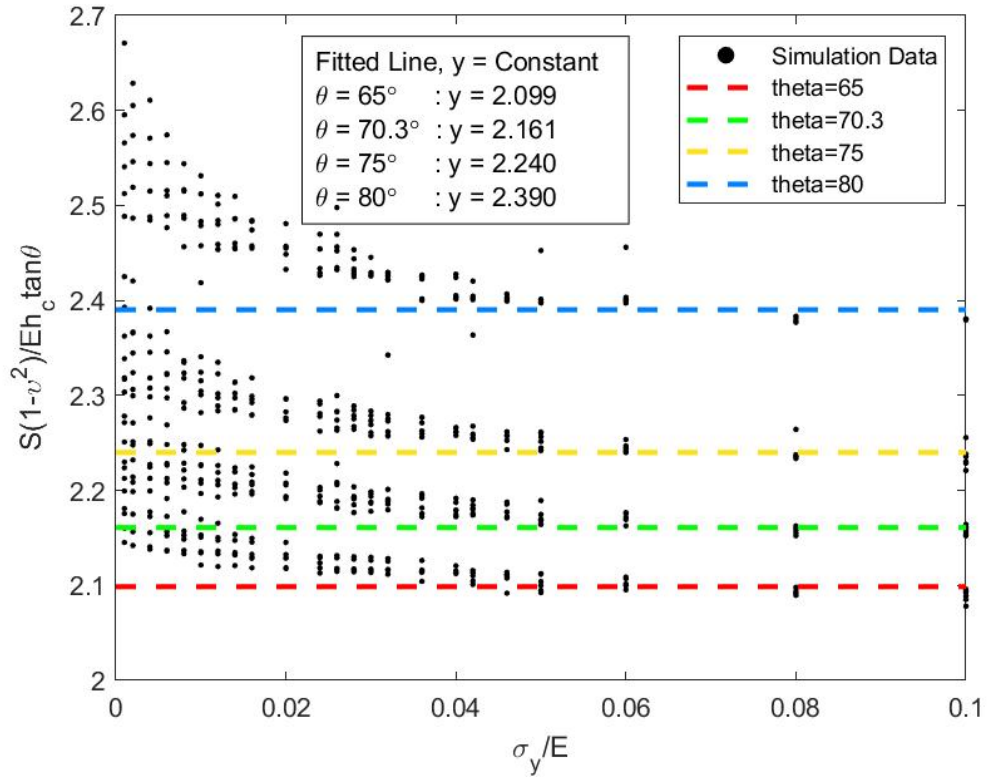
Figure 4.9: Relationship between $S(1 - \nu^2)/(Eh_c tan\theta)$ and σ_y/E

This algorithm can accurately estimate the elastic modulus and contact depth based on the measured indentation stiffness. The accuracy of this algorithm has been demonstrated by comparing the indentation carried out on three different materials, which are the bulk aluminum, bulk steel and fused silica, to the established conventional methods. The proposed algorithm is capable of differentiating the sink-in and pile-up profile contact depth within these three materials. The proposed graph fitting function in the reverse algorithm can be applied relatively quickly and accurately if the material Poisson's ratio is known, and the indentation is carried out with an ideal Berkovich indenter ($\theta = 70.3°$). However, in practice, the true Poisson's ratio of the material remains unknown and the Berkovich indenter may be far from ideal due to wear and tear, although the assumptions in these parameters do provide a close enough solution to the true value.

It should be noted that similar methodologies by Dao et al. (2001), Ma et al. (2012a) and Ogasawara et al. (2006) that depend on curve fitting to identify the mechanical properties solution by nanoindentation has been well established. However, previous literatures results are based on a fixed Poisson's ratio and a perfect Berkovich tip that has an equivalent conical angle of 70.3°. These assumptions are likely to introduce error into the estimation of the contact area estimation. Assuming Poisson's ratio of 0.3 may be reasonable for metal which has been reported to have a limited range between 0.25 - 0.35 (Ma et al., 2012b), this assumption may not be applicable for other types of material. The indenter's contact condition due to surface roughness and indenter tip radius are known factors that significantly affect the mechanical properties measurement result by nanoindentation (Shibutani and Koyama, 2004). Previous research showed that the effect from the indenter contact condition could be represented by altering the equivalent conical angle that will result in changing the loading curve response shape
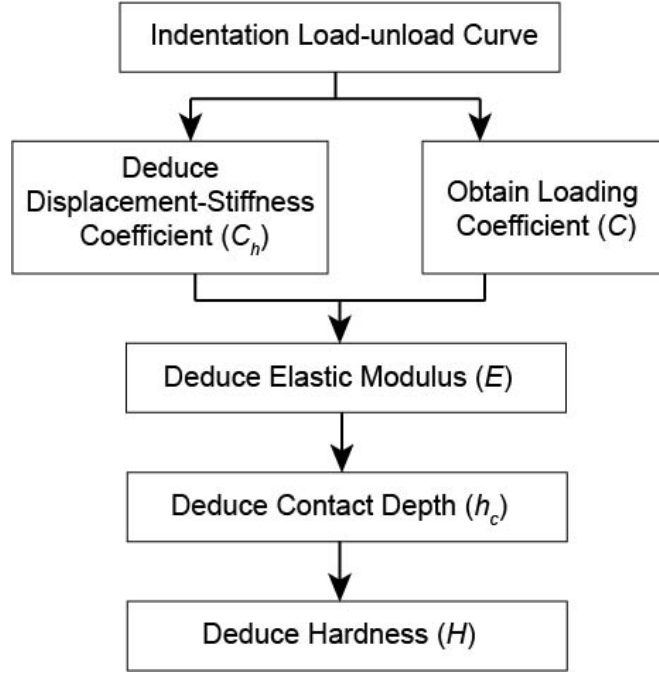
Figure 4.10: Reverse algorithm to determine the contact area and hardness using stiffness based dimensionless functions

(Kim et al., 2007). Therefore in an actual nanoindentation test, perfect indenter with ideal contact condition is not possible due to the surface roughness and tip imperfection, resulting in an alteration in the equivalent conical angle. For this reason, the assumption of a constant equivalent conical angle is likely to introduce error when trying to match the actual indentation response. Considering the limitation poised by the curve fitting method, the next section will present an improvement by adopting the artificial neural network to predict the nanoindentation outcomes by varying all the elastic and plastic parameters.

4.8   Machine Learning Solution

The curve fitting method and the previously introduced inverse algorithm depends on a prerequisite Poisson's ratio and an equivalent conical angle. These assumptions may introduce a small amount of error in the estimation of the indentation result. For this reasons, it is prudent to introduce the machine learning approach using the artificial neural network (ANN) to predict the indentation result without the needs of having assumed parameters.

The machine learning approach relies on the same indentation simulation database built by running indentation simulation on 2496 combination outlined in the design of experiment (Appendix A) with the finite element model detailed in the previous section. Machine learning or training is then implemented using the artificial neural network tool by Matlab to find out the relationship among the five selected dimensional functions, i.e. Π_1, Π_3, Π_4, Π_8 and Π_9. The details of the training are explained in the *Artificial Neural Network* section. Previously in the inverse algorithm, only the elastic modulus and hardness are determined. Further mechanical properties, including the yield strength and work hardening, are added using the machine learning approach. The addition of these parameters adds to the complexity of the interrelationship from the dimensional functions, where conventional curve fittings are deemed difficult if not

possible. The derived dimensionless functions show that the relationship with yield and work hardening is non-linear with no obvious trend with the other mechanical parameters. The use of stiffness based criteria remains valid for the entire range of σ_y/E where the displacement-stiffness and force-stiffness gradient is always constant. The outcome of the stiffness-based plot is shown in Figure 4.12.
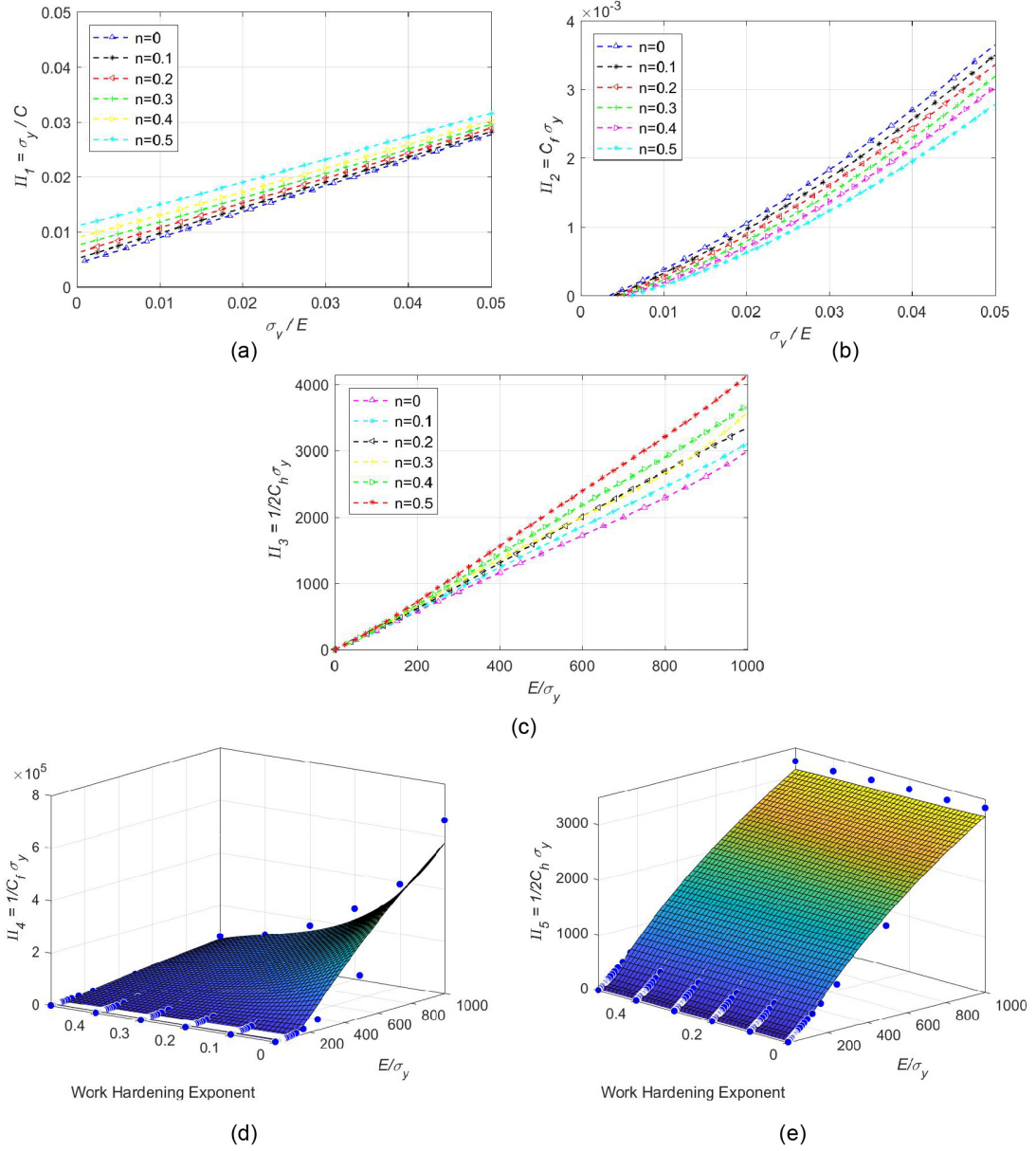
Figure 4.11: Dimensional functions plot with ν=0.25, $\theta = 70.3°$ with varying work hardening exponent

Once the training is complete, the machine learning approach can be used to replicate the load-unload curve. The prediction procedure starts by choosing a specific indention location. Based on the experimental indentation result, the loading coefficient (C from Equation 4.2.2), the stiffness based coefficient (C_h and C_f from Equation 4.9) and the total indentation energy (W_{tot} from the area under the experimental load-unload curve). Using non-linear solver tool from Matlab, these three parameters are inputted into the trained neural network database to extract all the corresponding dimensional function parameters, including Y/E, E, Y, ν, n, θ and h_c. The force and displacement scatter can then be replicated using the relationship
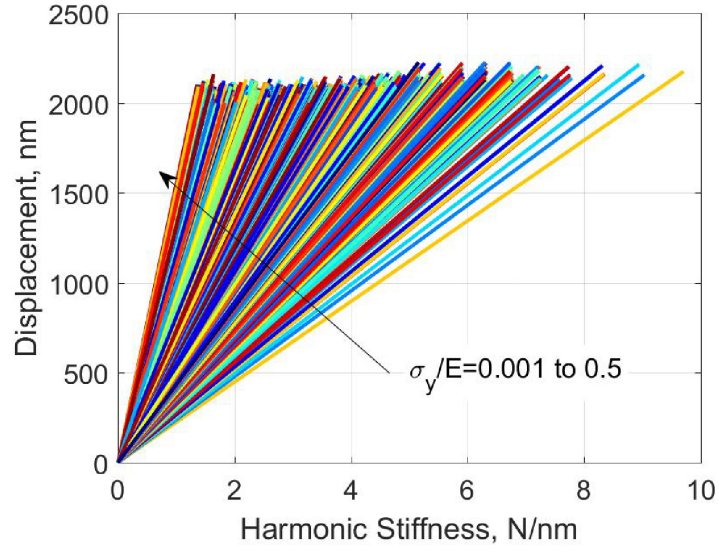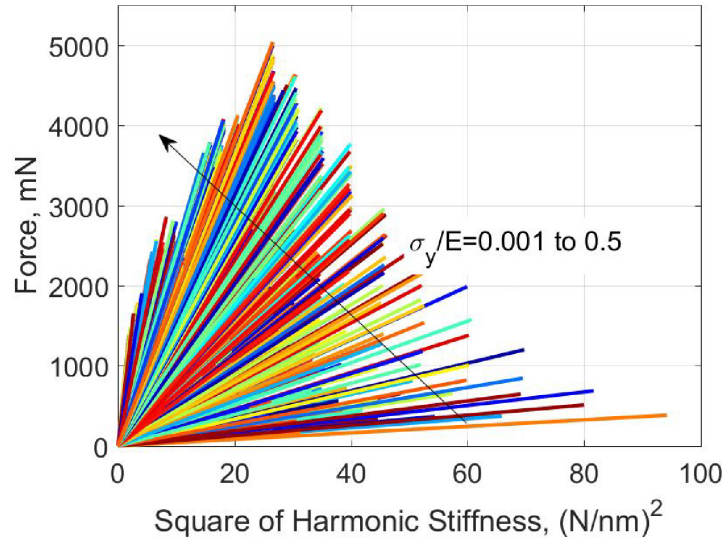
Figure 4.12: Stiffness based coefficient simulated outcome for the entire range of σ_y/E

outlined in the dimensional functions. The load-unload curve derived from the ANN prediction is presented in Figure 4.13. It is observed that the predicted load-unload data points are very close to the experimental load-unload curve.

4.8.1   Result and Discussion

By setting the ANN derived result as the mean value, a statistical deconvolution procedure is carried out to determine the standard deviation spread and the volume fraction for each of the material's phases, which is the aluminum and zinc. The outcome is compiled in table 4.3. The value obtained suggests that the properties of the coating materials are similar to those of the bulk materials. The aluminum elastic modulus has a range of $47 - 90$ GPa (Chen et al., 2005, Dai, 2003, Huang and Spaepen, 2000, Saha and Nix, 2002, Van Steenkiste et al., 2002) and the zinc has a range of $62 - 75$ GPa (Guzman et al., 2000, Sundararajan et al., 2013). The hardness derived by the ANN for both phases are found to fall within the range of reported bulk material
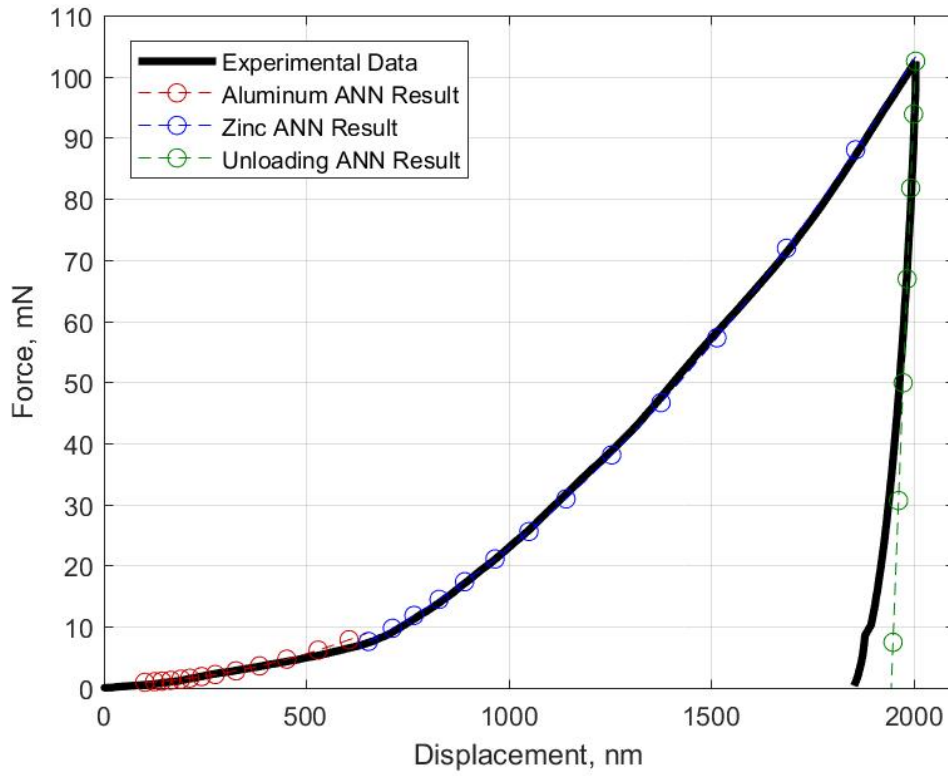
Figure 4.13: ANN load-displacement curve plot compared to multi-phase indentation experimental data for a random indentation location

hardness range, where aluminum has a range of 0.7 – 1.0 GPa (Kang et al., 2014) and zinc has a range of 0.45 – 1.86 GPa (Jiang et al., 2008). With both the elasticity (E) and plasticity (Y, n) parameters determined, the stress-strain curve can be plotted, and the outcome is presented in Figure 4.14.

Table 4.3: Aluminium and Zinc phase properties in arc thermal spray aluminium and zinc coating

Phase	Elastic Modulus, E (GPa)		Hardness, H (GPa)		Yield Strength, σ_y (GPa)		Work Hardening, n (GPa)		Volume Fraction
	Mean	StD	Mean	StD	Mean	StD	Mean	StD	%
Aluminum	57	33	0.92	0.35	157	17	0.17	0.02	68
Zinc	78	12	1.63	0.64	212	71	0.21	0.06	38
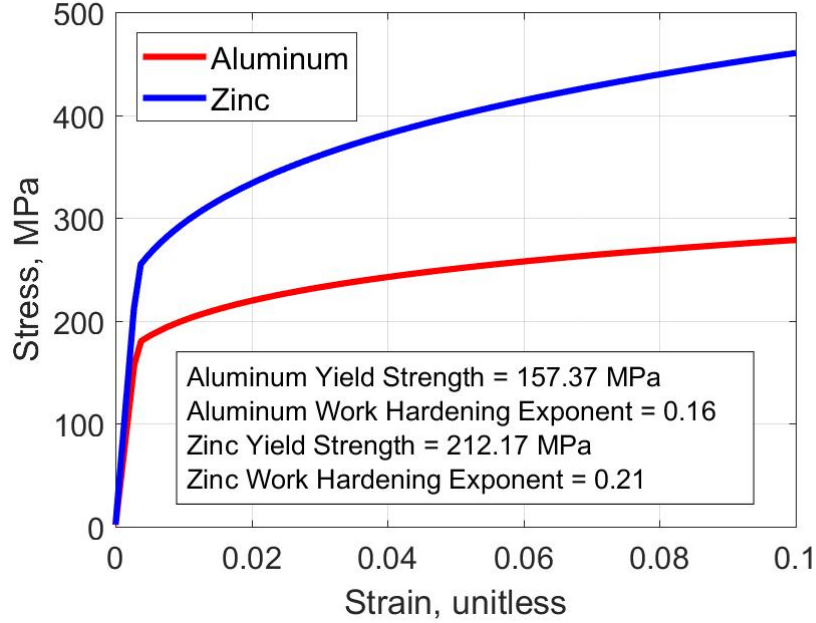
Figure 4.14: Stress strain curve plot for aluminum and zinc phase within the coating based on ANN result

4.9 Summary and Conclusion

The mechanical properties of multiphase coating have been determined at the microscale level using a combination of nanoindentation, numerical simulation and dimensional analysis. Using the continuous stiffness method from the nanoindentation investigation technique with the simulated-proportional indentation approach is the novelty presented in this work. The introduction of the stiffness parameters as a measured value rather than theoretical derived result provides greater access into the true material mechanical behaviour. This work shows that the new approach allows improvement made on the conventional method of interpreting nanoindentation experimental investigation by addressing the challenge in determining the indentation contact area and differentiate the sink-in and pile-up indentation profile. Through the use of dimensional analysis approach, the effects of variation in the engineering and indentation geometry parameters can be incorporated into the solution hence allowing better accuracy and consistency in the indentation outcome.

The proposed simulated-proportional indentation approach is presented in two distinct solutions. The first is a simplified solution using an inverse algorithm, and the second solution relies on machine learning. The inverse algorithm is similar to the conventional approach, where a curve-fit dimensional function solution is presented that is based on the measured stiffness parameter. This simplified solution requires the Poisson's ratio and the equivalent indentation cone angle to be known as a prerequisite, which is commonly adopted from practical engineering judgement. The second solution presents a more intricate approach by utilising machine learning to obtain the desired mechanical properties. Based on the same simulation database, machine learning is implemented to acquire a trained relationship of all the mechanical properties specified in the desired dimensional functions. Based on the results, the desired elastic and plastic mechanical properties are matched with the input experimental measured outcome using a customised post-processing algorithm based on the non-linear solver by Matlab.

Chapter 4 concludes by presenting the outcome and conclusion from the computational assisted indentation approach, as tabulated in the following:

1. The proposed stiffness based inverse algorithm can be used to derive elastic modulus and hardness based on the measured indentation stiffness. This algorithm can differentiate both the sink-in and pile-up indentation profile and remain valid for the entire range of $0 < \sigma_y/E \leq 0.5$.

2. The machine learning solution enables the prediction of the indented material mechanical elastic and plastic parameters based on the measured indentation experimental load-unload response. The machine learning is considered an improvement to the simplified inverse algorithm as it does not require pre-requisite engineering parameters to be known. The artificial neural network training result and the prediction made using the nonlinear solver tool by Matlab are found to match more than 99% of the simulated indentation outcome.

3. The continuous stiffness method (CSM) can be used to differentiate the presence of individual phases in the hybrid thermal sprayed aluminum and zinc. The change in stiffness gradients for the indentation force and displacement can be used to identify the transition from one phase to another. These stiffness gradients are unique for the specific material. Hence, this feature allows the material properties along the indentation depth to be investigated. The elastic modulus and hardness determined for the aluminum and zinc coating is found to be lower than the equivalent bulk material properties.

In the next two chapters, a multiscaling approached will be presented to describe a material system consisting of multiple scale lengths. The material system is represented by the thermal sprayed aluminum and zinc coating as the application. Nanoindentation is carried out on the thermal sprayed coating. The downscaling and upscaling algorithm based on the microporomechanics theory will be introduced to investigate the mechanical properties of coating at a smaller and higher length scale based on the nanoindentation results.

Chapter 5

Microporomechanical Scaling Method - Downscaling

5.1 Introduction

Structural materials such as concrete, rocks and soil are generally treated as homogeneous material in design and construction. However, it has been shown that at a smaller scale level, they are built on multiphase materials, pores and exhibit heterogeneous properties. Exactly how the interaction of the complex microstructure is linked with the mechanical performance has been an enigma that received considerable interest in the research community. In this work, indentation has been adopted to access material information at the microscale. As shown in the previous chapters, indentation results can be represented by the combination of statistical approach and computational simulation. In this chapter, these efforts are further extended with a theoretical approach to decipher the material's mechanical properties at the microscale. The hybrid thermal arc sprayed aluminum and zinc coating is used as an application to demonstrate the role of microporosity in the indentation results. It is further shown that porosity, in general, exists across multiple scale lengths and can be quantified to deduce the corresponding mechanical properties that will be explained in detailed.

5.2 Material Model

The thermal arc sprayed coating is treated as a transversely isotropic model, as shown in Figure 5.1. This model has an isotropic plane $(x_1 - x_2)$, where properties are directionally independent. The rotational axis, x_3, is an axis of symmetry. Such a model is commonly used to represent depositional material such as soil where the axis of symmetry is frequently adopted as the deposition direction. In this case, the rotational symmetric axis x_3 is taken as the spraying direction. During a typical spraying process, coating is sprayed in several passes to create multiple layers as new coating is deposited on the previous layer. For this reason, the transversely isotropic model is most suited to represent the anisotropy of the thermal sprayed coating. Based on existing literature review, the thermal sprayed coating exhibits anisotropic characteristic (Nakamura and Gu, 2007) that is distinct in the spray direction compared to its

perpendicular direction that coincides with layers of splat deposition.
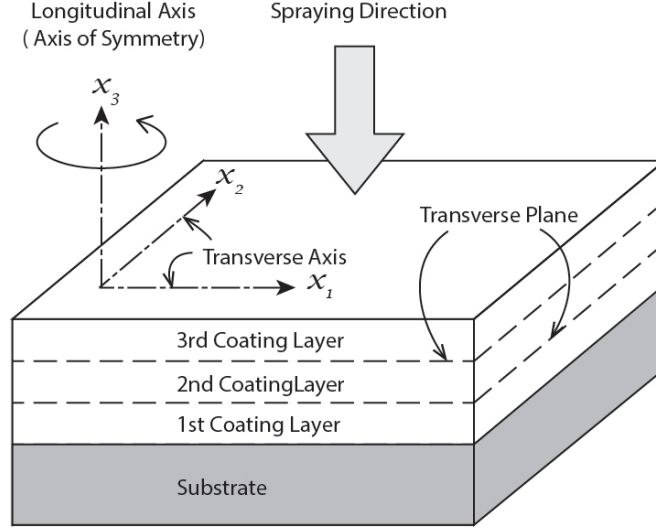
Figure 5.1: A transversely isotropic model with a transversely isotropic plane $(x_1 - x_2)$ and an axis of symmetry (x_3)

5.3 Elastic Constitutive Law

An elastic material is referred to one that has a linear relationship on stress (σ) and strain (ε), where the stress is only dependent on the strain. The Hooke's law is most commonly used to describe the stress-strain relationship for the isotropic elastic solid in uniaxial loading with the Young Modulus (E).

$$\sigma = E\,\varepsilon \tag{5.3.1}$$

The Hooke's law can be re-written in the tensor form to represent the multiaxial case as:

$$\sigma = \mathbb{C}\,\varepsilon \quad or \quad \sigma_{ij} = C_{ijkl}\,\varepsilon_{kl} \tag{5.3.2}$$

where $\mathbb{C}$ or C_{ijkl} is the fourth-order stiffness tensor. Due to the symmetry of the transversely isotropic model (Anandarajah, 2011), the stiffness tensor can be simplified in a matrix form:

$$\mathbb{C} = \begin{bmatrix} C_{1111} & C_{1122} & C_{1133} & 0 & 0 & 0 \\ C_{1122} & C_{1111} & C_{1133} & 0 & 0 & 0 \\ C_{1133} & C_{1133} & C_{3333} & 0 & 0 & 0 \\ 0 & 0 & 0 & (C_{1212} - C_{1122})/2 & 0 & 0 \\ 0 & 0 & 0 & 0 & C_{2323} & 0 \\ 0 & 0 & 0 & 0 & 0 & C_{2323} \end{bmatrix} \tag{5.3.3}$$

The corresponding stiffness compliance matrix, $\mathbb{S}$, can be derived by inverting the stiffness tensor, $\mathbb{C}$. Substituting the stiffness compliance tensor in a matrix form with the stress and strain matrix yields the Hooke's law with the familiar engineering constants:

48

$$
\begin{Bmatrix} \varepsilon_{11} \\ \varepsilon_{22} \\ \varepsilon_{33} \\ \gamma_{12} \\ \gamma_{23} \\ \gamma_{13} \end{Bmatrix} = \begin{bmatrix} 1/E_1 & -\nu_{12}/E_1 & -\nu_{13}/E_3 & 0 & 0 & 0 \\ -\nu_{12}/E_1 & 1/E_1 & -\nu_{13}/E_3 & 0 & 0 & 0 \\ -\nu_{31}/E_1 & -\nu_{31}/E_1 & 1/E_3 & 0 & 0 & 0 \\ 0 & 0 & 0 & 1/G_{12} & 0 & 0 \\ 0 & 0 & 0 & 0 & 1/G_{23} & 0 \\ 0 & 0 & 0 & 0 & 0 & 1/G_{23} \end{bmatrix} \begin{Bmatrix} \sigma_{11} \\ \sigma_{22} \\ \sigma_{33} \\ \sigma_{12} \\ \sigma_{23} \\ \sigma_{13} \end{Bmatrix} \tag{5.3.4}
$$

There are seven independent parameters in Equation 5.3.4, namely, E_1, E_3, G_{12}, G_{23}, ν_{12}, ν_{13} and ν_{31}. By making use of the symmetry of the compliance matrix, the number of independent constants can be reduced from seven to five by adopting Equation 5.3.5 and Equation 5.3.6.

$$
\frac{\nu_{31}}{E_1} = \frac{\nu_{13}}{E_3} \tag{5.3.5}
$$

$$
G_{12} = \frac{E_1}{2(1 + \nu_{12})} \tag{5.3.6}
$$

The final unknown independent parameters hence reduced to E_1, E_3, G_{23}, ν_{12} and ν_{13}. By inverting the $\mathbb{S}$ matrix back into the $\mathbb{C}$ matrix, the constant within the $\mathbb{C}$ can be found in terms of the engineering constants:

$$
C_{1111} = \frac{1 - \nu_{13}^2 \frac{E_1}{E_3}}{E_1 E_3 \, \beta}; \qquad C_{1122} = \frac{\nu_{12} + \nu_{13}^2 \frac{E_1}{E_3}}{E_1 E_3 \, \beta}; \qquad C_{1133} = \frac{\nu_{13}(1 + \nu_{12})}{E_1 E_3 \, \beta}; \qquad C_{2323} = G_{23}
$$

$$
where \quad \beta = \frac{1}{E_1^2 E_3}(1 + \nu_{12})(1 - \nu_{12} - 2\nu_{13}^2 \frac{E_1}{E_3})
$$

$$
\tag{5.3.7}
$$

To further simplify the computational effort by reducing the unknown parameters, the directional and shear Poisson's ratio (Lee et al., 2020) is assumed with the following expression:

$$
\nu_{12} = 0.3;
$$
$$
\nu_{13} + \nu_{31} = 2\,\nu_{12} \tag{5.3.8}
$$

As a result, all the Poisson's ratio is made dependent on the directional elastic modulus, and hence the remaining unknown elastic parameters have been reduced to only E_1, E_3 and G_{23}. The corresponding indentation modulus for both direction x_3 and x_1 can be derived using the expression based on the elastic stiffness tensor as (Delafargue and Ulm, 2004):

$$
M_3 = 2\sqrt{\left(\frac{C_{1111}C_{3333} - C_{1133}^2}{C_{1111}}\right)\left(\frac{1}{C_{2323}} + \frac{2}{\sqrt{C_{1111}C_{3333}} + C_{1133}}\right)^{-1}}
$$

$$
\tag{5.3.9}
$$

$$
M_1 = \sqrt{\sqrt{\frac{C_{1111}}{C_{3333}}\left(\frac{C_{1111}^2 - C_{1122}^2}{C_{1111}}\right)} M_3}
$$

5.4   Plasticity Criteria

The plasticity criteria for the transversely isotropic model is adopted using Hill's yield function (Hill, 1948, 1965) that was originally catered for orthotropic materials.

$$f(\sigma, \sigma_y) = a\,(\sigma_{22} - \sigma_{33})^2 + b\,(\sigma_{33} - \sigma_{11})^2 + 4\,c\,(\sigma_{33})^2 + 2\,d\,(\sigma_{12})^2 = 0 \tag{5.4.1}$$

where σ_y is the uniaxial yield strength, and the coefficient a to d are expressed as the ratio of the directional yield strengths, expressed by:

$$a = \frac{1}{2}\left(\frac{1}{R_{22}^2} + \frac{1}{R_{33}^2} - \frac{1}{R_{11}^2}\right); \qquad b = \frac{1}{2}\left(\frac{1}{R_{33}^2} + \frac{1}{R_{11}^2} - \frac{1}{R_{22}^2}\right);$$

$$c = \frac{1}{2}\left(\frac{1}{R_{23}^2}\right); \qquad d = \frac{3}{2}\left(\frac{1}{R_{12}^2}\right) \tag{5.4.2}$$

The directional yield strength ratio (R) is expressed in terms of the directional yield strength (denoted by a superscript y) and the uniaxial yield strength:

$$R_{11} = \frac{\sigma_{11}^y}{\sigma_y}; \qquad R_{33} = \frac{\sigma_{33}^y}{\sigma_y};$$

$$R_{12} = \sqrt{3}\,\frac{\sigma_{12}^y}{\sigma_y}; \qquad R_{23} = \sqrt{3}\,\frac{\sigma_{23}^y}{\sigma_y}; \tag{5.4.3}$$

For post-yield condition, the plasticity behaviour is assumed to take the form of a power-law function with the work-hardening (n), the uniaxial yield strength (σ_y), the directional elastic modulus (E_{11} and E_{33}) and the equivalent post-yield plastic strain (ε_{pl}).

$$\sigma = \sigma_y \left(1 + \frac{(E_{11} + E_{33})/2}{\sigma_y}\,\varepsilon_{pl}\right)^n \tag{5.4.4}$$

The shear yield strength is adopted using the von Mises yield criterion, expressed as:

$$\sigma_{12}^2 = \frac{\sigma_y}{\sqrt{3}}; \qquad \sigma_{23}^y = \frac{\sigma_y}{\sqrt{3}}\sqrt{\frac{\sigma_{33}^y}{\sigma_{11}^y}} \tag{5.4.5}$$

To further simplify the number of unknown plasticity parameters, the uniaxial yield strength (σ_y) in an isotropic condition can be assumed to be the average of the stresses in directions 11 and 33, as:

$$\sigma_y = \frac{\sigma_{11}^y + \sigma_{33}^y}{2} \tag{5.4.6}$$

As a result, the remaining unknown plasticity parameters are reduced down to σ_{11}^y, σ_{33}^y and n.

5.5 Anisotropic Computational Simulation

As shown in the previous sections, the transversely isotropic model can be simulated using finite element modelling with six elasticity and plasticity parameters, including E_1, E_3, G_{23}, σ_{11}^y, σ_{33}^y and n. The indentation on a transversely isotropic material is simulated using the finite element with ANSYS 2019. A series of anisotropic dimensionless functions, as shown in Equation 5.5.1, are derived using a similar approach described in Chapter 4. An anisotropic database is then derived using these dimensionless functions. The purpose of obtaining these dimensionless functions is to acquire the relationship of the indentation response (left hand side of Equation 5.5.1) with the material properties (right hand side of Equation 5.5.1). Finite element simulation (Details of the model are in Chapter 4) is then carried out using a broad range of material properties combinations based on the design of experiment approach (DOE), as shown in Appendix B. Once the database is ready, artificial neural network (ANN) is used to train the data in the database. The dimensionless functions are solved using the non-linear solver from Matlab (Lee et al., 2018). The objective is to obtain the unknown anisotropic parameters, including E_1, E_3, G_{23}, σ_{11}^y, σ_{33}^y and n.

$$\frac{F_3}{E_3 h_{max}^2} = \Pi_1 \left(\frac{E_3}{E_1}, \frac{G_{23}}{E_1}, \frac{\sigma_{33}^y}{E_1}, \frac{\sigma_{33}^y}{\sigma_{11}^y}, n \right)$$

$$\frac{S_3}{2 E_3 h_{max}^2} = \Pi_2 \left(\frac{E_3}{E_1}, \frac{G_{23}}{E_1}, \frac{\sigma_{33}^y}{E_1}, \frac{\sigma_{33}^y}{\sigma_{11}^y}, n \right)$$

$$\frac{3 W_{total(3)}}{E_3 h_{max}^3} = \Pi_3 \left(\frac{E_3}{E_1}, \frac{G_{23}}{E_1}, \frac{\sigma_{33}^y}{E_1}, \frac{\sigma_{33}^y}{\sigma_{11}^y}, n \right)$$

$$\frac{W_{u(3)}}{E_3 h_{max}^3} = \Pi_4 \left(\frac{E_3}{E_1}, \frac{G_{23}}{E_1}, \frac{\sigma_{33}^y}{E_1}, \frac{\sigma_{33}^y}{\sigma_{11}^y}, n \right) \qquad (5.5.1)$$

$$\frac{h_{r(3)}}{h_{max}} = \Pi_5 \left(\frac{E_3}{E_1}, \frac{G_{23}}{E_1}, \frac{\sigma_{33}^y}{E_1}, \frac{\sigma_{33}^y}{\sigma_{11}^y}, n \right)$$

$$\frac{H_1}{E_1} = \Pi_6 \left(\frac{E_3}{E_1}, \frac{G_{23}}{E_1}, \frac{\sigma_{33}^y}{E_1}, \frac{\sigma_{33}^y}{\sigma_{11}^y}, n \right)$$

5.6 Microstructure Length Scale

The thermal spray coating used in the experiment can be categorised in a multiple scale lengths depends on the measuring resolution. Figure 5.2 shows the coating in three distinct scale lengths. At level 2, the coating image is taken at a 100 μm scale is considered at the macroscale or mesoscale. At this level, the aftermath of splat deposition is visible that forms interlamellar layers that generally measured at 10 to 50 μm (Davis et al., 2004). The uneven surface is clearly distinguishable with cracks network and defects that are a characteristic of thermal sprayed coating (Ang and Berndt, 2014, Toma et al., 2014). The next level down is the level 1 or known as the microscale level. The image taken for this level is at a 2 μm resolution. This is an essential level for this PhD work as the microscale is where the indentation takes place. As the maximum indentation depth used in this study is 2 μm, the indentation impression area can be one to three magnitude bigger. At this level, the coating is presented in the form of irregular particles, or known as grains, measured with a mean size of 0.25 to 0.5 μm (Ang and Berndt, 2014). In between the grains are voids, also referred to as the microscale porosity or microporosity. The microporosity is considerably smaller compared to the indentation depth

for a compact arrangement of grains. The next level down is level 0 or known as the nanoscale level. In this work, the grain is considered as a solid particle, which is comparable to the bulk metal nanostructured crystal formation (Li et al., 2007). Experimental study of nanostructured mechanical behaviour is beyond the capability and the scope of this work. However, nanoscale properties can be predicted based on the theoretical approach by using the multiscale analysis technique.
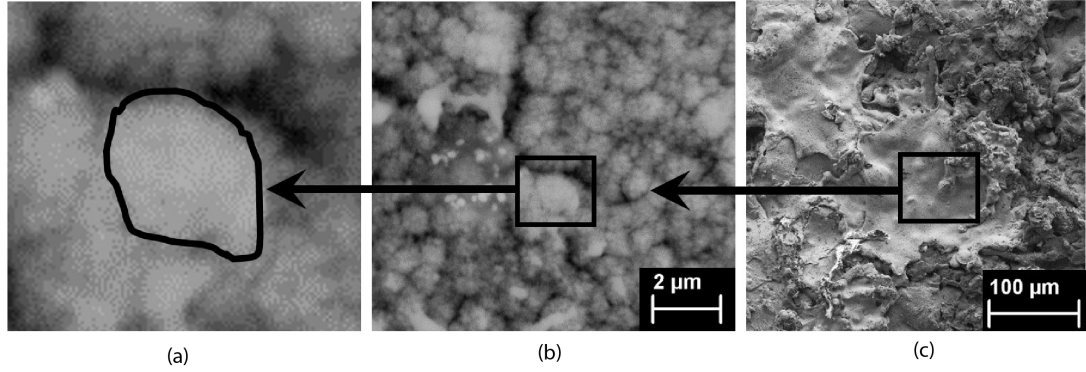
Figure 5.2: SEM images from the thermal arc sprayed composite (aluminum and zinc) coating. (a) Level 0 Nanoscale solid particle (b) Level 1 Microscale solid-porous structures with microporosity between adjacent solid particles (c) Level 2 Mesoscale microstructure showing the molten splat with cracks and pores.

5.7   Micromechanics Scaling Relationship

Consider a simplified porous material, in a finite representative volume element (RVE), composed of two phases, i.e. a cohesive-frictional solid phase and a pore phase. The solid phase has a solid volume fraction, or packing density, η, which is a ratio of the solid volume to the overall RVE volume. The pore phase is effectively the empty spaces in between the solid that can be represented by the porosity, $\varphi = 1 - \eta$. There are two types of porous microstructure morphology considered in this work (see Figure 5.3). The first is the matrix-porosity morphology, or commonly known as the Mori-Tanaka scheme (Mori and Tanaka, 1973). The second is the perfectly disordered, polycrystal morphology, or commonly known as the self-consistency scheme (Jaeger and Nagel, 1992).

A micromechanical link has been established (Ulm et al., 2007) to relate the indentation responses with the material's properties. The link is based on dimensionless indentation modulus and hardness scaling functions, i.e. Π_M and Π_H:

$$M_{hom} = m_s \cdot \Pi_M \left(\frac{\mathbb{C}}{\mathbb{C}^s}, \eta, \eta_0 = 0.5 \right)$$
$$H_{hom} = c_s \cdot \Pi_H \left(\alpha_s, \eta, \eta_0 = 0.5, \theta \right)$$

$$(5.7.1)$$

The indentation modulus, M_{hom} and indentation hardness H_{hom} are the indentation response obtained from the procedure outlined in Chapter 2. The subscript *hom* denoted by the homogenised result. Note that the indentation modulus (M) is used here instead of elastic modulus (E), where $M = E/(1 - v^2)$. The solid properties are represented by a subscript s in the mechanical properties, including indentation modulus (m_s), cohesion (c_s), and friction an-
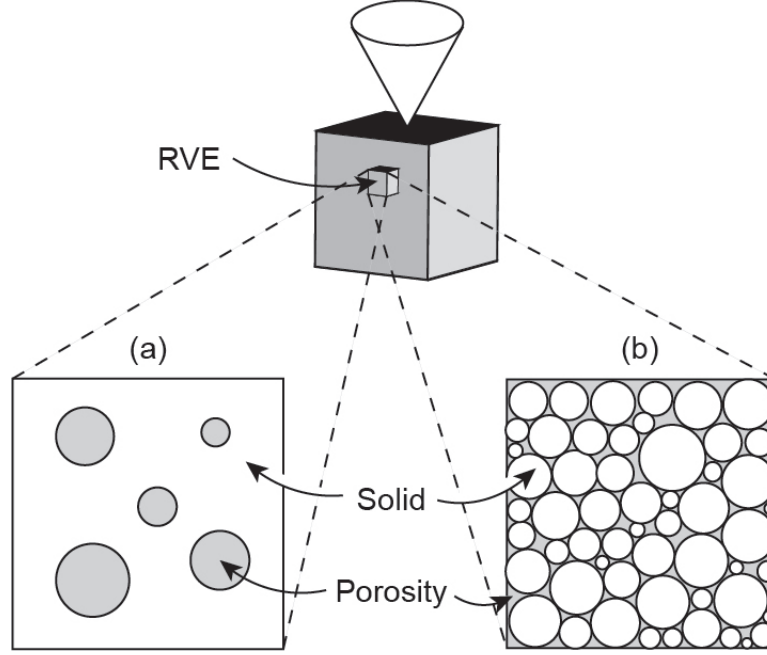
Figure 5.3: Porous microstructure RVE consists of solid and pore phase, shown in two different morphologies: (a) matrix-pore inclusion morphology, or Mori-Tanaka scheme ($\eta_0 = 0$) (b) Perfectly disordered polycrystal morphology, or Self-consistent scheme ($\eta_0 = 0.5$).

gle (α_s). These solid mechanical properties are parameters adopted from the yield criterion for a Drucker-Prager material model (Cariou et al., 2008). For the self-consistency scheme, a solid percolation threshold, η_0, is described as the solid fraction required to maintain a load-sustaining system with a continuous load transfer path through the solid particles. The solid percolation threshold, below which the system is unable to sustain any load, is assumed to be 0.5 which is close to the limit (Onoda and Liniger, 1990). The stress and strain behaviour of the material is represented by the solid stiffness tensor ($\mathbb{C}^s$) and expressed as a ratio to the homogenised stiffness tensor ($\mathbb{C}$).

5.7.1 Indentation Modulus Scaling function

The indentation modulus scaling function has been investigated previously (Dormieux et al., 2006, Ulm et al., 2007), where the Π_M is given as:

$$\Pi_M\left(r_s, \eta, \eta_0 = 0.5\right) = \frac{\Im\left(9\eta r_s + 4\Im + 3r_s\right)\left(3r_s + 4\right)}{4\left(4\Im + 3r_s\right)\left(3r_s + 1\right)} \tag{5.7.2}$$

where r_s is defined as the ratio of the solid bulk modulus (k) to the shear modulus (g). Two common methods of deducing the bulk modulus and shear modulus from the $\mathbb{C}^s$, namely the Voigt Method (with subscript V) (Voigt et al., 1928) and Reuss Method (with subscript R) (Reuss, 1929), are adopted. It is known that the Voigt and Reuss method represent an upper bound and lower solution to the bulk and shear modulus, respectively. Therefore it is prudent to derive the r_s term using the Voigt-Reuss-Hill average method (with subscript VRH) by compressing the $\mathbb{C}^s$ into a quasi-isotropic state (Ortega et al., 2007).

$$k_V = \frac{1}{9}\left(2C^s_{1111} + C^s_{3333}\right) + \frac{2}{9}\left(C^s_{1122} + 2C^s_{1133}\right)$$

$$g_V = \frac{1}{15}\left(2C^s_{1111} + C^s_{3333}\right) - \frac{1}{15}\left(C^s_{1122} + 2C^s_{1133}\right)$$

$$+ \frac{1}{5}\left(2C^s_{2323} + \frac{1}{2}\left(C^s_{1111} - C^s_{1122}\right)\right)$$

$$k_R = \frac{1}{\wp\left(C^s_{1111} + C^s_{1122} + 2C^s_{3333} - 4C^s_{1133}\right)}$$

$$g_R = \frac{15}{2\wp\left(2\left(C^s_{1111} + C^s_{1122}\right) + 4C^s_{1133} + C^s_{3333}\right)} + 6\left(\frac{1}{C^s_{2323}} + \frac{1}{\left(C^s_{1111} - C^s_{1122}\right)/2}\right)$$

$$\wp = \left[C^s_{3333}\left(C^s_{1111} + C^s_{1122}\right) - 2C^{s\,2}_{1133}\right]^{-1}$$

$$k_{VRH} = \frac{1}{2}\left(k_V + k_R\right); \quad g_{VRH} = \frac{1}{2}\left(g_V + g_R\right)$$

(5.7.3)

The composite solid shear modulus ratio, $\Im$, can be expressed as

$$\Im = \frac{1}{2} - \frac{5}{4}\left(1 - \eta\right) - \frac{3}{16}r_s\left(2 + \eta\right)$$
$$+ \frac{1}{16}\sqrt{144\left(1 - r_s\right) - 480\eta + 400\eta^2 + 408r_s\eta - 120r_s\eta^2 + 9r_s^2\left(2 + \eta\right)^2}$$

(5.7.4)

5.7.2 Hardness Scaling Function

The derivation of the hardness scaling function is based on the strength-based approach developed by Dormieux and co-workers (Cariou et al., 2008, Dormieux et al., 2006, 2017) since the hardness is measured when the material has undergone plasticity. In other words, the measurement of hardness is a function of the material yield criterion. The starting point of the hardness definition is to relate the indentation in terms of energy, or work done. The work rate provided by a rigid conical indenter in an infinite half-space is given by:

$$W = P\,\mathring{h} = \int_\Omega \Sigma\!:\! D \, d\Omega$$

(5.7.5)

where $\mathring{h}$ is the indentation rate, Σ is the Cauchy stress, D is the Cauchy strain rate in the half-space Ω. The stress field is statically admissible, satisfying equilibrium and assumed frictionless contact. Substituting the work rate equation into the hardness definition will give:

$$H = \frac{P}{A_c} = \frac{W}{\mathring{h}\,A_c} = \frac{1}{\mathring{h}\,A_c}\int_\Omega \Sigma\!:\! D \, d\Omega \quad \text{or}$$
$$H = \frac{1}{A_c}\int_\Omega \Sigma\!:\! D \, d\Omega \quad \text{when } \mathring{h} = 1$$

(5.7.6)

To incorporate this hardness definition into a yield design criterion, the product of the stress

and strain rate field has to be replaced by a dissipation or support function $\Pi(D)$ in the realm of a strength compatible stress state (G_s) that takes the form of a convex shape. Here, D is taken as the form of a symmetrical second-order tensor. By adopting the dual definition of the strength criterion, the $\Pi(D)$ can be defined in the G_s realm with the following conditions:

$$\begin{cases} \text{Condition (1)}: & \Sigma \in G_s, \ F(\Sigma) \leq 0 \\ \text{Condition (2)}: & \Pi(D) = sup\,(\Sigma \colon D, \ \Sigma \in G_s) \\ \text{Condition (3)}: & \text{At yield, } \Sigma \in \partial G_s, \ \Sigma = \dfrac{\partial \Pi(D)}{\partial D} \end{cases} \qquad (5.7.7)$$

Provided the conditions in Equation 5.7.7 are met, the entire material system Ω is considered to collapse plastically. In other words, the work done by the external force has caused the material system (Ω) dissipation capacity to be exhausted with the development of the stress field (Equation 5.7.5) in plasticity. The phenomenon of the plasticity dissipation can be described with the classical lower and upper bound limit analysis of yield design (Sloan and Kleeman, 1995, Tang et al., 2014). The solutions described by the limit analysis yields two outcomes. The first solution is the lowest estimate of an upper bound solution, denotes by the supremum (sup), when the statically and plastically admissible stress field (Σ^{SA}) conditions are satisfied. The second solution is the highest estimate of a lower bound solution, denotes by the infimum (inf) when the plastic strain rate field (D^{KA}) is derived that is kinematically compatible with the velocity field ($\underline{U}$) and the normality rule of plastic flow. Both these hardness estimates are presented below:

$$\begin{cases} \text{Lowerbound}: & H = \dfrac{1}{A_c} \sup_{F(\Sigma\ \text{SA}) \leq 0} \displaystyle\int_{\Omega} \Sigma^{SA} \colon D \ d\Omega \quad \text{when } \mathring{h} = 1 \\ \text{Upperbound}: & H = \dfrac{1}{A_c} \inf_{\underline{U}\ \text{KA}} \displaystyle\int_{\Omega} \Pi(D^{KA}) \ d\Omega \quad \text{when } \mathring{h} = 1 \end{cases} \qquad (5.7.8)$$

The dissipation function can be expressed in the form of

$$\Pi(D^{KA}) = c_s \sqrt{\mathcal{A}D_v{}^2 + 4\mathcal{B}D_d{}^2} - \mathcal{C}D_v{}^2$$

$$\text{where } D_d{}^2 = J_2 = \frac{1}{2}\Delta \colon \Delta \quad \text{and} \quad D_v = \text{trace } D \qquad (5.7.9)$$

The dissipation function is shown to depend on both the macroscopic strain rate invariants (D_v and D_d), which is also found to relate back to the macroscopic stress invariants (Σ_m and Σ_d) in the form of $\Sigma = \mathbb{C}^{hom} \colon D$, where $\mathbb{C}^{hom}$ is the homogenised elastic tensor and k^{hom} and g^{hom} are the homogeneous bulk and shear modulus respectively.

$$\Sigma_m = \frac{1}{3}tr\Sigma = k^{hom}D_v; \qquad \Sigma_d = \sqrt{\frac{1}{2}\Sigma_d \colon \Sigma_d} = 2g^{hom}D_d \qquad (5.7.10)$$

The macroscopic stress invariants can be used to plot the strength domain (G_s) by substituting into the strain rate invariants in Equation 5.7.9, resulting in an elliptical strength criterion, expressed as:

$$F(\Sigma_m, \Sigma_d) = \frac{{\Sigma_d}^2}{B} + \frac{C - {\Sigma_m}^2}{A} - 1 = 0 \tag{5.7.11}$$

The strength criterion from Equation 5.7.11 has a closed ellipse form provided that $B > 0$. In the case when $B \leq 0$, the strength criterion becomes a hyperbolic shape, see Figure 5.4. The values of the constants A, B and C depend on the porous material morphology in terms of the friction angle (α_s) and the porous material packing density (η).
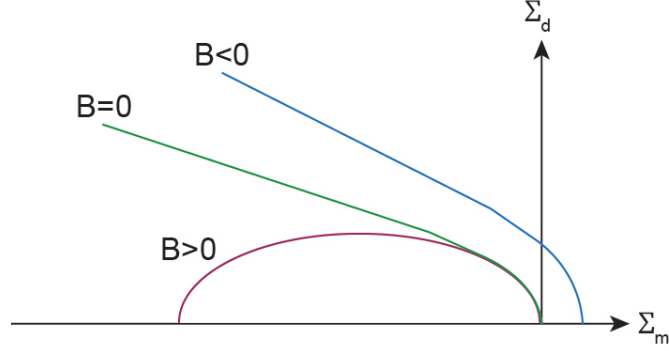
Figure 5.4: Cohesive-strength yield criterion: elliptical criterion when B>0, parabola criterion when B=0 and B<0. Position on the axes for illustration only.

As highlighted by Johnson (1985), while the lower bound solution can be readily derived analytically, the upper bound solution is proven to be more challenging to implement, if not possible, using the proposed classical slip lines method. Cariou et al. (2008) has derived the lower bound solution for hardness, but only for a flat punch indenter. For this reason, The derivation of hardness has to be resorted to a computational approach using continuum discretization of the finite element with linear programming technique (Cariou et al., 2008) to solve for the upper bound solution. The upper bound hardness problem can be presented as:

$$H = \frac{c_s}{A_c} \min_{\underline{U} \; \mathrm{KA}} \int_{\Omega} \left[\sqrt{\mathcal{A}{D_v}^2 + 4\mathcal{B}{D_d}^2} - \mathcal{C}{D_v}^2 \right] d\Omega \quad \text{for } \mathring{h} = 1$$

$$\text{or} \quad \frac{H}{c_s} = \Pi_H(\alpha_s, \eta) \tag{5.7.12}$$

By treating the above hardness problem as a second-order conic optimization problem, the hardness solution can be obtained using advanced solver algorithm, MOSEK (Mosek, 2015), incorporated and implemented by MATLAB (Mat, 2019). The outcome of the hardness solution is expressed in terms of the solid friction angle (α_s) and packing density (η) for a self-consistent material scheme. The Π_H solution is given by:

$$\Pi_H(\alpha_s) = \Pi_0 \left[1 + (1 - \eta)\xi - (d - e\eta)\xi^2 - (f - g\eta)\alpha_s^5 \right]$$

$$\text{where} \quad \Pi_0 = \frac{12\eta(a - b\eta)\left[(2\eta - 1)(2 + \eta)\right]^{1/2}}{(1 - c\eta)(2 + \eta)} \tag{5.7.13}$$

and the coefficients are given as (Ulm et al., 2007):

$$a = 0.19567; \qquad b = 0.03739; \qquad c = 0.77999; \qquad d = 20.3138;$$
$$e = 31.5352; \qquad f = 52.1817; \qquad g = 99.3465;$$

<div align="right">(5.7.14)</div>

It is worth noting here that in the situation when the strength criterion takes the form of a hyperbolic form, the hardness problem is no longer able to be solved as a second-order conic optimization problem. This remains as a limitation of the currently presented algorithm. The presented result in the following sections in this chapter falls demonstrate a condition when the downscaling algorithm works with the ellipse form of strength criterion. However, this may not be the case for all the range of porous material parameters. This issue will be further discussed in the next chapter when it is necessary to introduce a new scaling relationship algorithm to cater for the hyperbolic form of strength criterion.

5.8 Downscaling (Inverse) Algorithm

Consider the self-consistent model of a porous material, an inverse algorithm based on the micromechanics scaling relation can be implemented to determine the solid properties, including the stiffness tensor ($\mathbb{C}^s$), packing density (η), the indentation modulus (m_s) and the cohesion (c_s). A total number of N experimental indentation tests was used as input information where the anisotropic indentation response have been determined using the machine learning approach described in the previous section. This inverse algorithm is also known as a downscaling algorithm, where through the indentation on a porous surface, the solid properties and the corresponding pores information can be deduced using this inverse algorithm. The downscaling algorithm is illustrated in Figure 5.4, where an indentation impression is superimposed on top of the irregular microstructure that has been simplified into a self-consistent and perfectly disordered solid-porous model. Note that the indentation depth is chosen so that the indentation impression only covers material with the same phase. Also, the size of the pores is much smaller than the indentation depth, h, the collected indentation result will represent the composite properties of both the solid and porosity.
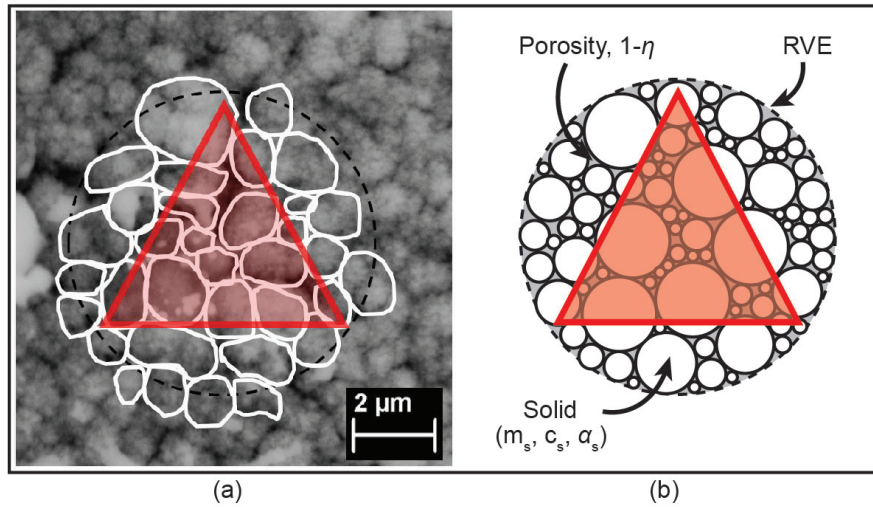
Figure 5.5: Indentation carried out on a solid-porous medium consists of solid particle and microporosity at the microscale (level 1). (a) Indentation surface (red) located within an RVE capturing the response from both the solid particle and porosity at the microscale (level 1) (b) Self-consistent, perfectly disordered, granular model

A two-step inverse algorithm is carried out by minimising the difference between the experimental indentation response with theoretical derivation from the dimensionless scaling functions. The first step is to obtain the $\mathbb{C}^s$ by minimising the difference in the experimental indentation modulus and the dimensionless scaling functions. The outcome $\mathbb{C}^s$ is to be used to calculate the directional solid stiffness for both directions, i.e. $m_{s(1)}$ and $m_{s(3)}$. The subscript (1) and (3) on the indentation modulus are referred to the data from x_1 and x_3 direction, respectively. The minimising problem from the first step can be expressed as:

$$\min_{\mathbb{C}^s, \eta} \sum_{i=1}^{N} \left[\left(1 - \frac{m_{s(1)} \Pi_M}{M_{i(1)}} \right)^2 + \left(1 - \frac{m_{s(3)} \Pi_M}{M_{i(3)}} \right)^2 \right] \qquad (5.8.1)$$

Following the determination of the directional solid stiffness modulus, the second steps is to determine the plasticity parameters by minimising the difference between the experimental indentation modulus and hardness with the respective dimensionless scaling functions. The subscript J refers to the direction of x_1 and x_3. The second step minimisation problem can be expressed as:

$$\min_{c_s, \alpha_s, \eta} \sum_{i=1}^{N} \left[\left(1 - \frac{m_{s(J)} \Pi_M}{M_{i(J)}} \right)^2 + \left(1 - \frac{c_{s(J)} \Pi_H}{H_{i(J)}} \right)^2 \right] \qquad where \quad J \in 1, 3 \qquad (5.8.2)$$

5.9 Effects of Microporosity

Experimental indentation has been carried out on the coating to evaluate the anisotropic mechanical properties based on a transversely isotropic model. Indentation result for the x_1 directions has been obtained using the anisotropic computational simulation and artificial neural network trained database based on the experimental x_3 result. The procedure to obtain the indentation result is summarised in Figure 5.5.
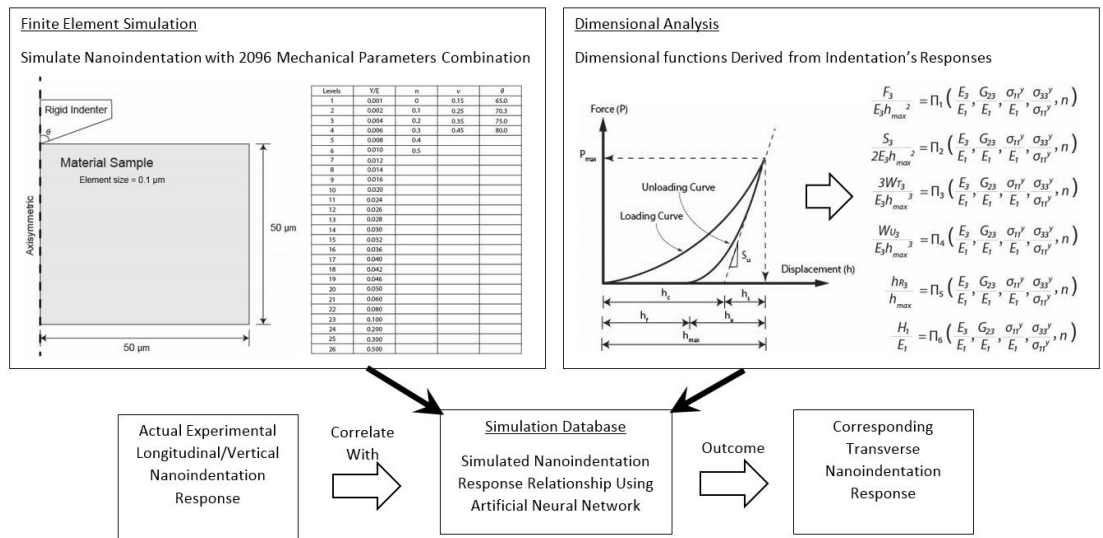
Figure 5.6: Flow chart showing the derivation of the anisotropic mechanical properties using a combination of finite element simulation, dimensional analysis and artificial neural network

Statistical deconvolution is carried out to identify the the transverse (x_3) and longitudinal (x_1)

directions indentation modulus, hardness and volume fraction for the aluminum and zinc phases. The deconvolution result is shown in Table 5.1. The result indicates that thermal sprayed coating exhibits anisotropic mechanical properties that have been reported in the literature (Nakamura and Gu, 2007, Tan et al., 2010). The anisotropic ratio for the indentation modulus is relatively small at 20% for aluminum and 7% for zinc. This observation is in line with the previous investigation (Vlassak and Nix, 1994) that found the anisotropic ratio of the indentation modulus is not apparent for transversely isotropic materials such as coating. The range of values from these mechanical properties agrees well with this literature which is lower compared to the bulk material. Hardness is observed to have a higher anisotropic ratio at 60% for aluminum and 40% for zinc. Anisotropic hardness result is rare in the literature, but this observation is close to the reported investigations Vlassak and Nix (1994), Wang et al. (2013). The anisotropic characteristic of the coating can be observed in the cumulative distribution function plots, as shown in Figure 5.6.

Table 5.1: Statistical deconvolution result of indentation modulus, hardness and packing density

Direction	Phase	Elastic Modulus, E (GPa)		Hardness, H (GPa)		Packing Density		Volume Fraction %
		Mean	StD	Mean	StD	Mean	StD	
x1	Aluminum	45.602	36.397	1.262	0.723	0.616	0.094	82
	Zinc	108.780	22.473	2.311	2.145	0.798	0.016	18
x3	Aluminum	35.395	29.514	0.738	0.525	0.616	0.075	65
	Zinc	93.149	12.585	1.183	0.202	0.790	0.010	35

Each indentation location is assigned with a packing density for both directions as a result of the deconvolution process. The values of the mean packing density for aluminum and zinc, 0.616 and 0.790 respectively, are close to the highest packing density of 0.74 that is achievable for a face-centred cubic (FCC), and hexagonal close packed (HCP) system respectively. These results implied that the metal crystal structure of the coating is similar to the bulk material, except that they are relatively loosely packed. The reason behind the difference in the packing density of the coating compared to the bulk material is not known. However, it is hypothesised that the relatively low packing density may be due to the imperfect rearrangement of the crystal structure, or known as grain boundary defects, following the spraying and splat deposition process. This spraying condition is considerably different compared to the heat and pressure introduced while forging the bulk material. It is this packing density determined from indentation that offers the answer to explain why the coating's indentation modulus is lower compared to the bulk material. The indentation modulus has a linear relationship with the packing density, as seen in Figure 5.7. As the packing density reduces, so does the indentation modulus. For this reason, to find out the indentation modulus, one has to first determine the packing density of the coating's metallic crystal microstructure.

While the indentation modulus is a measure of the solid stiffness following a linear relationship (Hooke's law), the hardness is observed to have a non-linear relationship with the packing density. The hardness is plotted with the packing density shown in Figure 5.8. Recalled that the indentation with a sharp tip indenter always leads to almost instant plasticity in the material due to the close to singularity condition as the tip indented into the material surface (Fischer-Cripps, 2004). For this reason, the hardness result effectively falls in the plasticity range that is non-linear in nature. The combined aluminum and zinc indentation and hardness plots are shown in Figure 5.9. It should also be noted that as the packing density approaching the percolation threshold, $\eta_0 = 0.5$, both the indentation modulus and hardness are close to

zero. The percolation threshold represents the limit where the material system can transmit load through a valid load-bearing path. As a result, When the packing density falls below the percolation threshold, the material system is no longer capable of sustaining the load, and therefore has zero indentation modulus and hardness.
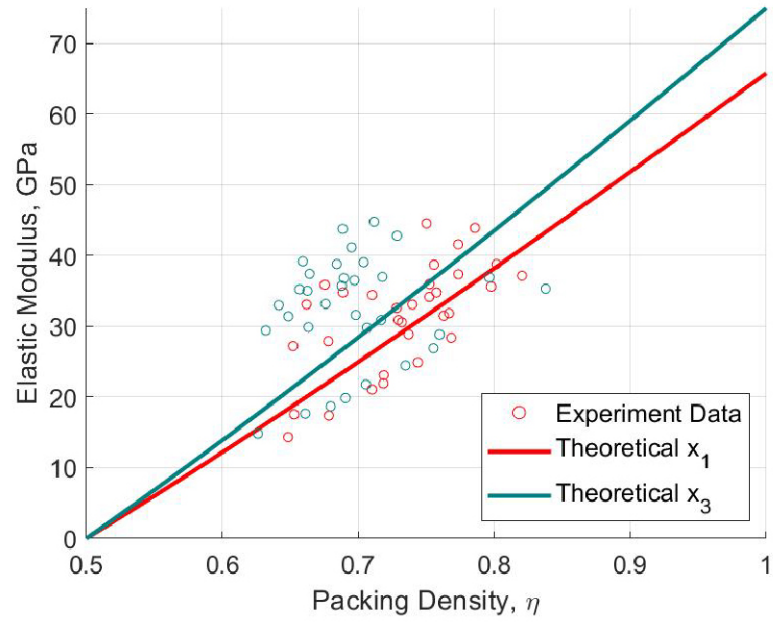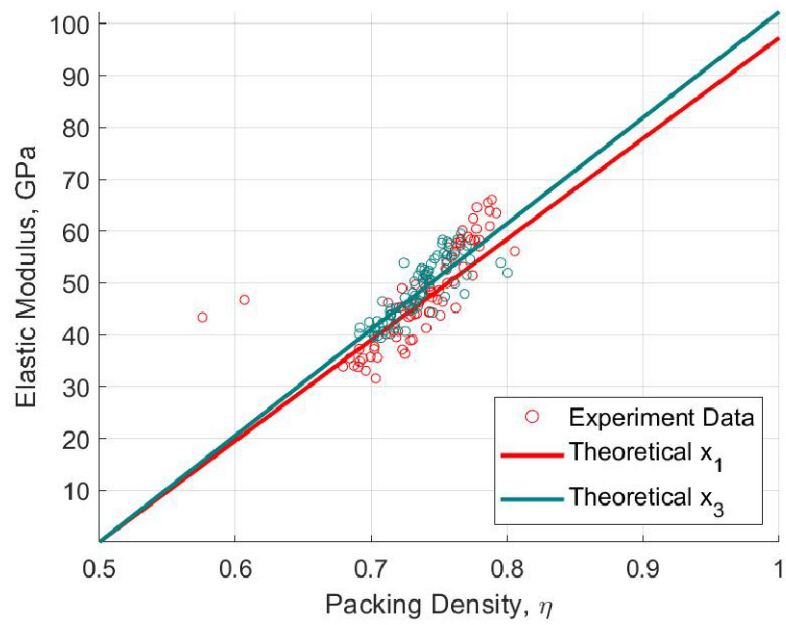
Figure 5.7: Scaling relationship of indentation modulus with packing density (a) aluminum (b) zinc
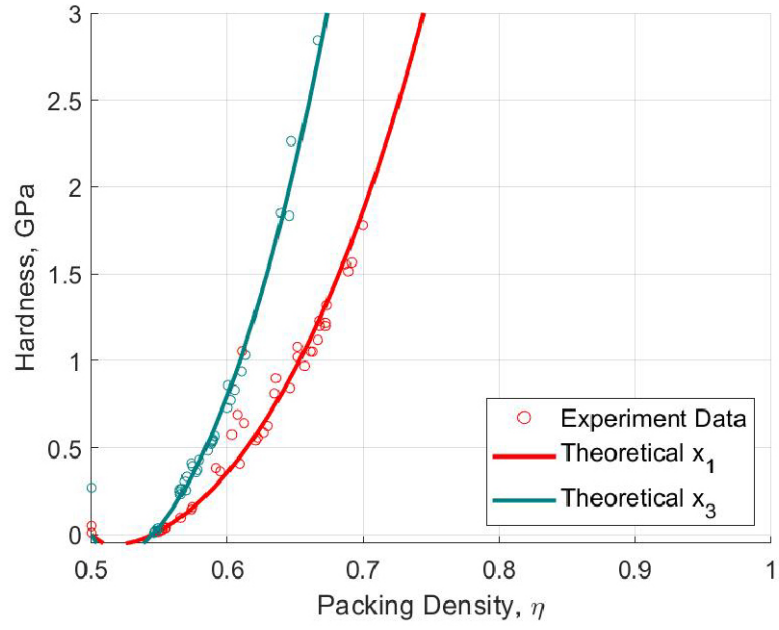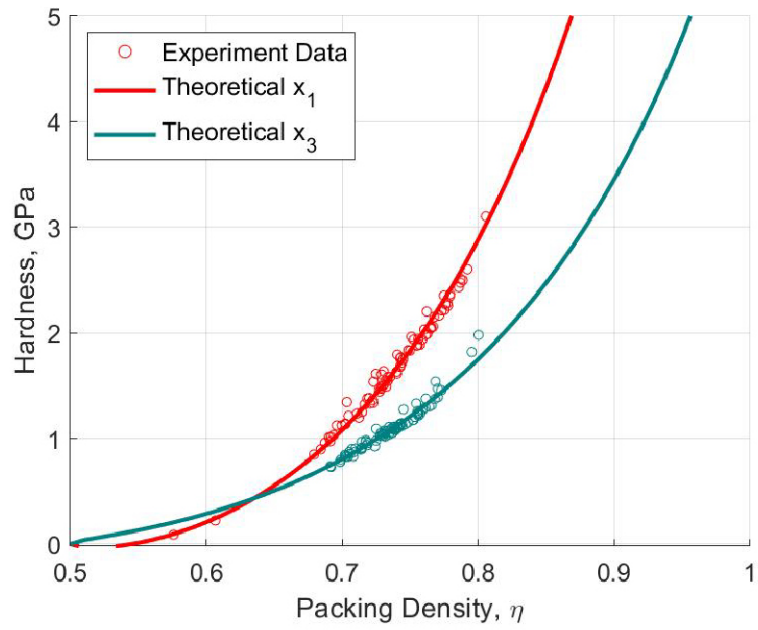
Figure 5.8: Scaling relationship of hardness with packing density (a) aluminum (b) zinc
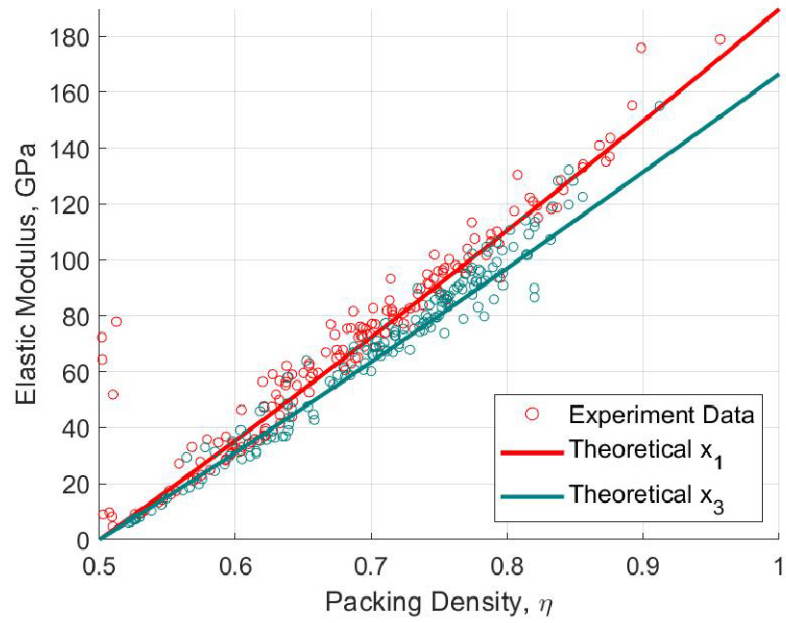
(a)
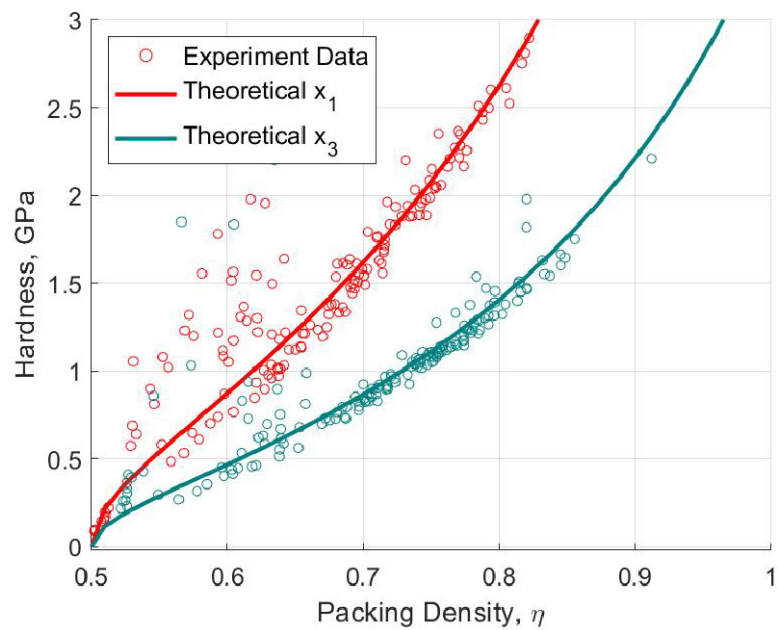
(b)

Figure 5.9: Scaling relationship with packing density for the combined aluminum and zinc (a) indentation modulus (b) hardness

5.10 Nanoscale Solid Properties

While it is not possible to directly measure the nanoscale mechanical properties due to the limitation in the indentation hardware, it is possible to predict the nanoscale solid mechanical properties theoretically. Through the use of the downscaling algorithm, the solid particle's stiffness tensor, $\mathbb{C}^s$, can be determined as presented in the previous chapter. Once the $\mathbb{C}^s$ is known, the theoretical elastic modulus and shear modulus can be calculated (see Equations 5.3.4 to 5.3.8). Compared to the conventional method using molecular dynamics simulation and advanced nanoscale experimental, this proposed downscaling algorithm is shown to successfully derive the nanoscale solid properties that are close to those reported in the literature (Choudhary et al., 2014, Dickel et al., 2018, Jang et al., 2018, Pascuet and Fernández, 2015, Römer et al., 2009). The results are presented in Table 5.2 and Table 5.3. It is observed that the calculated transverse and longitudinal elastic modulus for both the aluminum and zinc are very close ($<4\%$). This outcome suggests that the elastic behaviour for both these materials can be considered isotropic. The microporosity is different in the transverse and longitudinal directions. Since the isotropic condition is observed in the elastic modulus, it is further suggested that the material's elastic stiffness is mostly unaffected by the microporosity. Therefore, it can be concluded that the solid's elastic stiffness does not contribute to the anisotropic condition. The anisotropic properties are instead found to be dominantly attributed from the solid particle's plasticity properties.

Table 5.2: Aluminum - Elastic Stiffness Matrix and Corresponding Elastic Modulus

Phase	Pascuet et al. (2015)	Choudhary et al. (2014)	Present Work
C1111	113.5	114.0	119.2
C1122	61.6	61.6	70.3
C1133	N.A.	N.A.	75.6
C2323	45.4	31.6	42.2
C3333	N.A.	N.A.	128.4
Elastic Modulus, E_1 (GPa)			65.7
Elastic Modulus, E_3 (GPa)			68.0

Table 5.3: Zinc - Elastic Stiffness Matrix and Corresponding Elastic Modulus

Phase	Jang et al. (2018)	Dickel et al. (2018)	Romer et al. (2009)	Present Work
C1111	133.4	177.0	179	170.3
C1122	47.02	34.8	38	53.3
C1133	41.51	52.8	55	51.1
C2323	34.14	45.9	46	104.5
C3333	122.42	68.5	69	162.4
Elastic Modulus, E_1 (GPa)	110.3	136.0	134.9	145.3
Elastic Modulus, E_3 (GPa)	103.3	42.2	41.1	139.1

The plasticity parameters result for both aluminum and zinc following the minimisation algorithm is presented in Table 5.4. As explained earlier, the difference in stiffness for both directions is relatively small, which is 13% for aluminum and 6% for zinc. This is consistent

with the observation made earlier where stiffness is the dominant elastic parameters for the evaluation of the elastic modulus. The difference in cohesion (c_s) and friction angle (α_s) for both directions have shown significant anisotropic results for aluminum and zinc. The anisotropic ratio in the cohesion is close to 5 folds for aluminum and 3.5 folds for zinc. The anisotropic ratio in friction angle is close to 30% for aluminum and 70% for zinc. A large anisotropic ratio is observed in the plasticity parameters. Therefore, it can be concluded that the anisotropy in the thermal sprayed coating is influenced predominantly by the material's plasticity yield criterion. In other words, this work shows that the coating's anisotropy is a result of yield and post-yield hardening. During the spraying process, the metal particles are atomised under the high-intensity heat of the arc, accelerated by the jet of air, cooled down and deposited onto the substrate. This process is likely causing the metal particles to undergone plastic deformation as a result of the exposure to high heat-intensive and kinetic pressure (Deshpande and Sampath, 2005, Grujicic et al., 2003). It is hypothesised in this work that due to the drastic plasticity transformation, the grain boundary condition has undergone changes resulting in the new microporosity arrangement.

The microporosity has been shown to have an impact on the anisotropy characteristic, as shown in Figure 5.9. It is also noted that higher stresses are observed in the transverse direction, which is the spraying direction, with the cohesion and friction angle values being dominant in this direction. What this implies is that the plasticity deformation in the coating is dominantly affected by the mechanical effect in the spraying direction. The predominant influence in the spraying direction can be explained by the kinetic pressure asserted as a result of the air jet. For this reason, the metal particles being deposited under the influence of the air jet sustain more significant plasticity deformation in the transverse direction compared to the longitudinal direction. The later is effectively unconstrained, and therefore metal deformation in this direction would differ significantly compared to the transverse direction. This observation and conclusion is further supported by the literature showing the yield strength is dominant in the spraying direction (Nakamura and Gu, 2007, Nakamura et al., 2000).

Table 5.4: Aluminum and zinc solid particle mechanical properties

Phase	Plasticity Parameters	Longitudinal (x_1 or x_2)	Transverse (x_3)
Aluminum	Stiffness, m_s (GPa)	85.51	97.64
	Cohesion, c_s (GPa)	0.182	0.929
	Friction Angle (Degree)	39.83	32.38
Zinc	Stiffness, m_s (GPa)	166.91	177.05
	Cohesion, c_s (GPa)	0.099	0.349
	Friction Angle (Degree)	39.83	25.69

5.11   Summary and Conclusion

Indentation carried out in the microscale level can access the porous material mechanical properties. By modelling a porous material with several phases, transversely isotropic, self-consistent material system, the separate solid and pores characteristics can be determined using the micromechanical scaling relationship approach. This downscaling algorithm is capable of deriving the microporosity relationship with the indentation results and further be used to obtain the mechanical properties of the nanoscale solid particle. It has been demonstrated in this Chapter

that the presented downscaling algorithm can be used to isolate the elasticity and plasticity parameters from the individual aluminum and zinc phase, in the hybrid coating based on experimental indentation results. The observation made from this work allows the following conclusion to be drawn:

1. Indentation response can be isolated using the statistical deconvolution technique provided that the indentation depth is selected to collect responses only from a single-phase material. The microporosity can be theoretically calculated from the dimensional scaling functions using the minimisation process. The outcome shows that the hardness from the indentation has a non-linear relationship with the packing density and exhibits anisotropic characteristics.

2. The microporosity captured in the dimensional scaling functions has a packing density lower but close to the theoretical highest spherical packing ratio for the face-centre cubic (FCC) and hexagonal close packed (HCP) systems that are known for the aluminum and zinc, respectively. This observation further suggests that the lower values in the indentation modulus and hardness captured by the indentation process compared to the bulk material is attributed to the relatively loosely packed microporosity. The reason of the change in the microporosity in the coating compared to the bulk material may be due to the effect of the spraying process, deposition mechanism under the influence of high heat intensity and kinetic pressure.

3. The difference in the indentation modulus for both the transverse and longitudinal (spraying) directions is relatively insignificant. Since porosity does not have stiffness, this suggests that the solid elastic stiffness properties is largely isotropic, and hence does not contribute to the overall anisotropic characteristic of the coating. This observation further indicates that the coating's anisotropy characteristic is related to the solid particle's plasticity parameters.

4. The solid particle plasticity parameters result shows a significant anisotropic ratio for its longitudinal and transverse direction, with the latter being dominant. The cohesion and friction angle are the key parameters to describe the material yield criterion, and therefore the coating anisotropy is influenced by the yield and post-yield strain hardening effect. High plastic stresses are found to coincide with the spraying direction as a result of the deposition of the splat under the relatively high kinetic pressure due to the air jet. It is hypothesised that the plasticity deformation is different in the spraying (longitudinal) and the transverse directions. The dominant plastic deformation in the spraying direction resulted in a higher packing density following grain boundary redistribution, which gives rise to the anisotropy.

Chapter 6

Microporomechanical Scaling Method - Upscaling

6.1 Introduction

In this chapter, an upscaling algorithm is presented by using indentation result to predict the coating bond strength. A typical bond strength test is performed by applying a tensile force to break a specific segment of the coating or separate the coating from the substrate. The upscaling algorithm is based on the linear comparison composite (LCC) method, which serves as an extension from the downscaling methodology used in the previous chapter. A multiscale model is presented to show how the aluminum and zinc phase of the coating is combined to form a single hybrid phase. A weak interfacial layer between the hybrid coating and the substrate is introduced to model the the separation of the coating from the substrate under a tensile force. The theoretical derivation of the macroscale mechanical properties of the coating strength is then compared to the macroscopic experimental testing results.

6.1.1 Composite Morphology

The mechanical properties of a porous composite are related to the composite morphology by describing the interaction among the different phases in the form of solid and porosity. The mechanical properties for a homogenised medium are represented by two dimensionless-morphology factors, which are $\mathcal{K}$ and $\mathcal{M}$. These factors are related to the homogenised bulk modulus (k_{hom}) and homogenised shear modulus (g_{hom}) with the shear modulus (g_i) of the individual phase, presented as:

$$\mathcal{K} = \frac{k_{hom}}{g_i}; \qquad \mathcal{M} = \frac{g_{hom}}{g_i} \qquad (6.1.1)$$

The Mori-Tanaka scheme (Mori and Tanaka, 1973) is a classical multiscale analysis technique that can be used to find the response of a composite, which consists of a matrix and inclusion. A homogenised composite can be described as a material system that exhibits the behaviour from two distinct materials that are treated as matrix (with subscript i) and inclusion (j). The

proportionality of the matrix and inclusion in the material system can be described by the volume fraction of the matrix (f_i). The dimensionless morphology factors can be expressed in an alternative form as:

$$\mathcal{K} = \frac{4\alpha_i{}^2 - 4\alpha_i{}^2 f_i + \alpha_j{}^2 f_i r_g + 20\alpha_i{}^2 + 8\alpha_i{}^2 f_i r_g + 15}{3\alpha_i{}^2 f_i + 3\alpha_i{}^2 r_g + 4\alpha_i{}^2\alpha_j{}^2 r_g - 3\alpha_j{}^2 f_i r_g}$$

$$\mathcal{M} = \frac{9 f_i r_g - 9F - i - 8\alpha_i{}^2 f_i + 20\alpha_i{}^2 + 8\alpha_i{}^2 f_i r_g + 15}{6 f_i + 15 r_g - 6 f_i r_g + 12\alpha_i{}^2 f_i + 20\alpha_i{}^2 r_g - 12\alpha_i{}^2 f_i r_g}$$

$$(6.1.2)$$

where r_g is the ratio of the shear modulus of the matrix to the inclusion ($r_g = g_i/g_j$).

In the case of a solid-porosity composite, the porosity becomes the inclusion and the solid becomes the matrix. The dimensionless morphology factors can be simplified by adopting $k_j = g_j = 0$, as

$$\mathcal{K} = \frac{4 f_i r_g k_i}{4 g_i + 3 k_i - 3 f_i k_i}$$

$$\mathcal{M} = \frac{f_i(8\alpha_i{}^2 + 9)}{20 g_i + 15 k_i - 12 f_i g_i - 6 f_i k_i}$$

$$(6.1.3)$$

6.2   Linear Comparison Composite Approach

Recall from Chapter 5 where the evaluation of the hardness of the homogenized porous material depends on the yield criteria, and in turn, depends on the definition of the dissipation function, $\Pi_{hom}(D)$. The downscaling results present the solution of the dissipation function with an elliptical criterion using the second-order conic optimization. In the following section, the linear comparison composite (LCC) approach (Ortega et al., 2007) is presented to cater for a hyperbola solution, where the constant B within the dissipation function has either the value of $B = 0$ or $B < 0$. The LCC approach seeks to identify the minimum points (or known as stationary points) of the upper bound solution for the homogenized strain rate energy density function, expressed as:

$$\Pi_{hom}(D) = \underset{\mathcal{C}^i \ \tau^i}{\mathrm{stat}} \left\{ \Psi(D) + \sum_i f_i Y_i \right\}$$

$$(6.2.1)$$

where the $\Psi(D)$ is the homogenized composite strain rate energy. For an isotropic material, the strain rate energy can be expressed as (Lee et al., 2020):

$$\Pi_{hom}(D_v, D_d) = \frac{1}{2} k_{hom} D_v{}^2 + 2 g_{hom} D_d{}^2 + \beta(\tau_1 - \tau_2) D_v + \frac{\gamma(\tau_1 + \tau_2)^2}{2 g_1}$$

$$\text{where} \quad \beta = \frac{k_{hom} - k_2}{k_1 - k_2}; \quad \gamma = \frac{g_1}{k_1 - k_2}(\beta - f_1);$$

$$D_v = tr(D); \quad D_d = \sqrt{\frac{1}{2}\Delta : \Delta} \quad \text{with} \quad \Delta = D - tr(D)1$$

$$(6.2.2)$$

The adopted upscaling methodology is based on the strength homogenisation approach (Dormieux et al., 2006, 2017) for a material system of self-consistent, perfectly disordered, granular solid-

porous particles (see Chapter 5). The strength of the heterogeneous material system is obtained using the Drucker-Prager yield criterion, where σ_m is the mean stress, σ_d is the deviatoric stress, α_s is the friction angle, and c_s is the cohesion. The subscript s represents the solid where the stresses are originated from.

$$F(\sigma) = \sigma_d + \alpha_s\,\sigma_m - c_s \leq 0 \qquad (6.2.3)$$

Alternatively, the Drucker-Prager yield criterion can be expressed in an equivalent form of hyperbolas (Bobko et al., 2011, Ortega et al., 2007) where the scalars A, B and S_0 can be used to relate the yield criterion parameters.

$$F(\sigma) = 1 - \frac{(\sigma_m - S_0)^2}{A} + \frac{\sigma_d}{B} \leq 0$$

$$\alpha = \sqrt{\frac{B}{A}}; \qquad c_s = S_0\,\alpha_s \qquad (6.2.4)$$

It has been shown by Ortega et al. (2011) that the ratio of A and B can be related to the bulk modulus (k) and shear modulus (g) and the friction angle (α). It should be noted that these relationships are universal across different scale lengths due to the assumption that the Drucker-Prager yield criterion remains valid. For this reason, the subscript s has been dropped in the friction angle. The same holds true to the k, g, A, and B where they are no longer constraint to a particular length scale.

$$\frac{k}{g} = \frac{A}{B} = \frac{1}{\alpha^2} \qquad (6.2.5)$$

The nonlinearity function (Y_i) related to the Drucker-Prager condition for each phase can be expressed as:

$$Y_i = \frac{B_i}{2g_i}\left[\frac{(S_i - \tau_i)^2}{2A_i} - 1\right] \qquad \text{where} \quad i = 1, 2 \qquad (6.2.6)$$

Stationarity points in the homogenised strain rate energy density function (Π_{hom}) can be found by differentiating it against the value of the prestress (τ_i) and the shear modulus (g_i).

$$\frac{\partial \Pi_{hom}}{\partial g_i} = 0; \qquad \frac{\partial \Pi_{hom}}{\partial \tau_i} = 0 \qquad (6.2.7)$$

Solving Equation 6.2.7 will yield the prestress (τ_i) and the shear modulus (g_i). By substituting these back into Π_{hom} in Equation 6.2.2, an alternative form of Π_{hom} can be expressed as:

$$\Pi_{hom} = D_v S_{hom} - sign(2B_{hom}\mathcal{K} - \eta A)\sqrt{4B_{hom}D_d{}^2 + A_{hom}D_v{}^2} \qquad (6.2.8)$$

The corresponding yield criterion can be expressed in terms of the scalar constants, where Σ_m and Σ_d represent the composite solid-porosity phase mean stress and deviatoric stress,

respectively.

$$F\left(\Sigma_m, \Sigma_d\right) = sign(B_{hom}) \left[\frac{\Sigma_d^2}{B_{hom}} + \frac{S_{hom} - \Sigma_m^2}{A_{hom}} - 1 \right] \qquad (6.2.9)$$

Equation 6.2.8 can be used to determine the values of the homogenized scalars A_{hom}, B_{hom} and S_{hom} so that the Drucker-Prager yield criterion shape can be determined. The definition of the scalar constant would depend on the morphology combination at a specific scale level (denoted by I as level 1 and II as level 2), whether it is solid-pores, solid-solid or solid-rigid. It is noted here that once the scalar constant is known, i.e. the yield criterion is defined, the conventional mechanical properties related to the yield criterion can then be determined as:

$$\alpha_{hom}^{(i)} = \sqrt{-sign(\rho_{hom}^{(i)}) \frac{B_{hom}^{(i)}}{A_{hom}^{(i)}}}; \qquad c_{hom}^{(i)} = \sqrt{\frac{B_{hom}^{(i)}(A_{hom}^{(i)} - S_{hom}^{(i)})^2}{A_{hom}^{(i)}}} \qquad (6.2.10)$$

$$\text{where} \quad i = \text{I (Level 1), II (Level 2)}$$

The bond strength can be theoretically derived based on the result of the yield criterion by modelling the coating under sustained tension load. The tensile strength relationship with the scaling constants can be expressed as:

$$\Sigma_{tensile} = \frac{3B_{hom} \left(S_{hom} - A_{hom} \sqrt{\frac{-3S_{hom}^2 + 3A_{hom} + B_{hom}}{A_{hom}B_{hom}}} \right)}{3A_{hom} + B_{hom}} \qquad (6.2.11)$$

The homogenization process can be carried out with three different composite combinations, outlined in the following:

6.2.1   Solid-Pore Composite

A solid-Pore composite is created with a solid and a pore phase is homogenized. The Drucker-Prager yield criterion scalar constants for a solid-pores composite can be expressed as

$$
\begin{aligned}
S_{hom}^{(1a)} &= -\frac{\mathcal{K}\alpha_i c_i f_i}{f_i - 2\mathcal{K}\alpha_i^2} \\
A_{hom}^{(1a)} &= \frac{\mathcal{K}c_i^2 f_i^2 (f_i - \mathcal{K}\alpha_i^2)}{f_i - 2\mathcal{K}\alpha_i^2} \\
B_{hom}^{(1a)} &= \frac{Mc_i^2 f_i (f_i - \mathcal{K}\alpha_i^2)}{f_i - 2\mathcal{K}\alpha_i^2}
\end{aligned}
\qquad (6.2.12)
$$

where the subscript i denotes the solid phase, and the f_i is the volume fraction of the solid. Similarly, the mechanical properties for a homogenized solid-pores composite can be determined from

$$\alpha_{hom}^{(1a)} = \sqrt{-sign(\rho_{hom}^{(1a)})\frac{B_{hom}^{(1a)}}{A_{hom}^{(1a)}}}; \qquad c_{hom}^{(1a)} = \sqrt{\frac{B_{hom}^{(1a)}(A_{hom}^{(1a)} - S_{hom}^{(1a)})^2}{A_{hom}^{(1a)}}} \qquad (6.2.13)$$

6.2.2 Solid-Solid Composite

A solid-solid composite is formed by two solid phases. Similarly, the Drucker-Prager yield criterion scalar constants for a solid-solid composite, which is represented by phase i and phase j, can be derived as (Lee et al., 2020):

$$
\begin{aligned}
\xi &= r_g \alpha_i{}^2 \alpha_j{}^2 f_i - r_g \alpha_i{}^2 \alpha_j{}^2 f_i{}^2 + 2\gamma_{hom}\alpha_i{}^2 f_i - 2\gamma_{hom}r_g\alpha_j{}^2 f_i + 2\gamma_{hom}r_g\alpha_j{}^2 \\
\zeta &= \alpha_i\alpha_j\beta_{hom}r_g f_i(\alpha_i c_j - \alpha_j c_i)(f_i - 1) \\
\omega &= f_i\gamma_{hom}r_g(\alpha_i c_j - \alpha_j c_i)^2(f_i - 1) \\
\kappa &= \mathcal{K}r_g\alpha_i{}^2\alpha_j{}^2 f_i{}^2 - \mathcal{K}r_g\alpha_i{}^2\alpha_j{}^2 f_i + 2\alpha_i{}^2\beta_{hom}f_i - 2\mathcal{K}\beta_{hom}\alpha_i{}^2 f_i \\
&\quad - 2r_g\alpha_j{}^2\beta_{hom}f_i + 2r_g\alpha_j{}^2 \\
S_{hom}^{(1b)} &= -\frac{\zeta}{\xi}; \qquad A_{hom}^{(1b)} = \frac{\kappa\omega}{\xi^2}; \qquad B_{hom}^{1b)} = \frac{-\mathcal{M}\omega}{\zeta}; \qquad \rho_{hom}^{(1b)} = \frac{\omega}{\xi}
\end{aligned}
\qquad (6.2.14)
$$

And similarly, the mechanical properties can be expressed as:

$$\alpha_{hom}^{(1b)} = \sqrt{-sign(\rho_{hom}^{(1b)})\frac{B_{hom}^{(1b)}}{A_{hom}^{(1b)}}}; \qquad c_{hom}^{(1b)} = \sqrt{\frac{B_{hom}^{(1b)}(A_{hom}^{(1b)} - S_{hom}^{(1b)})^2}{A_{hom}^{(1b)}}} \qquad (6.2.15)$$

6.2.3 Solid-Rigid Composite

A solid-rigid composite has one of the solid phase that is treated as rigid. In terms of continuum mechanics, the rigid phase is considered non-compressible. The Drucker-Prager yield criterion scalar constants for such a solid-rigid composite can be expressed as

$$
\begin{aligned}
S_{hom}^{(2b)} &= S_i \\
A_{hom}^{(2b)} &= 2A_i - A_i\mathcal{K}\alpha_i{}^2 f_i \\
B_{hom}^{(2b)} &= -\mathcal{M}\alpha_i{}^2 f_i
\end{aligned}
\qquad (6.2.16)
$$

And similarly, the mechanical properties can be expressed as:

$$\alpha_{hom}^{(2b)} = \sqrt{-sign(\rho_{hom}^{(2b)})\frac{B_{hom}^{(2b)}}{A_{hom}^{(2b)}}}; \qquad c_{hom}^{(2b)} = \sqrt{\frac{B_{hom}^{(2b)}(A_{hom}^{(2b)} - S_{hom}^{(2b)})^2}{A_{hom}^{(2b)}}} \qquad (6.2.17)$$

6.3 Multiscaling Model

A multiscaling model is built based on the hybrid aluminum and zinc coating. The model consists of three scale lengths, which includes nanoscale (level 0), microscale (level 1) and mesoscale/macroscale (level 2). As illustrated in Figure 6.1, the experimental nanoindentation tests are carried out at the microscale (level 1), while the bond strength tests are carried out at the macroscale (level 2). The mesoscale porosity is determined from the EDS image as detailed in section 3.6. This porosity is adopted to derive the hybrid porous coating mechanical properties.
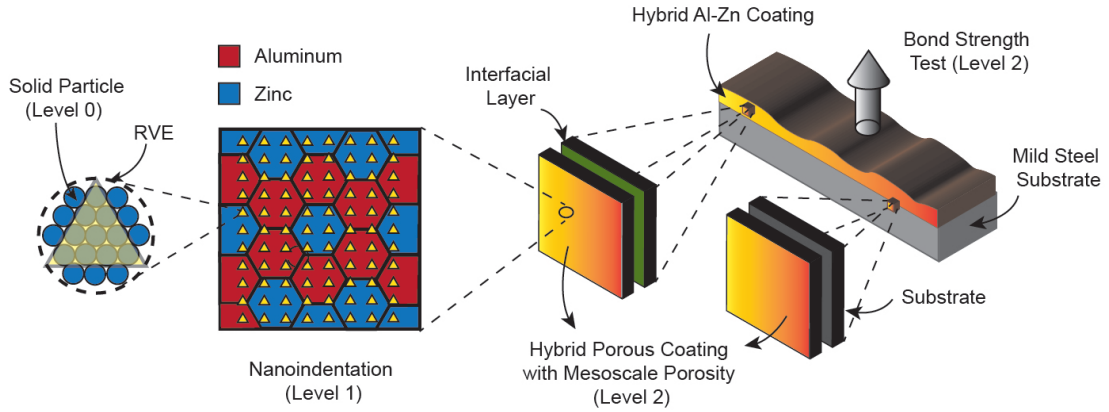
Figure 6.1: Multiscaling model for hybrid aluminum and zinc coating

A multiscaling (upscaling) algorithm is implemented to investigate the coating properties, and the procedure is shown in Figure 6.2. The building block of the upscaling algorithm is a single material phase, which can be either a solid or a pore. A composite can be created by either combining a solid with solid or solid with pore. The process of combining two phases is known as homogenization. The composite resulted from the homogenization process can be one of the three combinations, i.e. solid-pore, solid-solid and solid-rigid. The corresponding mechanical properties for the respective composite combination can be derived by one of the equations, either 6.2.10, 6.2.13 or 6.2.15,

The multiscaling model consider two scenarios to investigate the coating failure mode at the macroscale level (level 2). The first scenario (Level 2b-1) is a debonding case where the coating is separated from the substrate. The separation is modelled as failure at an arbitrary interface layer. The mechanical properties of the interfacial layer is back calculated based on the actual experimental average bond strength. The second scenario (Level 2b-2) consider the effect of substrate as a rigid entity where debonding is not allowed. As a result, the failure will happen within the coating body itself since the substrate (carbon steel) is much stronger compared to the coating.
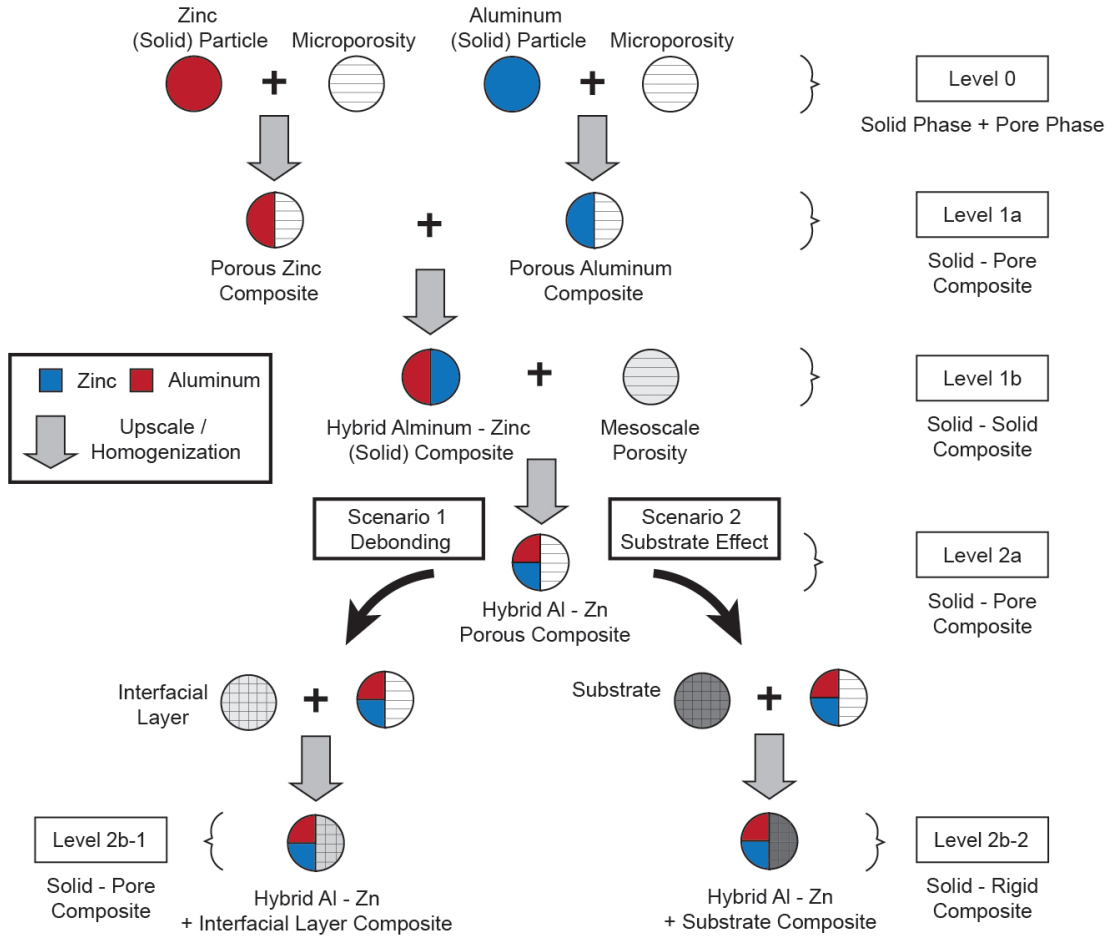
Figure 6.2: Multiscaling procedure for each scale lengths

6.4 LCC-based Minimization Problem

The upscaling algorithm starts with the mechanical properties for the solid phase at the nanoscale level (level 0). These properties can be derived by performing a downscaling exercise based on the nanoindentation test results. The downscaling exercise is similar to the downscaling algorithm described in Chapter 5, but this time it is based on the LCC approach. The difference between the previous downscaling algorithm to the LCC-based downscaling approach is the definition of hardness. Recall from Chapter 5 that downscaling can be carried out using the dimensionless scaling functions corresponding to the indentation modulus and hardness (refer to Equation 5.7.1). While the same indentation modulus related dimensionless scaling function can be used, the hardness related dimensionless scaling function is derived using the linear comparison composite (LCC) theory (Bobko et al., 2011, Ortega et al., 2007), which is shown in Equation 6.4.1. It is noted that the hardness related dimensionless scaling function based on the LCC approach uses the Mori-Tanaka scheme instead of the self-consistent scheme adopted previously. In this case, the solid percolation threshold, $\eta_0 = 0$.

$$H_{hom} = h_s(c_s, \alpha_s) \cdot \Pi_H(\alpha_s, \eta, \eta_0 = 0)$$

$$where \quad h_s = c_s[a(1 + b\alpha_s + (c\alpha_s)^3 + (d\alpha_s)^{10})]$$

$$a = 1.7644; \qquad b = 2.5934;$$

$$c = 2.1860; \qquad d = 1.6777$$

(6.4.1)

$$\Pi_H(\alpha_s, \eta) = \pi_1(\eta, \eta_0) + \alpha_s(1 - \eta)\Pi_2(\alpha_s, \eta, \eta_0)$$

$$where \quad \Pi_1 = \eta[1 + g(1 - \eta) + h(1 - \eta)^2 + j(1 - \eta)\eta^3]$$

$$\Pi_2 = \alpha_s\eta^2[k + m(1 - \eta) + p(1 - \eta)\alpha_s + q\alpha_s^3]$$

$$g = -1.2078; \qquad k = 8.7145; \qquad p = 74.0617;$$

$$h = 0.4907; \qquad m = -40.6615; \qquad q = -64.094; \qquad j = -1.7257$$

(6.4.2)

Based on the nanoindentation test results where the measured indentation modulus and hardness are known for all the locations, the theoretical indentation modulus and hardness can be determined by minimizing the difference from the experimental values. The minimizing process can be expressed as a minimization problem expressed as Equation 6.4.3. The minimisation problem is further modified to include the weighting factors for the indentation modulus and hardness, respectively (M_0, H_0).

$$\min_{\substack{c_s, \alpha_s, \eta, \\ M_{0(J)}, H_{0(J)}}} \sum_{i,j=1}^{N} \left[\frac{\left(M_{i(J)} - M_{hom(J)}\right)^2}{M_{0(J)}} + \frac{\left(H_{i(J)} - H_{hom(J)}\right)^2}{H_{0(J)}} \right] \quad where \quad J \in 1,3 \quad (6.4.3)$$

6.5 Results and Discussion

6.5.1 Level 1a

The upscaling algorithm starts where the individual solid phase for aluminum and zinc is made known by solving the minimization given in Equation 6.4.3. Both the dimensionless scaling functions for elastic modulus and hardness are obtained to derive the solid properties and packing density. The corresponding microporosity on each indentation location can be determined and shown in Figure 6.3. Similar to the hardness-packing density plots (see Figure 5.8) defined using the elliptical yield domain, the hardness was found to have a non-linear relationship using the LCC approach. The mechanical properties of the homogenized solid-pore composite for the aluminum and zinc are presented in Table 6.1.

6.5.2 Level 1b

The next step is to homogenize aluminum and zinc solid-pore composite into a hybrid solid-solid composite by using Equation 6.2.7. The results are presented in Table 6.2. This hybrid composite will be treated as the microscale solid phase for the next upscaling step.

Table 6.1: Level 1a: Mechanical properties of the aluminum and zinc (solid-pore) composite

Phase	Properties	Longitudinal (x_1 or x_2)	Transverse (x_3)
Aluminum	k_{hom} (GPa)	0.0040	0.0174
	g_{hom} (GPa)	0.0012	0.0041
	S_{hom} (GPa)	-0.0365	-0.0923
	Friction Angle, α_{hom} (Rad)	0.5477	0.4852
	Cohesion, c_{hom} (GPa)	0.0222	0.0532
Zinc	k_{hom} (GPa)	0.0118	0.0053
	g_{hom} (GPa)	0.0039	0.0017
	S_{hom} (GPa)	-0.0631	-0.0417
	Friction Angle, α_{hom} (Rad)	0.5753	0.5621
	Cohesion, c_{hom} (GPa)	0.0431	0.0265

Table 6.2: Level 1b: Mechanical Properties of the hybrid Al-Zn (solid-solid) composite

Phase	Properties	Longitudinal (x_1 or x_2)	Transverse (x_3)
Hybrid Aluminum-Zinc	k_{hom} (GPa)	0.0015	0.0110
	g_{hom} (GPa)	0.00014	0.00018
	S_{hom} (GPa)	0.0264	-0.0163
	Friction Angle, α_{hom} (Rad)	0.3069	0.4033
	Cohesion, c_{hom} (GPa)	0.0081	-0.0066

6.5.3   Level 2a

Once the level 1 properties are finalised, the next step is to upscale to level 2 by incorporating the mesoscale porosity. Mesoscale porosity has been mentioned in the previous section as 18%. Based on this ratio, the mesoscale porous solid composite can then be determined using the Equation 6.2.6. Figure 6.4 shows the changes in tensile strength with a decreasing porosity. The results of the mesoscale mechanical properties are presented in Table 6.2. The theoretical tensile strength at the mesoscale is determined as 11.8 MPa using the Equation 6.2.14. Compared to the experimental average bond strength of 3.93 MPa, this theoretical tensile strength is much higher. It can be noted that the theoretical tensile strength is the estimated strength of the porous solid coating material itself for the specific 18% porosity. Hence the lower experimental bond strength can only be explained in two ways. The first explanation is that the location that has the tested bond strength corresponds to a porosity lower than 18%. This explanation is illustrated in Figure 6.3, where the porosity is shown to affect the tensile strength, i.e., the higher the porosity, the lower the tensile strength. For a tensile strength of 3.93 MPa, the corresponding porosity would be 68%. Such high porosity would not be possible, and hence it leads to the second explanation where the failure does not occur within the porous solid coating but at the coating-substrate interface.

Table 6.3: Level 2a: Mechanical properties of the hybrid coating (solid-pores) composite

Phase	Properties	Longitudinal (x_1 or x_2)	Transverse (x_3)
Solid-Pores Hybrid Aluminum-Zinc	k_{hom} (GPa)	6.998×10^{-4}	0.0031
	g_{hom} (GPa)	5.133×10^{-5}	8.208×10^{-5}
	S_{hom} (GPa)	0.0155	-0.0404
	Friction Angle, α_{hom} (Rad)	0.2708	0.1631
	Cohesion, c_{hom} (GPa)	0.0042	-0.0066
	Tensile Strength (MPa)		11.8

6.5.4 Level 2b-1

Existing literature had reported that an interfacial layer exists between the coating with the substrate where the coating tends to fail in debonding or delamination under the effect of this residual stress (Besmann, 2009, Clyne and Gill, 1996, Greving, 1996, Yang and Chang, 2001). The accumulation of residual stresses are the result of the cooling and impact mechanism of the coating when it deposited itself on the relatively rigid substrate (Davis et al., 2004). The extent of the residual stresses depends on the substrate surface roughness (Benedetti et al., 2009) and the spraying parameters (Greving, 1996). The interfacial layer between the coating and the substrate can be modelled using the homogenization approach as a solid-solid composite with the weaker interfacial layer treated as the matrix. Using the experimental bond strength as input, the mechanical properties of the composite with a weak matrix and the corresponding volume fraction can be determined. The interfacial layer mechanical properties, denoted by the subscript IFL, is presented in Table 6.4. The interfacial layer was found to have a volume fraction of 8%. For a corresponding bond strength as low as 3.93 MPa, the mechanical properties of the homogenized hybrid coating with the interfacial layer is presented in Table 6.4.

Table 6.4: Level 2b-1: Mechanical properties of the hybrid coating with interfacial layer

Phase	Properties	Transverse (x_3)
Interfacial Layer	k_{IFL} (GPa)	0.0027
	g_{IFL} (GPa)	4.0225×10^{-5}
	Interfacial Layer volume fraction	8%
Homogenized Coating with Interfacial Layer	k_{hom} (GPa)	2.9042×10^{-4}
	g_{hom} (GPa)	6.1459×10^{-6}
	S_{hom} (GPa)	-0.0056
	Friction Angle, α_{hom} (Rad)	0.1455
	Cohesion, c_{hom} (GPa)	-8.0823×10^{-4}

6.5.5 Level 2b-2

In the event if debonding is not allowed to happen, the rigid substrate will have an effect on the bond strength of the coating. in other words, the failure is forced to failed within the coating body. In this case, the hybrid coating is treated as a single phase and homogenize with the rigid substrate as a solid-rigid composite. The coating and the rigid substrate is considered each taking 50% of the volume fraction. It is observed that the rigid substrate contribute to the bond strength which increased to 14.3 MPa. This tensile strength is higher compared to the theoretical hybrid porous coating determined at level 2b. This further confirms that debonding failure is the dominant failure mode for this coating.

Table 6.5: Level 2b-2 Mechanical properties of the hybrid coating on rigid substrate

Phase	Properties	Transverse (x_3)
Hybrid Coating on Rigid Substrate	k_{hom} (GPa)	0.0031
	g_{hom} (GPa)	1.4192×10^{-4}
	S_{hom} (GPa)	-0.0404
	Friction Angle, α_{hom} (Rad)	0.2126
	Cohesion, c_{hom} (GPa)	-0.0086
	Tensile Strength (MPa)	14.3
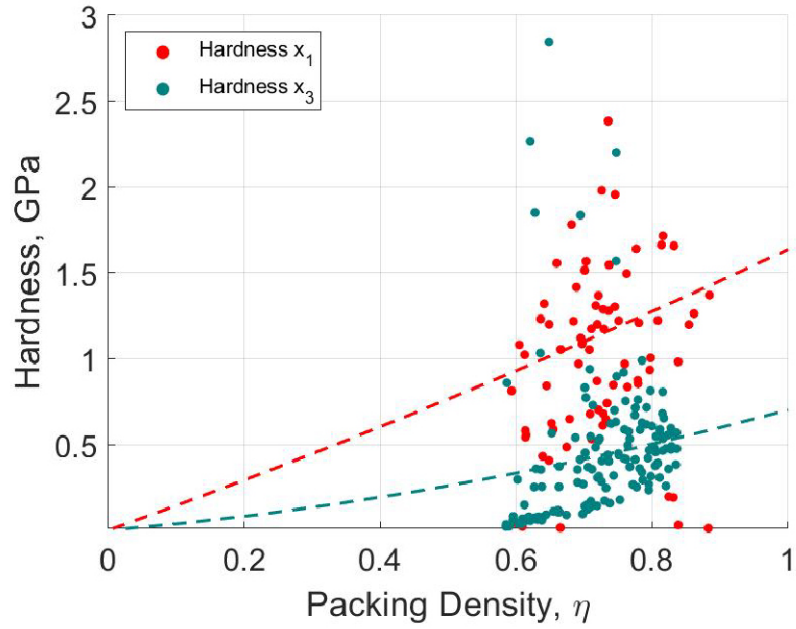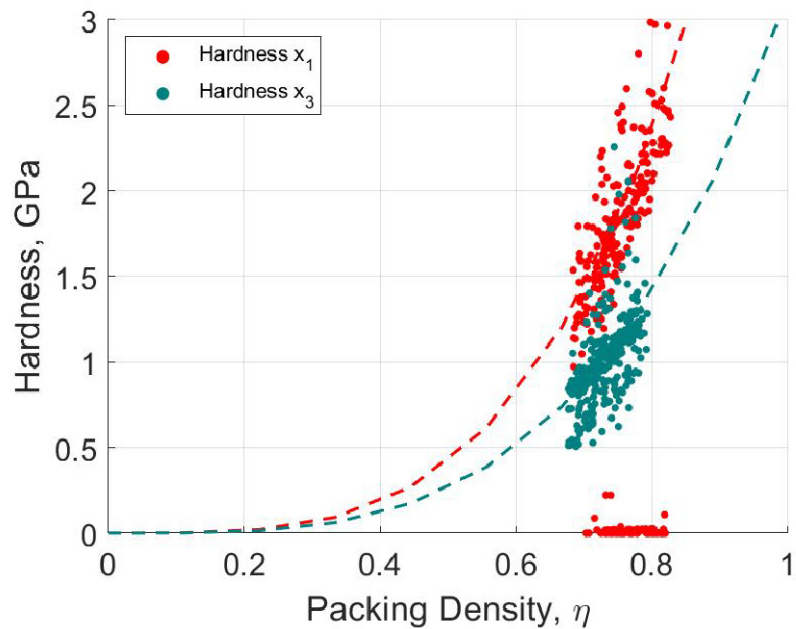
Figure 6.3: Scaling relationship of hardness with packing density (a) Aluminum (b) Zinc

Figure 6.4: Effect of porosity on the bond strength in the thermal arc sprayed Al-Zn coating

6.6   Summary and Conclusion

In this chapter, a multiscaling framework has been presented to derive the mechanical properties of the porous material at the mesoscale/macroscale based on experimental data. The material syst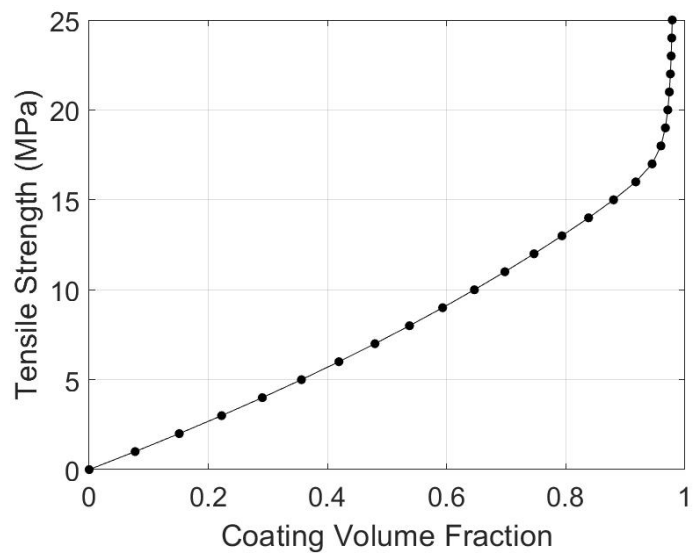em is built on the concept of a transversely isotropic and self-consistent model consists of both solid particles and pores, where the mechanical properties of the material system obeys the continuum mechanics and the micrporomechanical theory with the linear comparison composite approach. The overall mechanical properties of the material system is dependent on the inherent properties of the solid particles and the mechanical interaction against each other, where the latter is influenced by the pores space between the solid particles. The material system at each scale length has its distinct solid particles properties and the corresponding pore space which give rise to the overall mechanical behaviour. The multiscaling framework introduced in this chapter is capable of deriving the mechanical properties of the solid particles and the volume of the pore space by calibrating the experimental test results carried out at their corresponding scale length.

The thermal arc sprayed aluminum and zinc coating is chosen as the application. Nanoindentation test mechanical properties results provides the input data to calibrate the pores space at the microscale (level 1), or known as microporosity. At the mesoscale/macroscale level (level 2), the bond strength test results are used to derive the mechanical properties of the coating. The pore space at mesoscale, or known as mesoscale porosity, is pre-determined by measuring the pore space on the coating cross section image at a scale of 100 μm. The upscaling procedure generally involves a series of homogenization process combining multiple phases to create a composite material system. This is achieved by treating one phase as a matrix and the other as an include so that homogenization can be carried out using the LCC-based homogenization functions.

The following conclusions are obtained as a result of the upscaling algorithm:

1. At the microscale level (level 1), the individual aluminum and zinc phase is treated as two separate materials with each material modelled as a two-phase (solid and microporosity) composite. The mechanical behaviour of the two-phase (solid and microporosity) can be determined by solving the difference between the LCC theoretical result and the experimental nanoindentation results as a minimization problem. Similarly, the aluminum and zinc can be treated as two separate solid phases. They can be combined or homogenized to create a hybrid aluminum-zinc (solid-solid) composite. This hybrid composite is treated as the building block for the next upscaling procedure into the mesoscale.

2. At the mesoscale/macroscale level, the hybrid coating is treated as a porous composite after combining the pre-determined mesoscale porosity (18%) with the hybrid building block from the microscale level. The tensile strength from this composite reveals is relatively high (11.8 MPa) when compared to the experimental macroscale bond strength average results (3.93 MPa). The mismatch of in the tensile strength is reveals that failure did not occur at the coating body, but instead at the interface of the coating on the substrate. In other words, the coating is failed in debonding rather than structural failure.

3. By assuming the substrate as a rigid entity, a interfacial layer can be modelled with the coating as a two phase material system. The mechanical properties of the interfacial

layer (ITL) can be back calculated by adopting a tensile strength of 3.93 MPa for the homogenized (coating-ITL) composite. The results reveals that the interfacial layer has a 8% volume fraction. IN the scenario where debonding is not allowed, the coating is modelled as a solid-rigid composite by incorporating the effect from a rigid substrate. The results shows that a rigid substrate contribute to an increased in the bond strength to 5.3 MPa. Therefore, it is concluded that debonding remains as the dominant failure mode with a lower debonding strength of 3.93 MPa as captured from the experimental bond test.

Summary

This PhD work is part of a collective effort to seek an answer to a fundamental engineering question: What is the origin of the mechanical behaviour for a material system? Instead of relying on the conventional macroscale testing, this work adopts an alternative approach by going down the path of investigation at a smaller scale length. The main feature of this research outcome is the introduction of a multiscale framework that can link the experimental results at multiple scale lengths to a theoretical microporomechanical material model. The research goes on to show that the mechanical properties can be theoretically linked to the pores at the specific scale length. In other words, the variation in mechanical properties observed is due to the different volumetric packing of the solid particles, and the mechanical properties of the solid material should not change. Hence, finding the mechanical properties of the solid particle down the scale could potentially lead to the origin of mechanical behaviour.

The following is the summary of the outcome and achievement from this thesis in response to the proposed research aim and objective

- ■ Nanoindentation Measurement and Outcome

  - The theoretical background of nanoindentation has been given in Chapter 2. The limitation in the conventional solution for nanoindentation measurement including the indentation impression has been discussed. In particular, the concept of continuous stiffness measurement (CSM) method has been introduced. In Chapter 3, the nanoindentation measurement for the thermal sprayed aluminum and zinc coating has been presented using the statistical deconvolution analysis.

  - The computational assisted indentation approach based on the CSM method is a novelty introduced in Chapter 4 of this thesis. The stiffness-based reverse algorithm is proposed to address the indentation geometrical impression limitation highlighted in Chapter 1. Chapter 2, 3 and 4 focus in presenting the nanoindentation as an investigative tool. This next two chapters then focus in applying nanoindentation result in the multiscaling analysis.

- ■ Microporomechanical Analytical Solution

  - Chapter 5 and Chapter 6 outline the multiscaling analysis framework using nanoindentation as input data. The theoretical background for the microporomechanical framework has been introduced in Chapter 5. The novelty is the incorporation of the computational assisted indentation approach into the downscaling algorithm. This

outcome of this downscaling algorithm shows good correlation of the nanoscale properties when compared to the molecular dynamics result reported in the literature.

■ Application on Thermal Sprayed Aluminum and Zinc Coating

- The statistical deconvolution method highlighted in Chapter 3 is able to access the individual aluminum and zinc phase within the composite coating. The computational assisted indentation approach presented in Chapter 4 has been shown to provide estimation of the plasticity properties for the individual phases in the coating. It is shown in this work that the porosity plays a vital role in deriving the mechanical response at the different scale length.

- The main discovery from this work is the derivation of the anisotropic mechanical properties based on the microporomechanical framework. It was found that this outcome correlate well with existing literature. More importantly, this work provides evidence that the anisotrophy is a dominantly affected by plastic deformation in the coating during the spraying process. This discovery presents a new perspective in the conventional coating anisotrophy phenomenon where mainly elasticity behaviour is reported in the literature.

- The upscaling algorithm presented in Chapter 6 shows that the bond test result at the macro scale can be replicated using the multiscaling approach. Similar to the downscaling algorithm, improvement has been made in the upscaling algorithm so that it can be used to apply on a wide ranger of materials. This work also provides the evidence to support the existence of an interfacial layer between the coating and the substrate, which is known in the literature as a cause of bonding failure in coating.

By using thermal sprayed coating as the application and nanoindentation as the primary investigation tool, this research shows how the material properties can be derived at the larger and smaller scale lengths. To the best of the author's knowledge, this is the first time the thermal sprayed aluminum and zinc composite coating is treated as a cohesive-frictional solid material. The downscaling algorithm can be used to derive the aluminum and zinc nanoscale properties that are similar to the outcome of a molecular dynamics simulation. The same happens when the coating bond strength result can be replicated using the nanoindentation results. What this achievement implies is that there is evidence that mechanical behaviour in a material system can be inter-related across different scale lengths. In other words, the origin of mechanical properties can be traced downwards to a microscopic scale.

However, the next question is: How small can we go? This question would lead to the potential future works that this research inspired. From the "investigation tool" perspective, as the current investigative technology development advances, we can expect new tools introduced to access the mechanical properties of a solid particle at a smaller scale compared to the nanoindentation. However, there is a limit where mechanical properties can be physically measured as the investigation goes down an ever-smaller scale. Therefore, it is logical to imply that future works may have to go beyond the realm of solid mechanics to look for answer.

References

Every reasonable effort has been made to acknowledge the owners of copyright material. I would be pleased to hear from any copyright owner who has been omitted or incorrectly acknowledged.

A. Anandarajah. *Computational methods in elasticity and plasticity: solids and porous media.* Springer Science & Business Media, 2011.

A. S. M. Ang and C. C. Berndt. A review of testing methods for thermal spray coatings. *International materials reviews*, 59(4):179–223, 2014.

ANSYS Academic Research Mechanical APDL, Release 18.1. ANSYS, 2019.

E.-. ASTM et al. Standard test methods for tension testing of metallic materials. *Annual book of ASTM standards. ASTM*, 2001.

M. Benedetti, V. Fontanari, P. Scardi, C. A. Ricardo, and M. Bandini. Reverse bending fatigue of shot peened 7075-t651 aluminium alloy: The role of residual stress relaxation. *International Journal of Fatigue*, 31(8-9):1225–1236, 2009.

T. M. Besmann. Interface science of thermal barrier coatings. *Journal of Materials Science*, 44(7):1661–1663, 2009.

C. P. Bobko, B. Gathier, J. A. Ortega, F.-J. Ulm, L. Borges, and Y. N. Abousleiman. The nanogranular origin of friction and cohesion in shale—a strength homogenization approach to interpretation of nanoindentation results. *International Journal for Numerical and Analytical Methods in Geomechanics*, 35(17):1854–1876, 2011.

A. Bolshakov and G. Pharr. Influences of pileup on the measurement of mechanical properties by load and depth sensing indentation techniques. *Journal of materials research*, 13(4):1049–1058, 1998.

A. Bolshakov, W. Oliver, and G. Pharr. Influences of stress on the measurement of mechanical properties using nanoindentation: Part ii. finite element simulations. *Journal of Materials Research*, 11(3):760–768, 1996.

J. Brinell. Congrès international des méthodes d'essai des matériaux de construction. *Paris*, 2:83–94, 1901.

H. Buckle. The science of hardness testing and its research applications. *Westbrook, Jack Hall*, 1973.

S. Cariou, F.-J. Ulm, and L. Dormieux. Hardness–packing density scaling relations for cohesive-frictional porous materials. *Journal of the Mechanics and Physics of Solids*, 56(3):924–952, 2008.

S. Chen, L. Liu, and T. Wang. Investigation of the mechanical properties of thin films by nanoindentation, considering the effects of thickness and different coating–substrate combinations. *Surface and Coatings Technology*, 191(1):25–32, 2005.

Y.-T. Cheng and C.-M. Cheng. Relationships between hardness, elastic modulus, and the work of indentation. *Applied physics letters*, 73(5):614–616, 1998.

Y.-T. Cheng and C.-M. Cheng. Scaling, dimensional analysis, and indentation measurements. *Materials Science and Engineering: R: Reports*, 44(4-5):91–149, 2004.

Y.-T. Cheng, Z. Li, and C.-M. Cheng. Scaling relationships for indentation measurements. *Philosophical Magazine A*, 82(10):1821–1829, 2002.

K. Choudhary, T. Liang, A. Chernatynskiy, Z. Lu, A. Goyal, S. R. Phillpot, and S. B. Sinnott. Charge optimized many-body potential for aluminum. *Journal of Physics: Condensed Matter*, 27(1):015003, 2014.

T. Clyne and S. Gill. Residual stresses in thermal spray coatings and their effect on interfacial adhesion: a review of recent work. *Journal of Thermal Spray Technology*, 5(4):401, 1996.

G. Constantinides, K. R. Chandran, F.-J. Ulm, and K. Van Vliet. Grid indentation analysis of composite microstructure and mechanics: Principles and validation. *Materials Science and Engineering: A*, 430(1-2):189–202, 2006.

C.-L. Dai. In situ electrostatic microactuators for measuring the young's modulus of cmos thin films. *Journal of Micromechanics and Microengineering*, 13(5):563, 2003.

M. Dao, N. v. Chollacoop, K. Van Vliet, T. Venkatesh, and S. Suresh. Computational modeling of the forward and reverse problems in instrumented sharp indentation. *Acta materialia*, 49(19):3899–3918, 2001.

J. R. Davis et al. *Handbook of thermal spray technology*. ASM international, 2004.

A. Delafargue and F.-J. Ulm. Explicit approximations of the indentation modulus of elastically orthotropic solids for conical indenters. *International journal of solids and structures*, 41(26):7351–7360, 2004.

S. Deshpande and S. Sampath. 331 microstructure evolution in thermal spray coatings and its relevance in high temperature behavior. In *Proceedings of the 1992 Annual Meeting of JSME/MMD 2005*, pages 235–237. The Japan Society of Mechanical Engineers, 2005.

D. E. Dickel, M. I. Baskes, I. Aslam, and C. D. Barrett. New interatomic potential for mg–al–zn alloys with specific application to dilute mg-based alloys. *Modelling and Simulation in Materials Science and Engineering*, 26(4):045010, 2018.

M. F. Doerner and W. D. Nix. A method for interpreting the data from depth-sensing indentation instruments. *Journal of Materials research*, 1(4):601–609, 1986.

L. Dormieux, D. Kondo, and F.-J. Ulm. *Microporomechanics*. John Wiley & Sons, 2006.

L. Dormieux, E. Lemarchand, D. Kondo, and S. Brach. Strength criterion of porous media: Application of homogenization techniques. *Journal of Rock Mechanics and Geotechnical Engineering*, 9(1):62–73, 2017.

A. C. Fischer-Cripps. Nanoindentation test instruments. In *Nanoindentation*, pages 178–194. Springer, 2004.

A. C. Fischer-Cripps. Applications of nanoindentation. In *Nanoindentation*, pages 213–233. Springer, 2011.

D. J. Greving. Residual stresses and thermal spray coating performance. *PhD Thesis, The University of Tulsa*, 1996.

M. Grujicic, J. R. Saylor, D. E. Beasley, W. DeRosset, and D. Helfritch. Computational analysis of the interfacial bonding between feed-powder particles and the substrate in the cold-gas dynamic-spray process. *Applied Surface Science*, 219(3-4):211–227, 2003.

L. Guzman, M. Adami, W. Gissler, S. Klose, and S. De Rossi. Vapour deposited zn–cr alloy coatings for enhanced manufacturing and corrosion resistance of steel sheets. *Surface and Coatings Technology*, 125(1-3):218–222, 2000.

R. Haj-Ali, H.-K. Kim, S. W. Koh, A. Saxena, and R. Tummala. Nonlinear constitutive models from nanoindentation tests using artificial neural networks. *International Journal of Plasticity*, 24(3):371–396, 2008.

R. Hill. A theory of the yielding and plastic flow of anisotropic metals. *Proceedings of the Royal Society of London. Series A. Mathematical and Physical Sciences*, 193(1033):281–297, 1948.

R. Hill. Continuum micro-mechanics of elastoplastic polycrystals. *Journal of the Mechanics and Physics of Solids*, 13(2):89–101, 1965.

H. Huang and F. Spaepen. Tensile testing of free-standing cu, ag and al thin films and ag/cu multilayers. *Acta Materialia*, 48(12):3261–3269, 2000.

W. Y. Huen, H. Lee, V. Vimonsatit, P. Mendis, and H.-S. Lee. Nanomechanical properties of thermal arc sprayed coating using continuous stiffness measurement and artificial neural network. *Surface and Coatings Technology*, 366: 266–276, 2019.

W. Y. Huen, H. Lee, V. Vimonsatit, and P. Mendis. Relationship of stiffness-based indentation properties using continuous-stiffness-measurement method. *Materials*, 13(1):97, 2020.

H. M. Jaeger and S. R. Nagel. Physics of the granular state. *Science*, 255(5051): 1523–1531, 1992.

H.-S. Jang, K.-M. Kim, and B.-J. Lee. Modified embedded-atom method interatomic potentials for pure zn and mg-zn binary system. *Calphad*, 60:200–207, 2018.

W.-G. Jiang, J.-J. Su, and X.-Q. Feng. Effect of surface roughness on nanoindentation test of thin films. *Engineering Fracture Mechanics*, 75(17):4965–4972, 2008.

K. Johnson. Contact mechanics cambridge univ. *Press, Cambridge*, 95:365, 1985.

D. Joslin and W. C. Oliver. A new method for analyzing data from continuous depth-sensing microindentation tests. *Journal of Materials Research*, 5(1):123–126, 1990.

T. J. Kang, J.-G. Kim, H.-Y. Lee, J.-S. Lee, J.-H. Lee, J.-H. Hahn, and Y. H. Kim. Modification of optical and mechanical surface properties of sputter-deposited aluminum thin films through ion implantation. *International journal of precision engineering and manufacturing*, 15(5):889–894, 2014.

J.-Y. Kim, S.-K. Kang, J.-J. Lee, J.-i. Jang, Y.-H. Lee, and D. Kwon. Influence of surface-roughness on indentation size effect. *Acta materialia*, 55(10):3555–3562, 2007.

KSF4716. *Cement filling compound for surface preparation*. Seoul, Korea, 2001.

H. Lee, V. Vimonsatit, W. Y. Huen, P. Mendis, and K. S. K. Baduge. Cohesive-strength homogenisation model of porous and non-porous materials using linear comparison composites and application. *Scientific Reports*, 10(1):1–11, 2020.

H.-S. Lee, S.-J. Kwon, J. K. Singh, and M. A. Ismail. Influence of zn and mg alloying on the corrosion resistance properties of al coating applied by arc thermal spray process in simulated weather solution. *Acta Metallurgica Sinica (English Letters)*, 31(6):591–603, 2018.

Y. Li, J. Mueller, H. Höppel, M. Göken, and W. Blum. Deformation kinetics of nanocrystalline nickel. *Acta materialia*, 55(17):5708–5717, 2007.

Y. Lim, M. Chaudhri, and Y. Enomoto. Accurate determination of the mechanical properties of thin aluminum films deposited on sapphire flats using nanoindentations. *Journal of materials research*, 14(6):2314–2327, 1999.

J. LOUBET, J. GEORGES, O. MARCHESINI, and G. MEILLE. Vickers indentation curves of magnesium oxide (mgo). *Journal of lubrication technology*, 106 (1):43–48, 1984.

J. L. Loubet, J. M. Georges, and G. Meille. Vickers indentation curves of elastoplastic materials. In *Microindentation Techniques in Materials Science and Engineering*. ASTM International, 1985.

Z. Ma, Y. Zhou, S. Long, and C. Lu. An inverse approach for extracting elastic–plastic properties of thin films from small scale sharp indentation. *Journal of Materials Science & Technology*, 28(7):626–635, 2012a.

Z. Ma, Y. Zhou, S. Long, X. Zhong, and C. Lu. Characterization of stress-strain relationships of elastoplastic materials: An improved method with conical and pyramidal indenters. *Mechanics of Materials*, 54:113–123, 2012b.

Math, Statistics and Optimization Toolbox Release 2019a. The MathWorks, Inc, Natick, Massachusetts, United States., 2019.

R. McPherson. A review of microstructure and properties of plasma sprayed ceramic coatings. *Surface and Coatings Technology*, 39:173–181, 1989.

T. Mori and K. Tanaka. Average stress in matrix and average elastic energy of materials with misfitting inclusions. *Acta metallurgica*, 21(5):571–574, 1973.

A. Mosek. The mosek optimization toolbox for matlab manual, 2015.

T. Nakamura and Y. Gu. Identification of elastic–plastic anisotropic parameters using instrumented indentation and inverse analysis. *Mechanics of materials*, 39(4):340–356, 2007.

T. Nakamura, G. Qian, and C. C. Berndt. Effects of pores on mechanical properties of plasma-sprayed ceramic coatings. *Journal of the American Ceramic Society*, 83(3):578–584, 2000.

N. Ogasawara, N. Chiba, and X. Chen. Measuring the plastic properties of bulk materials by single indentation test. *Scripta Materialia*, 54(1):65–70, 2006.

W. C. Oliver and G. M. Pharr. An improved technique for determining hardness and elastic modulus using load and displacement sensing indentation experiments. *Journal of materials research*, 7(6):1564–1583, 1992.

W. C. Oliver and G. M. Pharr. Measurement of hardness and elastic modulus by instrumented indentation: Advances in understanding and refinements to methodology. *Journal of materials research*, 19(1):3–20, 2004.

G. Y. Onoda and E. G. Liniger. Random loose packings of uniform spheres and the dilatancy onset. *Physical review letters*, 64(22):2727, 1990.

J. A. Ortega, F.-J. Ulm, and Y. Abousleiman. The effect of the nanogranular nature of shale on their poroelastic behavior. *Acta Geotechnica*, 2(3):155–182, 2007.

J. A. Ortega, B. Gathier, and F.-J. Ulm. Homogenization of cohesive-frictional strength properties of porous composites: Linear comparison composite approach. *Journal of Nanomechanics and Micromechanics*, 1(1):11–23, 2011.

M. Pascuet and J. R. Fernández. Atomic interaction of the meam type for the study of intermetallics in the al–u alloy. *Journal of Nuclear Materials*, 467:229–239, 2015.

J. Pethica and W. Oliver. Tip surface interactions in stm and afm. *Physica Scripta*, 1987(T19A):61, 1987.

A. Reuss. Berechnung der fließgrenze von mischkristallen auf grund der plastizitätsbedingung für einkristalle. *ZAMM-Journal of Applied Mathematics and Mechanics/Zeitschrift für Angewandte Mathematik und Mechanik*, 9(1):49–58, 1929.

F. Römer, S. Braun, and T. Kraska. Development of an eam potential for zinc and its application to the growth of nanoparticles. *Physical Chemistry Chemical Physics*, 11(20):4039–4050, 2009.

G. Sachs. The derivations of the conditions of plasticity. *Ztsch. ver, deut. Ing*, 72:734, 1928.

R. Saha and W. D. Nix. Effects of the substrate on the determination of thin film mechanical properties by nanoindentation. *Acta materialia*, 50(1):23–38, 2002.

A. Selvadurai. The biot coefficient for a low permeability heterogeneous limestone. *Continuum Mechanics and Thermodynamics*, 31(4):939–953, 2019.

Y. Shibutani and A. Koyama. Surface roughness effects on the displacement bursts observed in nanoindentation. *Journal of Materials Research*, 19(1):183–188, 2004.

R. Sinha, C. J. Paredis, V.-C. Liang, and P. K. Khosla. Modeling and simulation methods for design of engineering systems. *J. Comput. Inf. Sci. Eng.*, 1(1): 84–91, 2001.

S. Sloan and P. Kleeman. Upper bound limit analysis using discontinuous velocity fields. *Computer methods in applied mechanics and engineering*, 127(1-4):293–314, 1995.

I. N. Sneddon. The relation between load and penetration in the axisymmetric boussinesq problem for a punch of arbitrary profile. *International journal of engineering science*, 3(1):47–57, 1965.

M. R. Stoudt, L. E. Levine, A. Creuziger, and J. B. Hubbard. The fundamental relationships between grain orientation, deformation-induced surface roughness and strain localization in an aluminum alloy. *Materials Science and Engineering: A*, 530:107–116, 2011.

G. Sundararajan, N. M. Chavan, and S. Kumar. The elastic modulus of cold spray coatings: influence of inter-splat boundary cracking. *Journal of thermal spray technology*, 22(8):1348–1357, 2013.

D. Tabor. A simple theory of static and dynamic hardness. *Proceedings of the Royal Society of London. Series A. Mathematical and Physical Sciences*, 192 (1029):247–274, 1948.

Y. Tan, A. Shyam, W. B. Choi, E. Lara-Curzio, and S. Sampath. Anisotropic elastic properties of thermal spray coatings determined via resonant ultrasound spectroscopy. *Acta materialia*, 58(16):5305–5315, 2010.

C. Tang, K.-C. Toh, and K.-K. Phoon. Axisymmetric lower-bound limit analysis using finite elements and second-order cone programming. *Journal of Engineering Mechanics*, 140(2):268–278, 2014.

S. L. Toma, M. Badescu, I. Ionita, M. Ciocoiu, and L. Eva. Influence of the spraying distance and jet temperature on the porosity and adhesion of the ti depositions, obtained by thermal spraying in electric arc-thermal activated. In *Applied Mechanics and Materials*, volume 657, pages 296–300. Trans Tech Publ, 2014.

F.-J. Ulm, M. Vandamme, C. Bobko, J. Alberto Ortega, K. Tai, and C. Ortiz. Statistical indentation techniques for hydrated nanocomposites: concrete, bone, and shale. *Journal of the American Ceramic Society*, 90(9):2677–2692, 2007.

T. Van Steenkiste, J. Smith, and R. Teets. Aluminum coatings via kinetic spray with relatively large powder particles. *Surface and Coatings Technology*, 154 (2-3):237–252, 2002.

D. Varacelle, D. Zeek, V. Zanchuck, E. Sampson, K. Couch, D. Benson, and G. Cox. Experimental studies of twin-wire electric arc sprayed zinc/aluminum alloy coatings. *Journal of Thermal Spray Technology*, 7(4):513–520, 1998.

J. J. Vlassak and W. Nix. Measuring the elastic properties of anisotropic materials by means of indentation experiments. *Journal of the Mechanics and Physics of Solids*, 42(8):1223–1245, 1994.

W. Voigt. Ueber die beziehung zwischen den beiden elasticitätsconstanten isotroper körper. *Annalen der physik*, 274(12):573–587, 1889.

W. Voigt et al. *Lehrbuch der kristallphysik*, volume 962. Teubner Leipzig, 1928.

L. Wang and S. Rokhlin. Universal scaling functions for continuous stiffness nanoindentation with sharp indenters. *International Journal of Solids and Structures*, 42(13):3807–3832, 2005.

L. Wang, M. Ganor, and S. Rokhlin. Inverse scaling functions in nanoindentation with sharp indenters: Determination of material properties. *Journal of Materials Research*, 20(4):987–1001, 2005.

Q. Wang, N. Birbilis, H. Huang, and M.-X. Zhang. Microstructure characterization and nanomechanics of cold-sprayed pure al and al-al2o3 composite coatings. *Surface and Coatings Technology*, 232:216–223, 2013.

T. Wang, T. Zhu, J. Sun, R. Wu, and M. Zhang. Influence of rolling directions on microstructure, mechanical properties and anisotropy of mg-5li-1al-0.5 y alloy. *Journal of Magnesium and Alloys*, 3(4):345–351, 2015.

Y.-C. Yang and E. Chang. Influence of residual stress on bonding strength and fracture of plasma-sprayed hydroxyapatite coatings on ti–6al–4v substrate. *Biomaterials*, 22(13):1827–1836, 2001.

A. Yurkov, V. Skvortsov, I. Buyanovsky, and R. Matvievsky. Sliding friction of diamond on steel, sapphire, alumina and fused silica with and without lubricants. *Journal of materials science letters*, 16(16):1370–1374, 1997.

A. Zaoui. Continuum micromechanics: survey. *Journal of Engineering Mechanics*, 128(8):808–816, 2002.

X. Zhang, B. Xu, F. Xuan, S. Tu, H. Wang, and Y. Wu. Porosity and effective mechanical properties of plasma-sprayed ni-based alloy coatings. *Applied Surface Science*, 255(8):4362–4371, 2009.

Appendix A

Design of Experiment - Isotropic Model

This appendix shows all the levels and parameters used as input to the computational simulation for the isotropic model. A total of 2496 combination are used based on this DOE.

Levels	Y/E	n	ν	θ
1	0.001	0	0.15	65.0
2	0.002	0.1	0.25	70.3
3	0.004	0.2	0.35	75.0
4	0.006	0.3	0.45	80.0
5	0.008	0.4		
6	0.010	0.5		
7	0.012			
8	0.014			
9	0.016			
10	0.020			
11	0.024			
12	0.026			
13	0.028			
14	0.030			
15	0.032			
16	0.036			
17	0.040			
18	0.042			
19	0.046			
20	0.050			
21	0.060			
22	0.080			
23	0.100			
24	0.200			
25	0.300			
26	0.500			

Appendix B

Design of Experiment - Transversely Isotropic Model

This appendix shows all the levels and parameters used as input to the computational simulation for the transversely isotropic model. A total of 3000 combinations are used based on this DOE.

Levels	E_3/E_1	G_{23}/E_1	σ_{11}^y/E_1	$\sigma_{33}^y/\sigma_{11}^y$	n
1	0.5	0.1	0.001	0.5	0
2	0.8	0.3	0.002	0.8	0.1
3	1.0	0.6	0.003	1.0	0.2
4	1.5	1.0	0.005	1.5	0.3
5	2.0		0.010	2.0	0.4
6					0.5

Appendix C

Author Attribution Statement

Author contribution statements

Journal Name:	*Surface & Coatings Technology*
Manuscript Title:	Nanomechanical Properties of Thermal Arc Sprayed Coating Using Continuous Stiffness Measurement and Artificial Neural Network
Authors	Wai Yeong Huen, Hyuk Lee, Vanissorn Vimonsatit, Priyan Mendis, Han-Seung Lee
Corresponding Author:	Wai Yeong Huen

Wai Yeong Huen and Hyuk Lee conceived of the presented idea. Wai Yeong Huen and Hyuk Lee developed the theory and performed the computation, and Vanissorn Vimonsatit and Priyan Mendis verified the analytical methods. Vanissorn Vimonsatit and Priyan Mendis encouraged Wai Yeong Huen and Hyuk Lee to investigate nanomechanical properties of material using indentation and ANNs and supervised the finding of this work. Han-Seung Lee guided Wai Yeong Huen in compiling the experimental result and provided critical input to the material's properties reported in the paper. All authors discussed the results and contributed to the final manuscript.

I have read *Surface & Coatings Technology* policy and declare that above information is complete and correct.

Name: **Wai Yeong Huen**

Signature: Date: **03.01.2019**

Author Contribution Statements

Journal Name:	*MDPI – Materials*
Manuscript Title:	Relationship of Stiffness-Based Indentation Properties Using Continuous-Stiffness-MeasurementMethod
Author:	Wai Yeong Huen, Hyuk Lee, Vanissorn Vimonsatit, Priyan Mendis
Corresponding Author:	Wai Yeong Huen

Wai Yeong Huen conceived of the presented idea. Wai Yeong Huen and Hyuk Lee developed the theory and performed the computation, and Vanissorn Vimonsatit verified the analytical methods. Vanissorn Vimonsatit and Priyan Mendis encouraged Wai Yeong Huen and Hyuk Lee to investigate nanomechanical properties of material using indentation and supervised the finding of this work through the dimensional analysis approach. All authors discussed the results and contributed to the final manuscript.

I have read *MDPI – Materials* policy and declare that above information is complete and correct.

Name: **Wai Yeong Huen**

Signature: Date: **03.11.2019**